# ABSTRACT


| | |
|---|---|
| Title of Dissertation: | DEVELOPMENT OF A MICROSCALE ELECTROCHEMICAL PLATFORM FOR THE ANALYSIS OF THERMAL PROFILES OF IMMOBILIZED DNA SECONDARY STRUCTURES |
| | Sarah Menio Robinson, Doctor of Philosophy, 2020 |
| Dissertation directed by: | Professor Sang Bok Lee<br>Department of Chemistry and Biochemistry |



Understanding the thermal stability of DNA secondary structures is important to the pharmaceutical industry, as drug molecules that strongly bind will increase the stability of the structure, leading to higher measured melting temperatures. Development of an electronic platform that can measure the thermal profiles of small-volume samples with automation and methodology that is scalable for high-throughput screening (HTS) would represent an important asset for the drug discovery process. This thesis endeavored to produce and demonstrate the feasibility of such a technology. A microelectronic device has been fabricated in the configuration of a planar electrochemical platform with an embedded platinum thin film that can function as both a platinum resistance thermometer (PRT) and as a resistive microheater. The device assembly as well as automation of the temperature control and electrochemical methods

have been instituted to increase measurement repeatability with the microscale device. The operational program was developed with a variety of features, including a PID controller, and has been demonstrated for a two-device array; functioning is scalable to larger device arrays with the addition of suitable electronics. A proof-of-concept methodology has been shown for monitoring the stabilization effects of ligand binding to duplex DNA. Results are presented for both refrigeration with resistive heating, and thermoelectric cooling and heating. The technology has also been adapted to examine other DNA secondary structures, such as G-quadruplexes, and the stabilization of these structures. The resulting analysis of such immobilized intramolecular secondary structures has demonstrated that the systems are more complicated and further fundamental studies are needed. With the future incorporation of microfluidics and larger-device arrays, a range of effects can be tested based on the demonstrated technology to understand binding events of relevance to drug discovery and the complexities of the surface chemistry effects on the analysis of thermal profiles.

# DEVELOPMENT OF A MICROSCALE ELECTROCHEMICAL PLATFORM FOR THE ANALYSIS OF THERMAL PROFILES OF IMMOBILIZED DNA SECONDARY STRUCTURES

by

Sarah Menio Robinson

Dissertation submitted to the Faculty of the Graduate School of the
University of Maryland, College Park, in partial fulfillment
of the requirements for the degree of
Doctor of Philosophy
2020

Advisory Committee:
Professor Sang Bok Lee, Chair
Professor Jeffery T. Davis
Professor Don L. DeVoe
Dr. Steve Semancik
Professor Herman O. Sintim

# Dedication

To my parents, Gregory and Elizabeth Menio,

and to my husband, Patrick Robinson.

# Acknowledgements

There are many people who have supported me and provided mentorship over my graduate career. I would like to thank Professor Herman Sintim for welcoming me into his lab at University of Maryland (UMD) and his continued support as he transitioned to Purdue University. I would also like to thank Professor Sang Bok Lee for teaching me electrochemistry fundamentals and advising the second half of my graduate school journey. I am also extremely grateful for the mentorship both in and out of the lab by Dr. Steve Semancik. I sincerely appreciate his help improving my writing through reading countless drafts and providing me with the opportunity to work with him at the National Institute of Standards and Technology (NIST). I would also like to express my deepest appreciation for my additional committee members: Professor Jeffery Davis for teaching me how to understand complex mechanisms and Professor Don DeVoe for his time and support of my graduate school career.

I would like to thank the Sintim group both at UMD and Purdue University, especially Dr. Zuliang Shen, Dr. Ben Roembke, Dr. Jie Zhou, and Dr. Clint Mikek for their mentorship and answering all of my questions. Thank you to the group members at Purdue that have included me in so many group meetings via video conferencing. I would also like to extend my thanks to the Sang Bok Lee group for their help with electrochemistry questions and for being so welcoming when I was at UMD.

I am extremely grateful for the support I received from so many individuals at NIST. I would like to express my deepest appreciate to Dr. Dean Ripple for his

invaluable discussions teaching me how to be a good scientist and for providing support in areas ranging from thermometry, statistics, to scientific decision making. I want to express my gratitude for Christopher Montgomery's assistance assembling devices and teaching me fabrication, but most importantly, I appreciate his ability to distill complex problems into simple analogies. I would also like to thank Dr. Kristen Steffens for her assistance with XPS, and Michael Carrier, for teaching me many tricks to working in the cleanroom. I also had great pleasure working with Dr. Kurt Benkstein, Dr. Richard Cavicchi, Dr. Nicholas Contento, Dr. Sean Lehman, Dr. Srivalli Telikepalli, and Dr. Wyatt Vreeland, and I am thankful for their support in lab and feedback on many practice presentations. I am extremely grateful for the support from Dr. Jon Askim, for his assistance automating the experiments, asking difficult questions, and for providing so much advice. To Dr. Ramya Vishnubhotla, thank you for being so optimistic and for helping me learn how to explain and teach concepts in a clearer way.

There are so many NIST NanoFab staff members that I am extremely appreciative for their time training me and providing troubleshooting assistance: Marc Cangemi, Dr. Lei Chen, Evan Cooper, Joe Di Pasquale, Dr. Gerard Henein, Dr. Rob Ilic, Stoyan Jeliazkov, Peter Litwinowicz, Christopher Ray, Matt Robinson, Dr. Jacob Schumacher, Dr. Kerry Sieben, Daron Wesley, Dr. Liya Yu, and Dr. Jessie Zhang.

I would also like to thank Dr. Lee Freidman, Dr. Monique Koppel, and Dr. Kim Huynh for helping me grow as a TA and for their letters of recommendation.

I am extremely grateful for my funding sources over the past 5 years. I would like to thank Dolores Jackson and Dr. John Fourkas for their help administering the

NIST/UMD Professional Research Experience Program (PREP). I also received a University of Maryland First-year Graduate Student Summer Research Fellowship and a Dean's Summer Research Fellowship. Additionally, I am grateful for travel funds from the University of Maryland Jacob K. Goldhaber Travel Grant and the National Science Foundation (NSF)-funded Biosensor 2018 Travel Award.

Last but certainly not least, I would like to thank my graduate school friends, especially Emily, Leila, and Sam, for relaxing weeknight dinners. To my parents, Gregory and Elizabeth, thank you for always setting the bar high, and for supporting me every step of the way. To my husband, Patrick, thank you for being my rock and keeping me grounded the entire way.

# Table of Contents

# List of Tables

# List of Figures

# List of Abbreviations

| | |
|---|---|
| AC | alternating current |
| ActD | actinomycin d |
| ACV | alternating current voltammetry |
| AFM | atomic force microscopy |
| ALD | atomic layer deposition |
| AQ | anthraquinone |
| bp | base pairs |
| BTD | biased target deposition |
| CAD | computer aided design |
| cDNA | complementary DNA |
| CV | cyclic voltammetry |
| CVD | chemical vapor deposition |
| DASH | dynamic allele-specific hybridization |
| DC | direct current |
| DIUF | deionized ultra-filtered |
| DMSO | dimethyl sulfoxide |
| DNA | deoxyribonucleic acid |
| DPV | differential pulsed voltammetry |
| DSC | differential scanning calorimetry |
| DSF | differential scanning fluorimetry |

| | |
|---|---|
| ECP | electrochemistry control program |
| EDTA | ethylenediaminetetraacetic acid |
| eT | electron transfer |
| FIB | focused ion beam |
| FRET | fluorescence resonance energy transfer |
| HMDS | hexamethyldisilizane |
| HPLC | high-performance liquid chromatography |
| HTS | high-throughput screening |
| IBD | ion beam deposition |
| IPA | isopropyl alcohol |
| LOR | lift-off resist |
| MB | methylene blue |
| 6-MCH | 6-mercaptohexanol |
| MicroE-DASH | microelectrochemical dynamic allele-specific hybridization |
| MSE | mean squared error |
| NP | nanoparticle |
| PCB | printed circuit board |
| PCR | polymerase chain reaction |
| PECVD | plasma enhanced chemical vapor deposition |
| PDMS | polydimethylsiloxane |
| PID | proportional-integral-derivative |
| PRT | platinum resistance thermometer |

| | |
|---|---|
| PVD | physical vapor deposition |
| RIE | reactive ion etch |
| RPM | revolutions per minute |
| RSF | relative sensitivity factor |
| RTV | room-temperature-vulcanizing |
| SAM | self-assembled monolayer |
| SANS | small angle neutron scattering |
| SAXS | small angle X-ray scattering |
| SEM | scanning electron microscopy |
| SERS | surface enhanced Raman spectroscopy |
| SIMS | secondary-ion mass spectrometry |
| SMRT | single-molecule, real-time |
| SMU | source measurement unit |
| SNP | single-nucleotide polymorphism |
| SPR | surface plasmon resonance |
| SWV | square wave voltammetry |
| T-DMF | thermal digital microfluidic |
| TE | thermoelectric |
| TMAH | tetramethylammonium hydroxide |
| UV | ultraviolet |
| UVRR | ultraviolet resonance Raman |
| XPS | X-ray photoelectron spectroscopy |

# Chapter 1 Introduction

## 1.1 Scope and impact

The global biosensor market is expected to exceed more than 26 billion dollars by 2022.[1, 2] Biosensors can be grouped into two main categories: cost-efficient, portable devices primarily developed for point-of-care applications, and relatively expensive, highly sensitive arrays of devices for high-throughput screening (HTS). As fabrication and electronics have improved, the development of miniaturized portable biosensors has progressed, most notably with the glucose sensor that has allowed for rapid and efficient monitoring, positively impacting millions of diabetic patients daily.[3-4] Although the glucose monitor dominates the field of biosensors, Turner has highlighted the larger need for new biosensors to contribute in the growing field of personalized medicine.[5] With increased automation, vast improvements have been made in HTS, offering the ability to measure thousands of samples at once. With traditional drug discovery methods, such as in classical pharmacology, small molecules are screened for possible targets. Developments in the drug discovery industry has also led to reverse pharmacology, where a target is identified and then screened against libraries of small molecules.[6]

This work focuses primarily on DNA-based biosensors, which have been extensively reviewed.[7-8] Although the electrochemical activity of DNA was first probed by alternating current oscillographic polarography in 1960,[9] the field of DNA

sensors did not take off until the 1990's.[10] Carter and Bard investigated the interaction of a ruthenium(II) chelate with DNA.[11] Herne and Tarlov showed that DNA could be immobilized on gold electrodes with an alkanethiol linker,[12] and further work showed that by using the binding of ruthenium(III) hexamine to DNA, the amount of DNA on the surface could be quantified.[13] The Barton research group's early work investigated the binding of metal tris(phenanthroline) complexes to duplex DNA in solution and demonstrated that it occurred electrostatically and hydrophobically to the minor groove, and through partial intercalation.[14] Later work was published showing that the binding methylene blue (MB) to DNA could be measured electrochemically.[15] Fan and coworkers demonstrated that a ferrocene redox tag could be synthesized to the end of the DNA sequence for a reagent-less method to probe complementary DNA sequences.[16] Xiao and coworkers expanded the redox labeling to MB and developed a protocol for MB-labeled DNA for electrochemical DNA (E-DNA) sensors.[17] The field of Au-thiol DNA sensors has expanded in wide variety of areas.[18-21]

Building upon these efforts, and to address the need of a cost-efficient, sensitive method to probe thermal stability that is suitable for HTS, a proof-of-concept microdevice technology coupling electrochemical detection with localized temperature control has been developed and is amenable to an array format. Specifically, the platform can probe the stability of DNA secondary structures on the surface, thereby enabling one to screen for compounds and conditions that could alter the stability. The following sections that follow will describe the significance of thermal stability measurements, indicate a range of methods used for measuring melting temperatures

of biomolecules both in solution and when they are immobilized on a surface, the sensitivity and cost-efficient nature of electrochemical detection, and lastly, how temperature can be controlled and measured on the microscale (a requirement for small sample volume thermal analyses).

As an example, a system using a simple on-off approach for electrochemical sensing of duplex DNA is shown in **Figure 1.1**. A thiol-immobilized duplex has high rates of electron transfer (eT) when the methylene blue (MB) labeled duplex is fully hybridized.[22] When the device is heated, the duplex is denatured and the eT is reduced.[22]

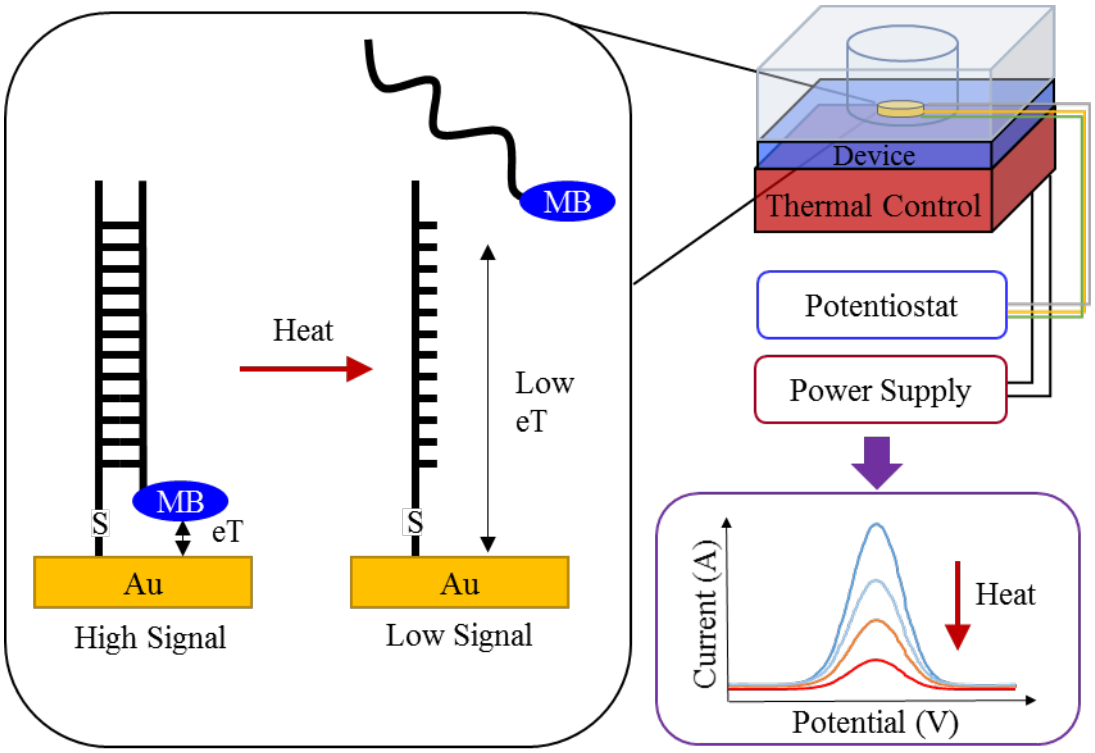


**Figure 1.1**. Schematic of DNA sensor with thermal control using an on-off approach.

This schematic concept involves the basis of the current, *i*, measurement principle used for the developed electrochemical microplatforms, which will be expanded upon in the chapters that follow; critical project aspects include device fabrication, surface chemistry, measurements methods, and results on temperature-dependent probing of biomolecular properties. It is noted here that the functionality of **Figure 1.1** was realized by creating a small-footprint device, with fabrication methods that are compatible with scaling to produce array configurations for efficiently characterizing sets of biomolecules and their interactions with drug candidates. Key platform components (**Figure 1.1**) include a power supply to control the temperature of the device, electronics to monitor temperature, and a potentiostat to detect the electrochemical current changes. Interfacing software was also engineered to permit direct display of the electrochemical readout as a function of temperature.

## 1.2 Thermal stability

Thermal stability, measured by the melting temperature, can be used to determine the characteristics of denaturation of the secondary structures of macromolecules.[23] When measuring the melting temperature of nucleic acid structures, strong binding of small molecules typically stabilizes the structure, thus increasing the melting temperature.[24-25] Therefore, if binding to the macromolecule is known to inhibit a signaling pathway, the method can be used to screen for ligand binding for potential drug molecules.[24] The shift in the thermal stability due to ligand stabilization can be used to prioritize molecules that bind tightly to drug targets during drug discovery. When performing

high-throughput screening on hundreds or thousands of potential drugs, small sample volumes, quick analysis and high signal-to-noise ratios are all necessary for efficient discovery of new drugs. A potential application of this electrochemical technology would be incorporation into a screening platform to probe for ligand-induced stabilization of nucleic acid structures for drug discovery. Utilizing a melting temperature measurement to screen for stabilization effects on an array format can be used to prioritize further detailed investigation on other gold-standard instrumentation.

## 1.3 Methods of calculating $T_m$

The melting temperature, $T_{m,}$ can be measured and calculated using a variety of detection methods, and is defined as the temperature where half of the complex is denatured, and half is still folded or hybridized.[23] Depending on a biomolecule's structure, the denaturation process can vary from being highly reversible (as in many DNA duplexes),[23] to irreversible (with most proteins).[26] When the system being studied produces a sigmoidal population curve vs. temperature, as shown as the black curve in **Figure 1.2**, it is much easier to calculate the mid-point.[27] However, oftentimes the baselines for the completely hybridized and dissociated states are not flat; then an alternative to baseline fitting and finding the midpoint is to calculate the maximum of the first derivative, shown by the blue curve in **Figure 1.2**, although Owczarzy has shown that the maximum of the d(fraction melted)/d(1/T) is more accurate.[27]

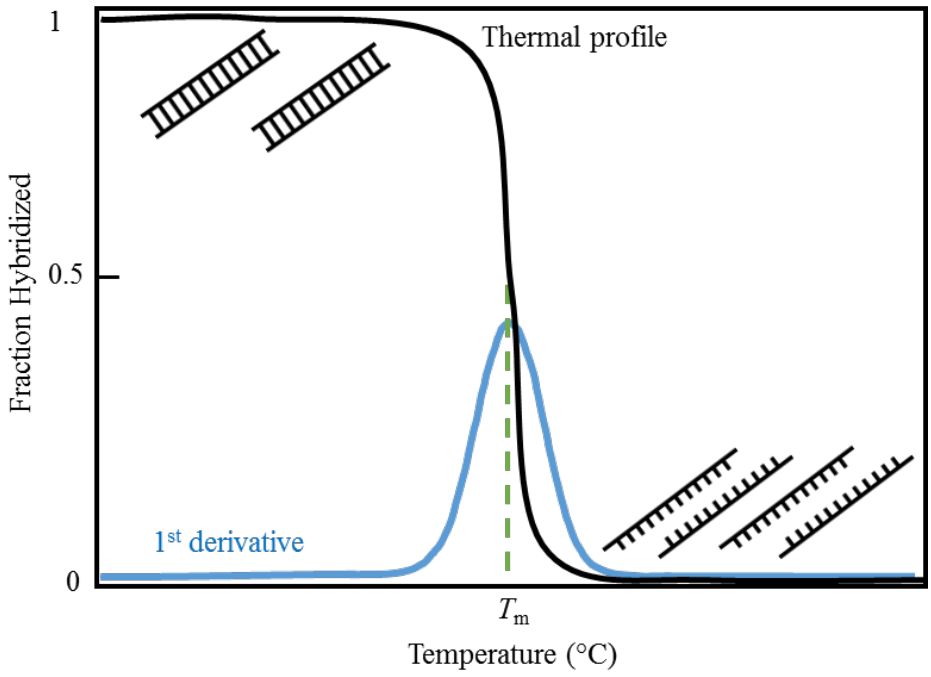


**Figure 1.2**. Schematic of a melting curve of duplex DNA. The thermal profile (black) is plotted as a function of the fraction of duplex that is hybridized. The $T_m$ is the temperature where half of the duplex is denatured and is commonly calculated by the maximum of the 1st derivative (blue). [Adapted from reference [23].]

The melting profiles can also be used to extract additional thermodynamic parameters.[25] For example, if there is a simple duplex system that has a two-state melting transition as shown in the example in **Figure 1.2**, a simple equilibrium expression can be used to describe the states for a non-self-complementary duplex (**Equation 1.1** and **Equation 1.2**).[28]

$$AB \rightleftarrows A + B \qquad \textbf{Equation 1.1}$$

$$where\ K_{eq} = \frac{[A][B]}{[AB]} \qquad \textbf{Equation 1.2}$$

For this model and the resulting relationship, [A] and [B] must be the same so that the total strand concentration is two times the initial [AB]. The total concentration of single-stranded DNA can be summarized by $C_{total}$ (**Equation 1.3**).

$$C_{total} = [A] + [B] + 2[AB] = 2[AB]_{initial}$$ **Equation 1.3**

The fraction of the duplex melted, *f*, is related to the total strand concentration and the equilibrium expression (**Equation 1.4**).

$$K_{eq} = f^2 \frac{C_{total}}{2(1-f)}$$ **Equation 1.4**

At equilibrium, $T_m$ can be related to the standard Gibb's energy, ΔG°, to obtain the standard enthalpy, ΔH°, and entropy, ΔS° (**Equation 1.5 and Equations 1.6**). Previous work has shown that the contributions of $\Delta C_p$ from the differences in the heat capacities of the unfolded and folded states are not large.[29]

$$\Delta G^\circ = -RT ln\, K_{eq}$$ **Equation 1.5**

$$\Delta G^\circ = \Delta H^\circ - T\Delta S^\circ$$ **Equation 1.6**

At the melting temperature, half of the duplex is dissociated, $f = ½$, and the concentrations can be expressed as in **Equation 1.7**.

$$[A]_m = [B]_m = [AB]_m$$ **Equation 1.7**

Therefore, using **Equations 1.3, Equations 1.4** and **Equations 1.7**, the equilibrium expression can be used at the melting temperature, $T_m$.

$$K_{eq} = \frac{C_{total}}{4}$$ **Equation 1.8**

Finally, the value for $K_{eq}$ (**Equation 1.8**) can be substituted in the Gibb's energy relationships (**Equations 1.5** and **1.6**) and solved for $T_m$ (**Equation 1.9**).

$$T_m = \frac{\Delta H^\circ}{\Delta S^\circ - R \ln\left(\frac{C_{total}}{4}\right)}$$ **Equation 1.9**

Based on the abundance of data collected and analyzed of the past few decades, the solution-phase melting temperature of duplex DNA can now be predicted based on the number of A-T/G-C base pairs, the effect of neighboring amino acids in the

sequence, oligomer concentration, and relative salt concentrations.[24, 28, 30-35] Many suppliers of DNA now have oligo analyzers that uses these calculations to predict the melting temperature (such as the IDT OligoAnalyzer: idtdna.com/calc/Analyzer). A recent review by Vologodskii and Frank-Kamenetskii compared the different methods to calculate the melting temperature of DNA duplexes,[36] and highlight the small average deviation from the experimentally measured melting temperatures compared to IDT's OligoAnalyzer. Vologodskii and Frank-Kamenetskii also point out that additional parameters might be used in the software, beyond what IDT has credited.[30] In addition, the authors suggest that even though much work has been done in the field over the past half a century, for the sequences they tested, the recent models do not do statistically better in predicting the $T_m$ than the nearest neighbor method.[35] Furthermore, the authors highlight the current work showing that the greater number of hydrogen bonds in a G-C base pair compared to an A-T base pair has a relatively small contribution to the $T_m$ compared to neighboring effects.[36] In Owczarzy's comments on Vologodskii and Frank-Kamenetskii's review, he emphasized the need for new parameters to be tested on data sets outside the data sets that they were derived from, and that the accuracy of the parameters can depend highly on the data set.[37] Owczarzy also suggests that very short duplexes (8-14 base pairs) are more challenging to predict than slightly larger duplexes (15-30 base pairs).[37] Lastly, he calls for the need for further studies to evaluate base pairing versus base stacking (addressing the stability of duplexes increasing with G-C content) and collecting larger amounts of data sets to evaluate sequence dependence, duplex concentrations and buffer compositions.[37] This

last point could be facilitated by large array-format technologies to analyze the $T_m$ on a microscale.

## 1.4 Experimental methods for detection of $T_m$

Depending on the objective and sample type, there are a wide range of detection methods that can measure data to determine the melting temperature, $T_m$. Each method has its own advantages and limitations, which will be summarized below with respect to sensing duplex DNA. The industry standards are primarily solution-phase measurements, but developments have also included some surface-based characterization methods that will be described in the latter half of this section. In measuring the melting temperature of duplex DNA, the amount of hybridization is also monitored. Where there are improvements on monitoring the hybridization of duplex DNA on the surface, but have not controlled temperature to date, the respective publications will be noted.

### *1.4.1 Solution-phase detection methods*

#### *1.4.1.1 Absorbance*

Absorbance is one of the simplest detection methods, monitoring how much light does not make it through the sample to the detector, instead being absorbed ($I/I_o$). Depending on the detector, a single wavelength of light can be monitored, or a scan can be made over a range of wavelengths. Typical commercial instruments use wavelengths from the near-ultraviolet to visible light (200 to 800 nm). DNA duplex structures have π-π* transitions of the nucleobases, which can be monitored at 260 nm to track the

change of the refractive index of the nucleobases as the population shifts from primarily the duplex state to primarily single-stranded oligomers, an absorbance increase will be observed.[23] This increased ability to absorb more light as the DNA denatures has been attributed to the higher delocalization of excitonic states in the single-stranded form.[38] The absorbance at 260 nm can be plotted vs. temperature and the inflection point, where half of the duplexes are denatured, determines the $T_m$.[23] The major advantage of the technique is that there is not a need for introducing labeling or modifications to monitor the transition. However, when looking at small molecules and proteins bound to the DNA, which tend to also have aromatic rings that adsorb in the same region as the nucleobases, interpreting the melting curves can be challenging.

*1.4.1.2 Fluorescence*

In order to address the issues with small molecules and proteins adsorbing in the same region as the nucleobases, researchers have used fluorescent nucleobase analogs, dyes, and labels to monitor the melting process. Most commonly used is Förster or fluorescence resonance energy transfer (FRET) melting where a fluorophore and quencher molecule are placed close to each other when the duplex or other secondary structure is hybridized or folded.[39-40] When the fluorophore (donor) and quencher (acceptor) are positioned close to each other, the lifetime of the fluorophore is decreased by the energy transfer to the acceptor, measured by a quenching of the fluorescence.[39] As a solution is heated and the structure of interest dissociates or unfolds, the average distance between the fluorophore and quencher increases, reducing the amount of quenching, and thus fluorescence increases.[39] The benefit of

this method is that a range of fluorophores can be used that have different excitation and emission spectra, so that overlaps with the base structure of interest can be avoided. It is worth noting that there is a disadvantage that the label can affect the inherent stability of the structure.[41-42]

Differential scanning fluorimetry (DSF) is a method employed for the analysis of proteins, where a fluorophore in solution can bind to the interior hydrophobic residues of proteins as the protein unfolds.[43-45] When bound, the fluorescence increases and the difference in the fluorescence can be monitored.[43] The major benefit is that the protein of interest does not need to be labeled, but if a researcher seeks to characterize the inherent stability, as well as to measure a small molecule stabilization factor, there will be a competitive interaction with the high concentrations of fluorescent dye present.[46] Another factor to consider is that the fluorescence can be inhibited by other components in protein formulations such as polysorbates (stabilizers).[47] Additionally, the binding of the fluorescent dye can stabilize the structure and skew the determination of the starting point of the unfolding process.[47] Lastly, when aggregates form, more light is scattered, which can affect the emission monitoring at high temperatures.[47]

*1.4.1.3 Calorimetry*

Differential scanning calorimetry (DSC) measures the difference in the change in heat capacity of a sample as compared to a reference sample.[44-45, 47-48] The technique utilizes a sensitive calorimeter and requires high concentrations of samples (approximately 500 µL of 50 to 100 µmol/L) of DNA to achieve adequate signal-to-noise ratios. Although developments have sought to improve (lower) the sample volume required, the

detection method still has limitations. While this measurement may require larger quantities of sample material, DSC can provide high quality data, and is a gold standard in understanding protein formulations. There is also movement toward HTS using DSC, which has involved incorporating automated sample changers and more rapid analysis. The method is currently limited in measuring multiple samples simultaneously, although developments in the analysis of nanoscale materials have been demonstrated with 5 x 5 arrays.[49]

### *1.4.2 Surface-based detection methods*

#### *1.4.2.1 Surface plasmon resonance*

As the field of DNA sensing has evolved, and advancements in surface immobilization have occurred, investigations of the thermodynamics of hybridization have been undertaken to study how tethering alters analyses as compared to solution-phase measurements.[50-51] One of the first commercially available bioanalytical systems designed for understanding biomolecular interactions was surface plasmon resonance (SPR).[52] SPR is an optical sensing technique where the refractive index of a thin film on a surface is monitored.[52] As molecules bind to the surface, the refractive index changes, allowing the binding events to be monitored in real-time. SPR is advantageous because samples can first be immobilized, and then a range of biomolecules and conditions can be flowed to interact with immobilized targets of interest.[52] It is a highly sensitive technique that can obtain a range of thermodynamic and kinetic data for applications from immunogenicity to food analysis.[53] Using SPR, the hybridization of

DNA was monitored as a function of temperature and ionic strength.[54] Other work explored the effect of probe density on the hybridization,[55] as well as detection of mismatches by electric-field induced denaturation.[56]

To further understand the thermodynamics of DNA, Buhot and Halperin first studied the helix-coil transition of short peptides with SPR.[57-59] They later expanded their theoretical work to the analysis of single-stranded DNA and the hybridization of DNA on the surface.[60-64] Fiche and coworkers built a custom SPR with a heated flow cell to study the hybridization of DNA as a function of temperature.[65-66] In these studies, the researchers ran two successive injections, one without and one with the target at a variety of temperatures; this process creates a "calibration" baseline for each temperature value to account for the refractive index changes with temperature variations.[65-66] Melaine and coworkers have shown that using a split-aptamer system, with one half of the aptamer immobilized to the Au sensor surface and the other half tethered to gold nanoparticles (AuNP), could increase the sensitivity to monitor the binding of adenosine to the sandwich structure.[67] Utilizing a custom-made temperature regulation system,[65] they monitored the binding of adenosine at different temperatures, with a limit of detection (LOD) of 30 nmol/L.[68]

*1.4.2.2 Surface-enhanced Raman spectroscopy*

Surface-enhanced Raman spectroscopy (SERS) is an optical technique that utilizes the excitement of plasmons (on a rough, porous, or hole-filled surfaces) to enhance the density of light and therefore increase the Raman signal.[69-70] The use of SERS for the analysis of DNA probes was first published by Vo-Dinh and coworkers, where they

described an ability to detect the hybridization of DNA cresyl fast violet-labeled probe sequences on silver substrates.[71] In 2008, Mahajan and coworkers developed a SERS-melting platform using gold sphere segment void (SSV) substrates made by electrodeposition mounted on a heating element.[72] They measured the hybridization based on the SERS signal of Cy3, Cy5, and Texas Red labels on the 3' position of the target sequence.[72] They also compared the melting temperatures collected by both electrochemically and thermally driven denaturation, showing the correlation between stability measurements, and also demonstrating that both methods have the ability to detect single-base mismatches.[72] Further work focused on electrochemically driven melting profiles, determining that it is not solely based on electrostatic effects as similar effects were seen with peptide nucleic acid (PNA)/ DNA duplexes.[73] More recently, researchers have shown that DNA duplexes can be horizontally tethered and their denaturation can be monitored both electrochemically and thermally, as seen in **Figure 1.3**.[74]

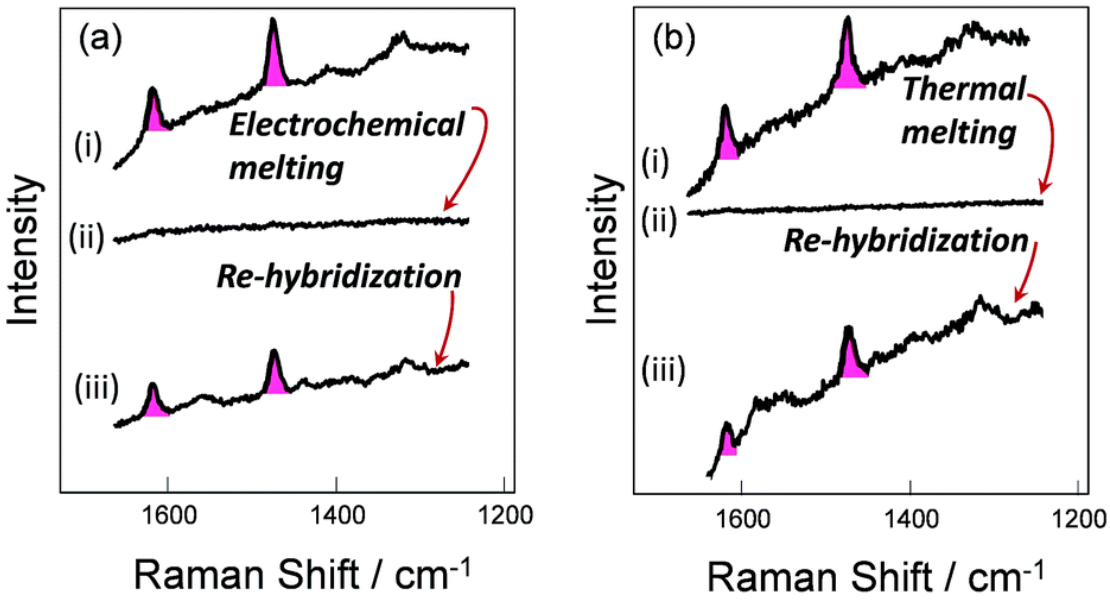


**Figure 1.3.** (a)-(i) and (b)-(i), SER spectra of DNA probe hybridized to a complementary target labelled with Texas Red. (a)-(ii) After electrochemical melting at −1.2 V and (b)-(ii) after thermal melting at 80 °C, in either case, the SERS signal is lost due to DNA denaturation, but recovered (a)-(iii), (b)-(iii) after re-hybridization at room temperature with the labelled target.[74] [Reprinted from E. Papadopoulou, N. Gale, J. F. Thompson, T. A. Fleming, T. Brown and P. N. Bartlett, *Chem. Sci.*, 2016, 7, 386 doi: 10.1039/C5SC03185K. Published by The Royal Society of Chemistry and licensed under CC BY 3.0.]

### *1.4.2.3 Quartz crystal microbalance*

Hybridization of DNA has also been measured with a quartz crystal microbalance (QCM).[75] Recently using QCM, researchers measured the rupture force of a 20-mer duplexes, and saw high correlation of the rupture force with the solution melting temperature of the duplexes.[76] Further work showed that, as expected, the rupture force decreased with temperature, and that the melting temperature could be approximated by extrapolation to the point where the rupture force equals zero.[77-78]

*1.4.2.4 Other surface-immobilized temperature studies of note*

Many other researchers have applied techniques such as fluorescence to analyze surface-immobilized DNA for polymerase chain reaction (PCR) applications. In 1999, researchers published the first dynamic allele-specific hybridization (DASH) method to monitor single-nucleotide polymorphisms (SNP).[79] The workflow of the method is outlined in **Figure 1.4**.[79]

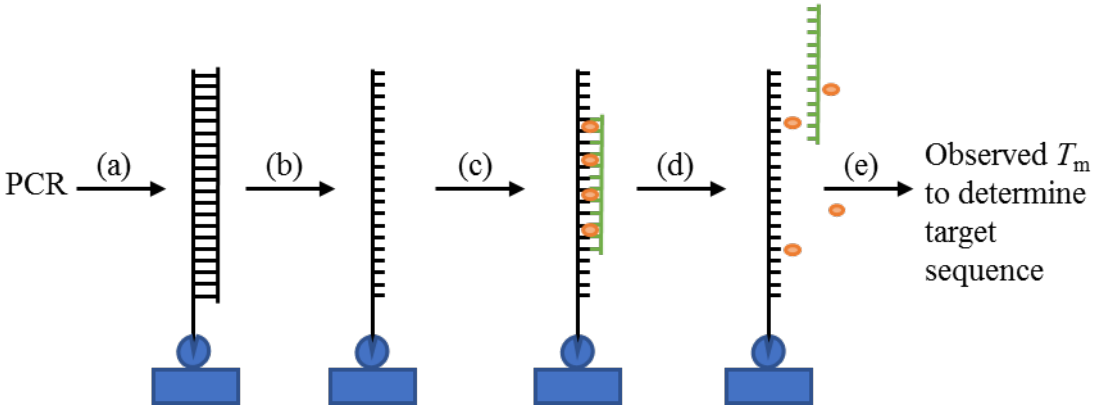


**Figure 1.4.** Experimental design of early dynamic allele-specific hybridization (DASH) methods. (a) Product immobilization, (b) strand isolation, (c) probe hybridization, (d) fluorescence measurement with heating, and (d) analysis. Target DNA is biotinylated and immobilized on a streptavidin-coated microtiter plate. [Adapted from reference [79].]

Using variants of the DASH method, researchers investigated the effects of truncations on SNP detection,[80] and developed a fully integrated system with a platinum resistance thermometer.[81] In the microdevice system, attached to a capillary electrophoresis chip, the fluorescence was measured to show the successful amplification and separation.[81] Dodge and coworkers built upon this work to measure the denaturation of immobilized duplex DNA by measuring the fluorescence of labeled-probe sequences.[82]

Single-molecule, real-time (SMRT) sequencing chips have used millions of zero-mode waveguides (ZMWs) to monitor nucleotide sequencing by detecting the fluorescence of labeled deoxyribonucleoside triphosphates incorporated by DNA polymerase.[83] Using a modified SMRT cell, researchers were able to perform kinetic measurements on 7 nucleotide probes with both negatively charged and positively charged fluorescent dyes to measure the hybridization on a single-molecule level.[84]

Chen and coworkers designed a thermal digital microfluidic (T-DMF) device that performed a 7 s melting curve analysis by monitoring fluorescence of labeled oligonucleotides.[85] The T-DMF device, had used a chromium thin film as a heater when applying a DC voltage, and droplet manipulation was accomplished with an applied AC voltage.[85] Knob and coworkers used a microfluidic device with a oligonucleotide modified-monolith to monitor the solid-phase extraction conditions by coupling hybridization and then a temperature controlled elution to obtain high purity of the complimentary sequence, cDNA; their method was monitored by a fluorescently tagged cDNA.[86] Traeger and Schwartz used FRET to investigate duplex and hairpin structures immobilized with hydrophobic, 1-dodecanethiol, and hydrophilic, methyl-$PEG_4$-thiol, SAMs.[87]

### *1.4.3 Electrochemical detection methods*

Electrochemical detection has the advantage that it does not need expensive detectors or amplifiers and can be used in a configuration that is amenable to miniaturization when analyzing surface-immobilized species. Most electrochemical methods use a

potentiostat and some are commercially available as portable (rather inexpensive) potentiostat units. A typical electrolytic cell, shown in **Figure 1.5**, contains a working electrode, reference electrode, and a counter electrode.[88] The working electrode materials can range from mercury, carbon and platinum, to gold.[88] Although carbon electrodes can have a broad potential window, low-cost, and are relatively chemically inert, the thiol chemistry extensively used in tethering DNA to the surface makes gold working electrodes highly desirable in DNA hybridization biosensors.[88] The purpose of a reference electrode is to permit measurement of a reproducible, stable potential compared to the working electrode. To produce a constant potential reference, reference electrodes typically have a "buffering" capacity against external factors and thus are composed of two components, such as Ag/AgCl or $Hg/Hg_2Cl_2$.[88] When making thin film devices, it can be challenging to make a true reference electrode because reference electrodes commonly have a frit and/or bridge to minimize sample contamination with a reference solution. For planar microdevices, materials such as platinum that are relatively unreactive, can be used as a pseudoreference electrode. Lastly, a counter, or auxiliary, electrode is used as a source of electrons and should have a surface area that is greater than the working electrode to avoid limiting the current flow.[88]

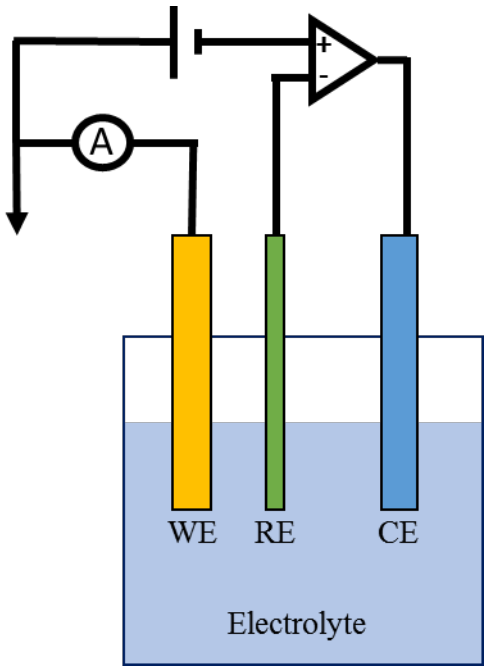


**Figure 1.5.** Schematic of a traditional electrochemical cell with a working electrode (WE), a reference electrode (RE), and a counter electrode (CE).

Using a standard electrochemical cell, a wide range of electrochemical analysis can be done. A few examples of microdevices for various applications are summarized below. Although solutions of redox-active components have been analyzed, to achieve higher sensitivity, immobilization to the surface increases the relative concentration and thus can lower the limit of detection making it workable even in a small footprint.

*1.4.3.1 Redox labeling*

Using a redox probe, one can attain much higher sensitivity since the generated signal is higher and output information (current) can be measured directly and further amplification can increase the sensitivity even more.[89] However, labeling or tagging the analyte is often required to probe the substrate. When selecting a redox tag, it is

easy to avoid the oxidation of the nucleobases and therefore it is rare to have any interference or background. A wide range of probes has been developed over the years with a range of oxidation and reduction potentials.[90] Redox potentials should also be in between the oxidation potential of guanine (0.9 V vs. Ag/AgCl) and the reduction potential of the alkanethiol attachment (between -0.8 to -1.1 V vs. Ag/AgCl).[90]

*1.4.3.2 Methylene blue (MB)*

Kelley and coworkers showed the utilization of methylene blue (MB) binding to duplex DNA to measure DNA on gold surfaces (**Figure 1.6**).[15] Later work showed that using a stem-loop modified on the 5'-end with a thiol and modified with MB on the 3' end, they could monitor the binding of a complementary DNA sequence, changing the relative position of the MB, and thus the change in measured current level.[91]

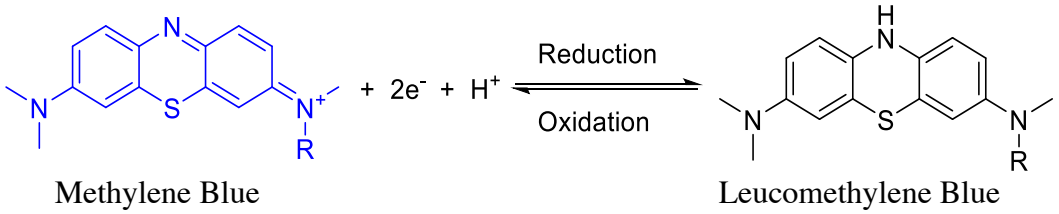


**Figure 1.6.** Reduction of methylene blue.

The synthesis of MB is also simple compared to other redox labels, making it a preferred form to be incorporation into commercial phosphoramidites.[92] MB produces a 3-fold larger signal than that derived from Nile blue,[93] and it is stable in chloride containing solutions, unlike ferrocene.[94] MB has been incorporated in DNA duplexes and studied for various effects on charge transfer: base mismatch, probe distance, electron transport mechanism, and intercalation between base pairs.[90]

#### *1.4.3.3 Chronoamperometry*

Chronoamperometry is one of the simplest electrochemical techniques. In this technique a potential step is applied, and the current is measured over a period of time.[88] By monitoring the current over time, the effects of the electron double layer charging and any diffusion effects in solution can be measured.[88] Utilizing a series of chronoamperometric steps from an electronic aptamer-based sensor, researchers were able to measure in vivo pharmacokinetics based on a sensor placed in the veins of live rats.[95]

#### *1.4.3.4 Electrochemical impedance spectroscopy (EIS)*

As compared to amperometry and voltammetry that use DC current, electrochemical impedance spectroscopy (EIS) uses AC current to monitor the frequency-dependent resistance of the current flow.[88] EIS can be useful because it provides information on both electron double layer effects and diffusion-limited reactions.[88] Marquette and coworkers developed a DNA chip for a flow cell to measure the impedance as a function of temperature and were able to monitor the denaturing of a $d(T)_{20}$ duplex.[96] In their devices, $Si/SiO_2$ chips were coated with aminopropyltriethoxysilane, activated with glutaraldehyde, and then functionalized with an amino-modified $d(T)_{20}$ oligomer.[96] By applying a 10 mV rms AC signal and at a frequency of 100 kHz, the researchers could calculate the real and imaginary impedance at each temperature value.[96] Their work showed that there were higher rates of hybridization with lower incubation times (lower probe density), and that a melting analysis of unlabeled

sequences could be done in under 15 min.[96] Later studies with impedance-based sensors have shown that the impedance of the hybridization of DNA can also be characterized on thiol-modified DNA on gold electrodes.[97-98]

*1.4.3.5 Voltammetry*

In voltammetry, the current is measured as a function of the potential. There are several different voltammetry techniques depending on whether the potential is swept, cycled, or pulsed. Cyclic voltammetry (CV) is one of the most common voltammetric techniques.[88] As the name implies, the potential is swept in one direction and then swept back to the original point to form a full cycle of both the oxidation and reduction.[88]

Belozerova and Levicky utilized CV to analyze the hybridization of DNA by tethering 9-mer duplexes to 3 mm diameter gold disk electrodes, and the thermal profiles of the hybridization with a ferrocene-labeled complimentary sequence as a function of temperature.[99-100] In their work, they also investigated the binding of netrospin, a known minor groove binder to DNA, as a function of ionic strength and ligand concentration to show that the thermodynamics on the surface do vary slightly from solution-phase measurements.[99]

*1.4.3.6 AC voltammetry*

Similar to EIS, AC voltammetry (ACV) is an impedance, or resistance, measurement where an applied DC potential is scanned slowly, and an AC component is applied on top.[88] The applied DC potential is used to change the equilibrium of oxidized or reduced species which then can be oscillated with the AC wave.[101] An example of an application

of ACV was its coupling with the DASH method to detect SNP on a microelectronic platform.[102]

*1.4.3.7 Differential pulse voltammetry (DPV)*

While CV can provide good electrochemical signals, it is difficult to differentiate between the capacitive (charging) currents and faradaic (electron transfer) currents.[88] In order to overcome this challenge and increase sensitivity, pulsed voltammetric techniques were developed. Differential pulsed voltammetry (DPV) was developed based on staircase voltammetry, where a pulse of potential would be applied over a stepped baseline pulse.[88] The current is measured just before the pulse, and at the end of the pulse to separate the charging and faradaic currents.[88] The difference between those two current readouts is plotted as a function of the baseline potential at each step.[88] This technique was compared with results obtained with CV and ACV for a DNA stem-loop sensor and researchers demonstrated that DPV can be more versatile for DNA sensor architectures.[103]

*1.4.3.8 Square wave voltammetry (SWV)*

Square wave voltammetry (SWV) is a pulsed voltammetric technique. It monitors the current at both the forward potential pulse ($i_1$) and reference potential pulse ($i_2$), and the difference in current ($I_{meas}$) is plotted versus potential (**Figure 1.7**).[104-106] This voltammetric technique produces peaks for faradaic currents (oxidation or reduction) as opposed to sigmoidal waveforms, yielding a higher signal-to-noise ratio and thus

higher sensitivity.[105] The resulting peak heights can be used to quantify the electron transfer reaction.

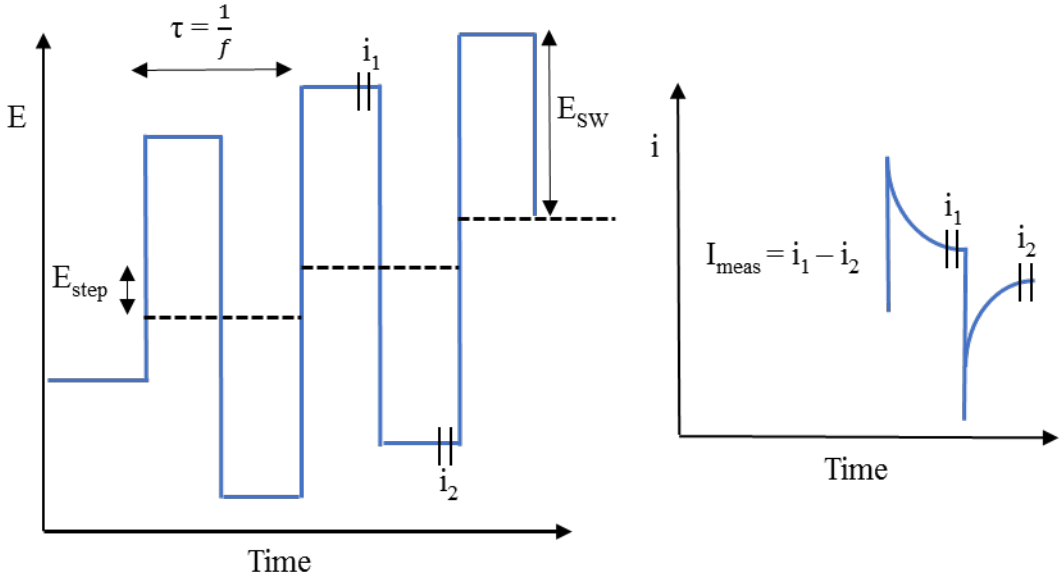


**Figure 1.7.** Square wave voltammetry pulse sequence.

Meunier-Prest and coworkers used SWV to probe the binding of both methylene blue (MB), potassium ferricyanide, and hexamineruthinium(III) chloride to immobilized $d(T)_{15}$.[107] They also looked at the effect of the MB binding as a function of temperature to show that they can use the MB current to probe the concentration of duplex DNA on the surface, and measure a thermal profile.[107]

One of the key aspects to be investigated involves looking at probes as a function of temperature, and to acquire information on molecular thermal stability. In order to do this on a microelectrochemical platform, a localized microheater is needed.

## 1.5 Thermal control in small-scale $T_m$ determination

There are many methods to control the temperature of a surface or solution. Most commonly used are thermoelectric modules, specifically Peltier modules, resistive heaters, and heated-wire electrodes.[108]

### *1.5.1 Thermoelectric control*

Thermoelectric (TE) modules convert electrical energy to temperature changes by having a series of solid p and n type materials that function as a heat pump.[109] The concept uses the Peltier effect and therefore often called Peltier modules.[109] TE modules can be controlled with a DC power supply and depending on the current direction, can either cool or heat a sample (**Figure 1.8**).[109] A wide range of TE modules are commercially available and can be coated or plated in a variety of materials to be customized for each individual application.

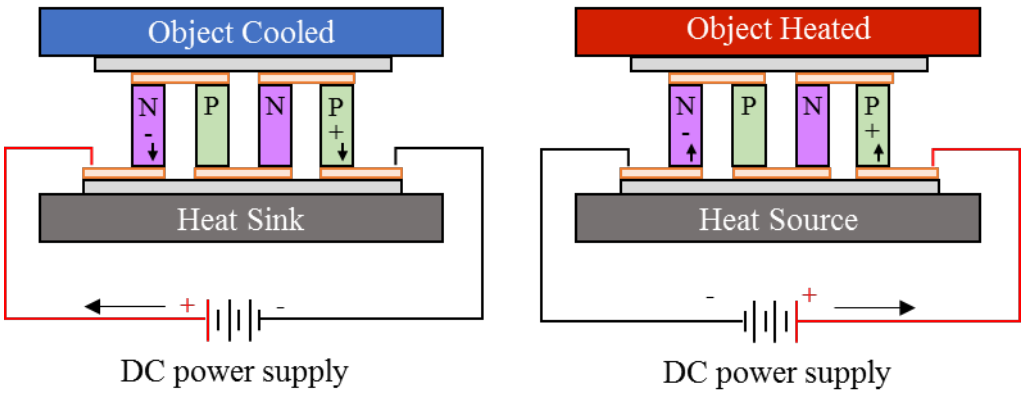


**Figure 1.8**. Schematic of thermoelectric device containing p- and n-type materials. Depending on the direction of the DC current, an object can either be heated or cooled. [Adapted from reference [109].]

### *1.5.2 Resistive heating*

Microheaters have been investigated for a wide range of applications including gas sensing, photonic biosensing, and electrochemical measurements.[108] Gas-phase sensing with temperature variation has utilized microhotplate platforms such as the 3-dimensional structure in **Figure 1.9**, which has utilized various materials including doped polysilicon.[110-111] Platinum is very stable and its resistance is proportional to temperature at the lower temperatures needed for solution-phase measurements on biomolecular samples.[112] Therefore, a voltage can drive a current that heats the platinum, and the temperature-dependent resistance can be measured to calculate the real-time temperature. Contento and Semancik developed an electronic microdevice with a platinum microheater and characterized the heating in both gas-phase and solution samples.[113]

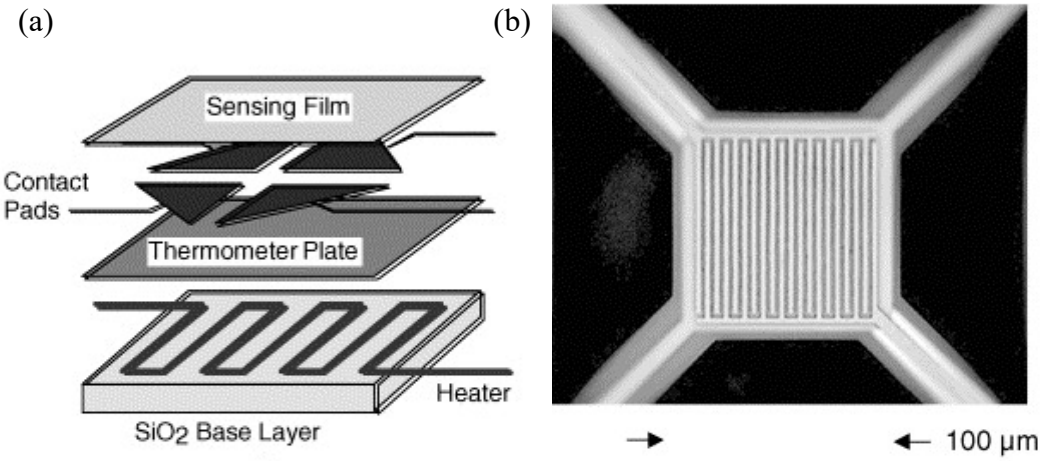


**Figure 1.9.** Microheater technology used for gas sensing: (a) schematic of functional layers and (b) micrograph of microhotplate with two interdigitated electrodes.[111] [Reprinted from *Sensor Actuat B-Chem, 77* (1-2), Semancik, S.; Cavicchi, R. E.; Wheeler, M. C.; Tiffany, J. E.; Poirier, G. E.; Walton, R. M.; Suehle, J. S.; Panchapakesan, B.; DeVoe, D. L., Microhotplate platforms for chemical sensor research, 579-591, 2001, with permission from Elsevier.]

### *1.5.3 Heated wire temperature control*

The concept of heated wire electrodes is again an application of electrical, or Joule, heating as discussed in the previous section. In hot-wire electrochemistry the resistive heating element also functions as the electrode for electrochemical measurements. Grundler and Flechsig have utilized hot-wire electrochemistry, which was typically used to clean electrode surfaces without changing the temperature of the bulk solution, and to deposit and strip arsenic(V) traces.[114] They later applied this technique to analyzing the stripping of nucleic acids on carbon paste electrodes.[115] A recent review highlights the range of materials and applications of heated electrodes, such as probing DNA hybridization kinetics, DNA melting curves, to the detection of enzyme-labeled DNA.[116-120]

## 1.6 Summary

Advances in techniques for DNA immobilization, electrochemical detection, temperature control, and device fabrication have been utilized to develop an integrated microelectronic platform for measuring the thermal stability of a wide range of tethered bioanalytes. The initial feasibility of the technology was demonstrated by a previous graduate student, Dr. Zuliang Shen. Using a protype device, he was able to demonstrate the ability to detect a single-base mismatch by measuring a $\Delta T_m$ of 5.1°C.[22] The contents of this thesis discuss a new fabrication protocol to address challenging insulation issues, incorporation of automation for the thermal profile analysis,

demonstration of a new methodology to screen for ligand stabilization of duplex DNA, and steps towards performing analyses of other secondary structures.

Chapter 1 has provided an overview of DNA biosensors and the current methods employed to measure the thermal profiles of DNA secondary structures. It also summarizes specific criteria and goals sought in developing a microdevice technology for measuring DNA thermal profiles.

Chapter 2 discusses the fabrication of a planar electrochemical platform with an embedded platinum thin film that can function as both a platinum resistance thermometer (PRT) and as a resistive heater.

Chapter 3 highlights the device assembly as well as automation of the temperature control and electrochemical methods instituted to increase measurement repeatability. The program developed includes a proportional-integral-derivative (PID) controller and has been demonstrated for operation of a 2 x 1 array.

Chapter 4 shows a proof-of-concept methodology for monitoring the effects of ligand binding to duplex DNA. Results are presented for both refrigeration with resistive heating and thermoelectric cooling and heating.

Chapter 5 discusses aspects of developing the technology for other DNA secondary structures, such as G-quadruplexes, and the areas of optimization required for the analysis of the stabilization effects of these structures.

# Chapter 2 Fabrication of Devices

## 2.1 Introduction to fabrication methods

This chapter will focus on techniques used in the production of microdevices for electrochemical measurements: physical vapor deposition (PVD), chemical vapor deposition (CVD), ion beam etching, reactive ion etching (RIE), lithography, and characterization. Due to a sensitivity toward particle contaminants, fabrication using these techniques is performed in Class 100 or Class 1000 cleanroom facilities: these facilities have gowning procedures and air filters to reduce the particle counts to less than 100 or 1000 particles larger than 0.5 μm per cubic foot of air, respectively.

There are two primary methods used to deposit thin films on wafers: physical vapor deposition (PVD) and chemical vapor deposition (CVD). In PVD, material is vaporized from a solid target and deposited directly on a substrate in vacuum.[121] Common PVD techniques include evaporation, where a crucible of metal is heated under vacuum, and sputtering, where a target is bombarded with argon plasma.[121] Compared to evaporation, sputtering methods have significantly slower deposition rates, but produce a higher quality film. The National Institute of Standards and Technology (NIST) Center for Nanoscale Science and Technology (CNST) NanoFab facilities have two e-beam evaporation tools that can hold four 4-inch wafers simultaneously. Therefore, surface electrodes were deposited using e-beam evaporation. The CNST NanoFab facility sputtering tool has much slower deposition rates relative to e-beam evaporation and can only hold one 4-inch wafer. The platinum

resistance thermometer (PRT) required a higher quality film and as a result was deposited using sputtering. Unlike direct deposition via PVD, CVD utilizes precursor gases that react with the surface to form conformal coatings.[121] The reaction can be controlled and accelerated by properly manipulating the pressure, temperature, and exciting a gas-phase. Common CVD equipment includes plasma-enhanced CVD (PECVD) and atomic layer deposition (ALD); both of these techniques are used for the non-metallic insulation layers.

Pattern transfer is accomplished using lithography. Common lithography techniques include the use of a photosensitive film that upon exposure will either remain on the film (negative) or be developed (positive).[121] Due to the micron-sized features involved in this project, contact alignment can be used instead of the more expensive e-beam lithography.

For film removal, there are a range of etching techniques that can be used from chemical etching, reactive ion etching (RIE), and ion beam etching. To etch through metals, ion milling with an argon beam firing ions at an angle (typically 100° or 135°) to remove atoms on the substrate. To etch the contact pads of the embedded Pt thin film, a combination of RIE and ion beam etching was used.

## 2.2 Microdevice fabrication design[122]

The microscale platform shown schematically in **Figure 2.1** was fabricated on a fused silica wafer. Silica was chosen due to its low thermal conductance, which allows for rapid, localized thermal response and promotes a stable heating profile at the

electrochemical interface. The embedded Pt film can act as a resistive heater by applying a large DC current; the film heats the surrounding area which transfers heat through the (electrically) insulating layer. Alternately, applying a low voltage and closely monitoring the current allows the film to function as a Pt resistance thermometer (PRT). The ~ 650 Ω platinum film was designed in a bifilar, serpentine pattern to provide uniform heat transfer and minimize any field effects through antiparallel current flow. The resistance of the Pt thin film was approximately linear, with a thermal coefficient of resistance large enough to make a practical thermometer. After calibration, resistance measurements of the heater provided direct, local measurement of the device temperature in real time.

The Pt film was isolated from the three planar top-surface electrodes with a layer of silicon oxide, which provides dense and pinhole-free electrical insulation. The electrode system deposited above the insulation layer allowed electrochemical current measurements at different temperatures. Analyte sample solution was contained over the electrode area in a polydimethylsiloxane (PDMS) chamber with a PDMS lid to minimize evaporation, and the entire chamber is removable for cleaning to allow cleaning of the electrochemical surface. The small footprint and thin profile of the microscale system led to an overall low thermal mass that allowed effective heat transfer for small-volume sample measurement (generally $\leq$ 10 μL). All sensor components were integrated for electrochemical measurements within the microchamber and can be readily adapted to develop multi-element array devices for high-throughput screening.

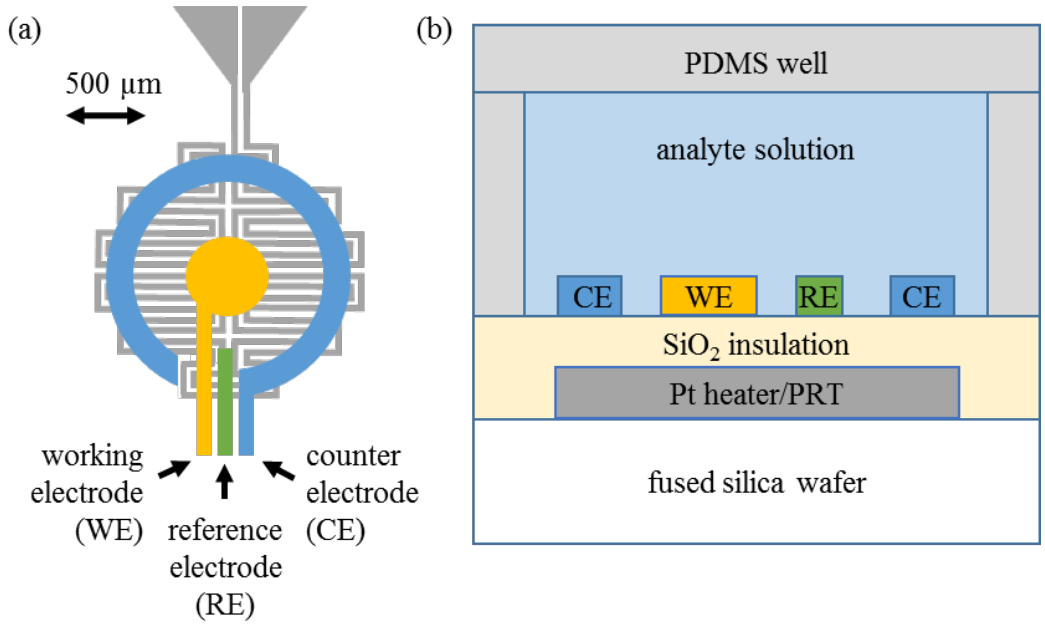


**Figure 2.1.** Electrochemical platform architecture: (a) top-view schematic of the platform (without the PDMS sample chamber) and (b) side-view schematic, including a sample well (not to scale). The Pt heater/PRT fabricated on a glass wafer was isolated by a $SiO_2$ insulating layer. Au and Pt electrodes were fabricated by two lift-off e-beam evaporated depositions. The PDMS chamber and lid were centered above the electrode system.[122]

Heater and electrode layouts were originally designed by Dr. Zuliang Shen and the associated CAD files were used in the fabrication of further devices produced in this work. Optimization of the heater width and spacing for the devices is described in his dissertation.[123]

## 2.3 Fabrication procedures

There are two main methods to develop a thin film metal in a controlled pattern: metal lift-off and etching. The former involves a two-layer lithography step typically with a lift-off resist (LOR).[121] The LOR provides an undercut so that once the thin film of metal is deposited, there is a clean break (no deposition) between the metal on the

substrate and the metal on the top of the photoresist.[121] This processing was used for the surface electrodes in the fabricated devices and the processing can be done on multiple devices simultaneously. On the other hand, deposition of a blanket film and then etching back involves more steps, and often single wafer processing, but can leave a higher quality film required for the PRT and later insulation with oxide. These methods are illustrated in **Figure 2.2**.

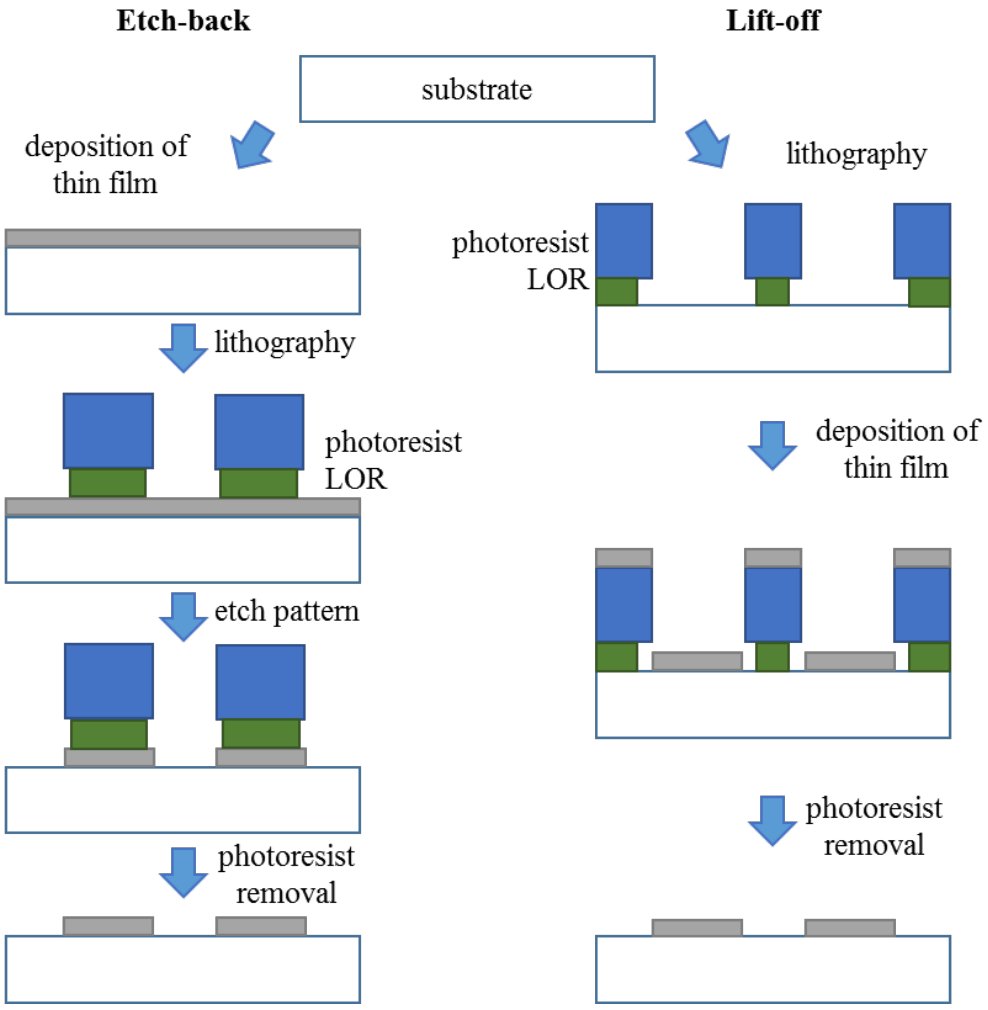


**Figure 2.2.** Fabrication steps for etch-back and lift-off processing. Both examples are shown using positive lithography and lift-off resist (LOR), but using the inverse photomasks to achieve the same pattern.

The device fabrication procedure used in earlier prototypes made by Dr. Zuliang Shen used metal lift-off of e-beam deposited Pt heaters which were insulated with 300 nm PECVD oxide.[22, 123] Due to the replacement of the CNST PECVD tool, subsequent fabricated wafers were not insulating as well as the devices used in previous work. Therefore, in addition to adjusting the insulating oxide, the fabrication of the Pt thin film was switched to minimize particle contamination and rough edges. The major changes discussed in this chapter are the switch from metal lift-off to etching the heater pattern and the development of sandwich and thicker oxides for better electrical insulation. The workflow for the new fabrication of the microdevice is shown in **Figure 2.3**. Overall fabrication steps can be simplified into the key procedures that will be discussed in this section: (a) deposition of a blanket Pt film with Ti adhesion layer(s) with cluster sputter, (b) lithography and ion mill etching of serpentine pattern of Pt, (c) deposition of $SiO_2$ insulation by either thinner ALD and PECVD sandwich oxide or a thicker PECVD layer with the optimization of the insulator discussed further in Section 2.4, and (d) lithography and metal lift-off of surface electrodes.

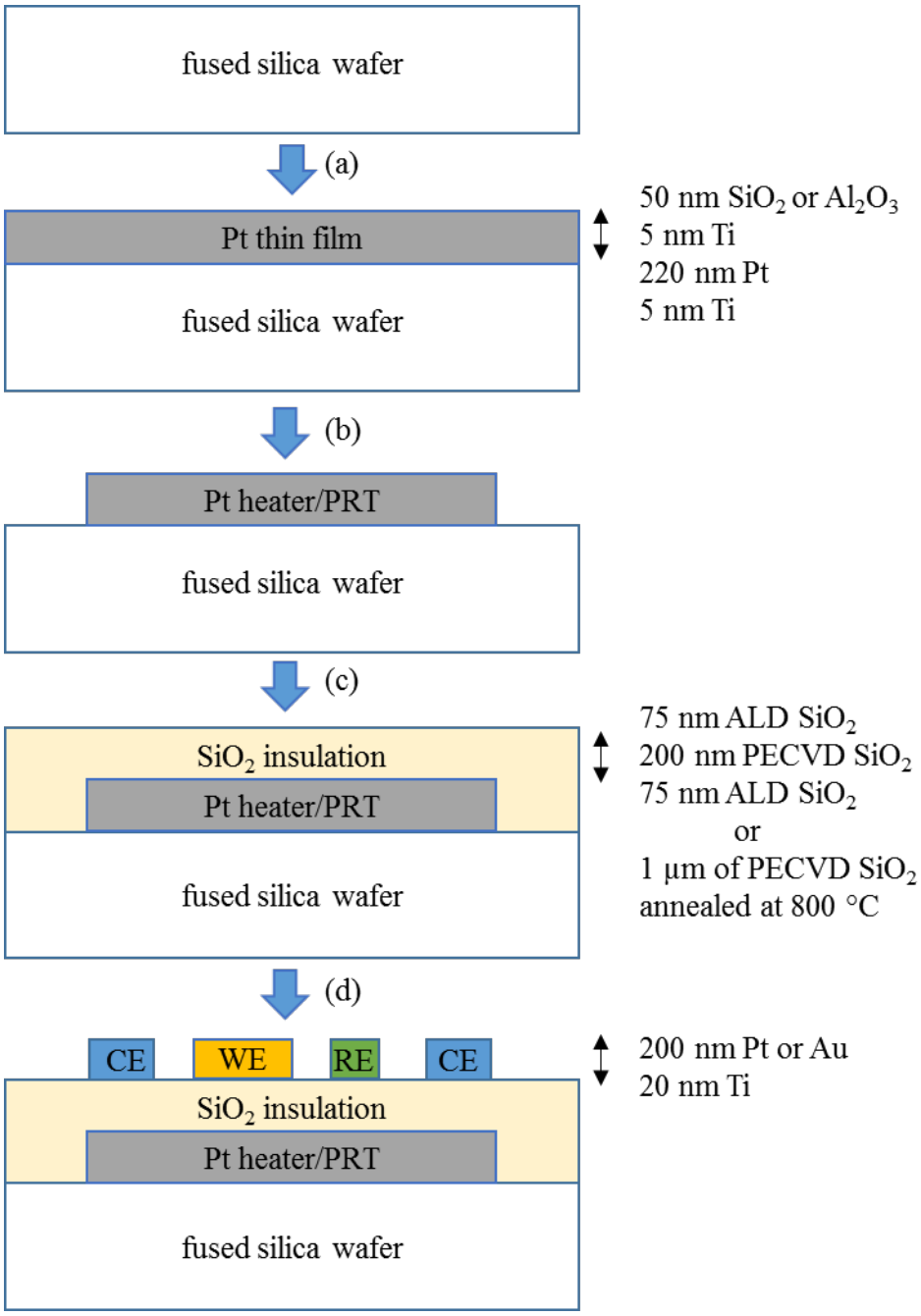


**Figure 2.3.** Fabrication workflow: (a) deposition of a blanket Pt film with Ti adhesion layer(s), (b) lithography and etching of serpentine pattern of Pt, (c) deposition of $SiO_2$ insulation, and (d) lithography and metal lift-off of surface electrodes.

### *2.3.1 Development of photomasks*

The original fabrication of the devices used metal lift-off of the Pt thin film. Therefore, the CAD files were reversed so that the heater pattern was protected from the UV development and the mask could be used with positive photoresist for etching. The mask was made in the CNST cleanroom with a laser writer (Heidelberg Instruments DWL 2000 Laser Pattern Generator). Initially, a 5-inch chrome mask with photoresist coating was exposed with the laser writer. The mask was then developed, placed in a chrome etch bath, and then rinsed with water. The photoresist was removed in a bath of 1165 (Microposit remover 1165), rinsed with water, and then cleaned in Nano-Strip. Masks for surface electrodes were made by Dr. Nick Contento.

### *2.3.2 Blanket deposition of Ti/Pt/Ti/$SiO_2$*

The serpentine Pt thin film was deposited using the CNST cluster sputter deposition system (4Wave IBD/BTD cluster sputter deposition system). The first generation recipe used included 5 nm Ti and 220 nm Pt deposited in the biased target deposition (BTD) process module. After patterning of the Pt thin film, the next processing requires the Pt to be encased in an electrically insulating oxide layer. It was found that a blanket film of 5 nm of Ti and 220 nm Pt caused poor adhesion between the exposed Pt and the subsequent layer of oxide, and resulted in a peel-up effect (shown in the SEM micrograph in **Figure 2.4**).

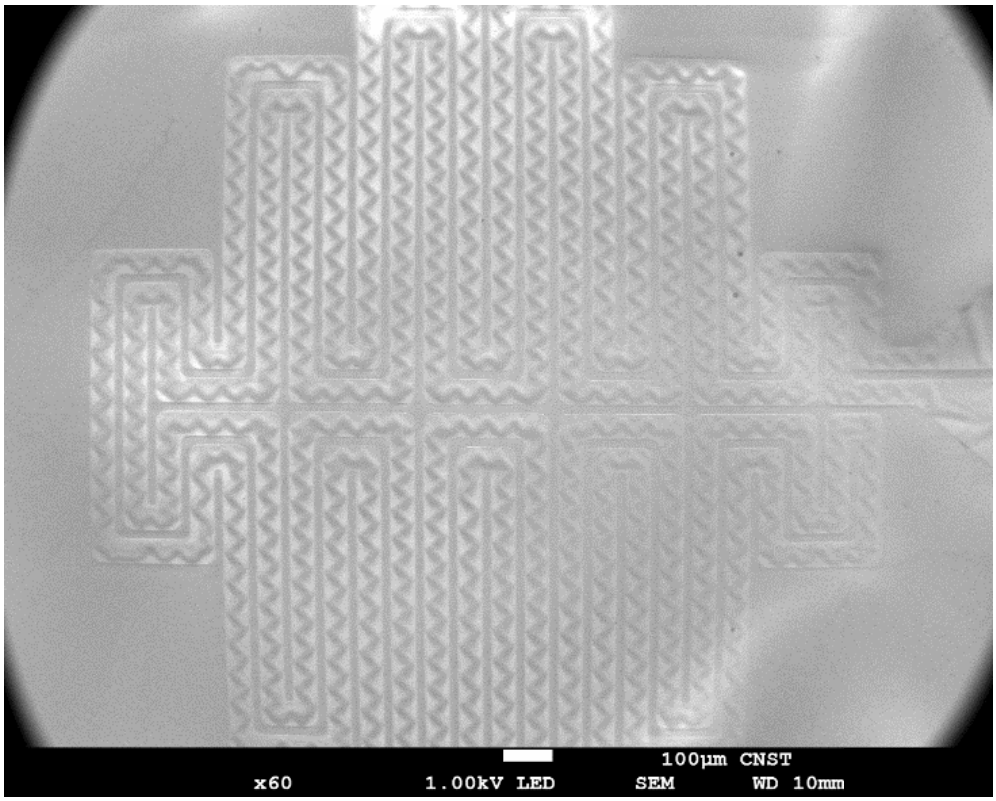


**Figure 2.4.** SEM image showing peel-up of insulating $SiO_2$ on top of Pt. The zig-zag pattern on top of the Pt traces is the $SiO_2$ buckling due to the poor adhesion to the Pt and the slight compressive stress of the $SiO_2$ film.

An additional 5 nm Ti adhesion layer was first added to the top of the blanket film of Pt in attempt to improve $SiO_2$ adhesion, but due to the oxidation of Ti in the presence of oxygen in the atmosphere, the films were harder to clean and prepare for the surface oxide. The recipe ultimately employed, with success, included the addition of an oxide seed layer, 50 nm either $SiO_2$ or $Al_2O_3$ which was deposited in the ion beam deposition (IBD) module without breaking vacuum on the wafer being processed. The incorporation of $Al_2O_3$ will be elaborated on in Section 2.4.4.

### *2.3.3 Lithography and etch-back to produce heater pattern*

The wafers were coated with hexamethyldisilizane (HMDS) in priming oven (Yield Engineering Systems, Inc.). The wafers were then coated with LOR5A and spun at 3000 RPM for 30 sec, baked at 175 ºC for 5 min, and cooled for 2 min. LOR5A was included to provide an undercut and minimize connection of the remaining Pt pattern to the redeposition of the etched material to the sidewalls of the photoresist during the ion mill etch step. Next, the wafers were coated with SPR 220 3.0, spun at 3000 RPM for 30 sec, and baked at 115 ºC for 90 s. The wafers were exposed with 220 mJ/ $cm^2$ (lamp intensity at 405 nm = 22.0 mJ/ $cm^2$, exposed for 10 s) using a 100 µm alignment gap in soft contact mode. (The alignment gap and soft contact mode were larger than normal to keep the masks cleaner when processing several wafers at the same time. Future generations should use a smaller alignment gap for more accurate heater dimensions.) A post exposure bake was done at 115 ºC for 90 s. The wafers were developed for 3 min in AZ 300 MIF with gentle agitation, and then they were rinsed with DIUF water. The step height of the resist was measured to be approximately 2.9 µm.

The wafers were etched with an ion mill at low power with cycles of 1 min etch and 4 min idle. The total etch should be roughly done with 80% of the time at a stage angle of 100º and 20% at a stage angle of 135º. A SIMS detector was used to monitor the etch rates and to estimate completion by etching though the last Ti adhesion layer. Slight over-etching into the fused silica substrate was preferred to make sure that all Pt and Ti was removed from between the traces.

### *2.3.4 Photoresist removal*

The cleaning procedure of the photoresist was modified over time and depended on the efficiency of the cooling stage in the ion mill and how much the photoresist would bake and the redeposition of the etched Ti, Pt, and oxide on the sidewalls of the photoresist. The general cleaning procedure is as follows. The wafers were placed, upside-down, in a wafer carrier in a large crystallography dish with PG Remover overnight. The wafer was then scrubbed gently with a cleanroom swab and then placed in a fresh bath of PG Remover. The bath was heated to 100 ºC for 10 min and then sonicated for 10 min. The wafers were scrubbed again with a cleanroom swab and checked under an optical microscope for any residual resist or metal that was redeposited on the side walls of the photoresist.

The wafers were then placed in either Nano-Strip for 30 min or cleaned in fresh piranha solution for 5 min. An additional cleaning was done in a downstream plasma asher (ULVAC Solutions ENVIRO-1Xa downstream plasma asher) for 1 to 2 min. The cleaned wafers were imaged in the JOEL SEM to make sure that there were no fabrication issues and that the were no visible remnant particles.

### *2.3.5 Etch processing to remove seed layer and round edges*

The wafers were then placed back in the ion mill and etched at low power for 5 min at a stage angle of 100º and then 2 to 5 min at a stage angle of 135º. A FIB SEM below in **Figure 2.5** shows the resulting rounded edges of the Pt film. Image taken from

analysis of Wafer 9 described later in Section 2.4.4. FIB SEM imaging was performed by Dr. Jacob Schumacher.

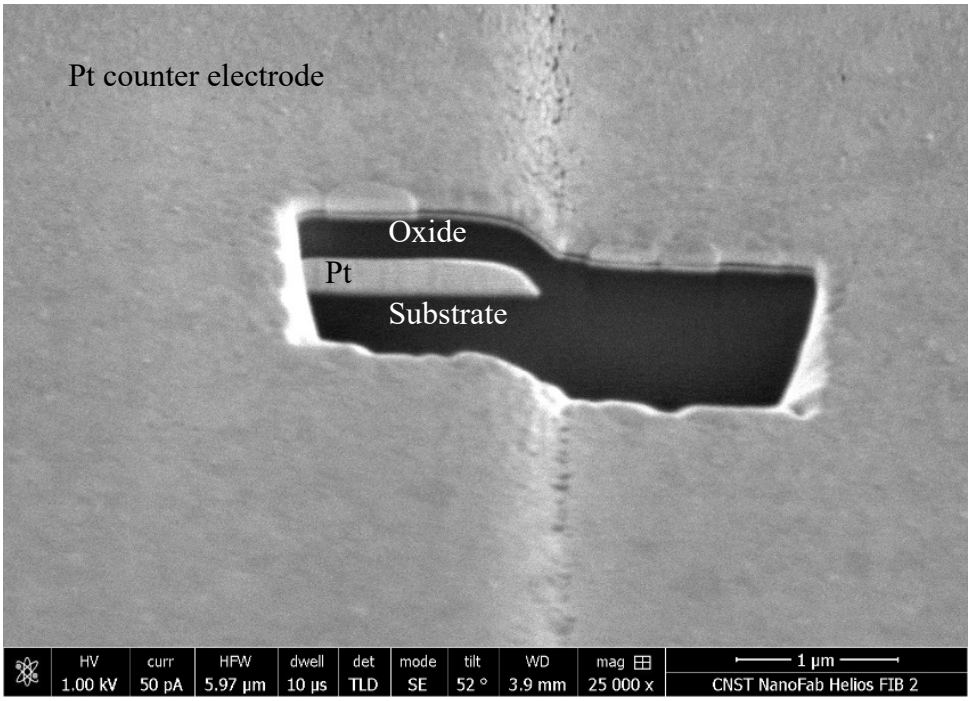


**Figure 2.5.** FIB SEM of side profile of embedded Pt thin film.

*2.3.6 Deposition of insulating oxides*

After optimization efforts, two main deposition methods were used to create a proper insulating layer. (1) Sandwich oxide with combining ALD, PECVD, and ALD or (2) a thicker PECVD layer that was annealed in the furnace. The characterization and selection of these oxide layers will be elaborated on in Section 2.4.

1) Before using the ALD tool, a preconditioning was done on a test wafer of 100 cycles of plasma $SiO_2$ (300° C, Plasma: 250 sccm Ar, 60 sccm $O_2$, 15 mTorr). Next, the wafer with the etched Pt film was coated with 500 cycles of $SiO_2$. A test Si coupon was placed on the outer edge of the wafer to monitor the

thickness of the oxide deposition via ellipsometric measurements (Wafer 8, 75.1 nm, n = 1.44740, MSE 1.367). The PECVD tool was also conditioned with a test wafer run 1 min and 34 s of 180 °C STD SiOx (1 mTorr base pressure, 150 °C spool and lid, 70 °C liner, and 180 °C electrode temperatures. Deposition step conditions: 5 mTorr, 56 sccm $O_2$, 20 sccm Ar, 28 sccm Ring $SiH_4$, 100 W Bias, 600 W ICP). The recipe was repeated on the subject wafer for a thickness of 204.9 ± 0.1 nm (n = 1.47204, MSE 10.4). If there was any film deposited in the ALD tool since the last $SiO_2$ deposition (by other facility users), the chamber was conditioned again for 100 cycles. Once conditioned, the subject wafer was placed back in the ALD tool for an addition 500 cycles of $SiO_2$ (Wafer 8, 75.4 nm, n = 1.45460, MSE 1.349).

2) The PECVD tool was also pre-conditioned by running a test wafer with the same recipe (STD SiOx). The deposition was set to 8 min and 56 s and the subsequent ellipsometric measurement confirmed a thickness of 993 ± 96 nm (n=1.46865, MSE 11.8). The wafer was then annealed in a nitrogen furnace at 800 °C for 1 h (Sandvik MRL Diffusion Furnace, Sandviken, Sweden).

### *2.3.7 Metal lift-off for surface electrodes*

Wafers were primed with HMDS, coated with LOR3A at 3000 RPM for 30 s, and baked at 210 ºC for 5 min. S1813 was then coated on top at 3000 RPM for 30 s and baked at 115 ºC for 60 s. Due to the fused silica substrate the exposure does was multiplied by 1.5 to be 135 mJ/cm$^2$. After exposure the wafers were developed in MF 319 for 60 s.

The step height was confirmed by profilometry to be approximately 1.8 µm. A descum process was performed on the wafers in the reactive ion etcher (RIE) for 2 min at 100 W. The Pt electrodes were deposited first with an e-beam evaporator (Denton Infinity 22 E-Beam, Morristown, NJ, USA) starting with a Ti adhesion layer (20 nm, 6.0 nm/min), and then the Pt electrode (200 nm, 6 nm/min). The wafers were placed in PG remover overnight to perform the metal lift-off. After scrubbing gently with a cleanroom swab, the wafers were placed in a fresh bath of PG remover at 100 ºC for 10 min and then rinsed with 1165, IPA, acetone, and water.

A similar process was employed for the gold working electrode, with a Ti adhesion layer (20 nm, 6.0 nm/min), and then the Au (200 nm, 6.0 nm/min).

### *2.3.8 Etch processing of contact pads*

Wafers were primed with HMDS and coated with SPR 220 3.0 at 3000 RPM for 30 s. Next, they were baked for 90 s at 115 ºC, exposed at 220 mJ/cm$^2$, baked at 90 s at 115 ºC, and developed in for 3 min in AZ 300 MIF agitating gently and then rinsed with DIUF water.

The bulk of the etching was performed with RIE. The chamber was conditioned for 5 min and then an etch rate was calculated for a 5 min etch (45 sccm $CHF_3$, 5 sccm $O_2$, 200 W, 50 mT). The wafer was then etched for 30 min and then in additional 5 min intervals until the multimeter could verify connection to the Pt contact pads by measuring a resistance of the embedded Pt. The wafers were then placed in the ion mill for additional ~ 5 min of etching to remove the remaining oxide and the top Ti adhesion

layer. The resist was removed with hot 1165 and then rinsed with DIUF. Completed microdevices are shown in **Figure 2.6**.

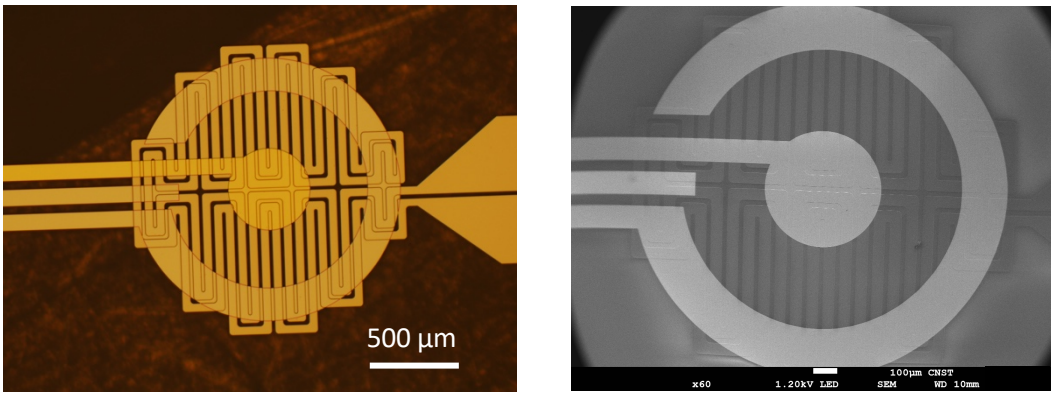


(a) (b)

**Figure 2.6.** (a) Optical micrograph and (b) scanning electron micrograph (SEM) of completed devices.[122]

## 2.4 Oxide optimization

The insulating oxide is of key importance to the performance of the device. The layer needs to be thin because when the embedded Pt thin film is functioning as a PRT, the temperature measurements should be as close to the actual temperature at surface electrodes as possible. Additionally, the layout is set up for future work with arrays, so the heating should be localized. When the Pt thin film is functioning as a resistive heater, then the oxide needs to electrically insulate the surface electrodes up to 20 V. On top of the thermal and electrical criteria, the oxide needs to withstand the piranha cleaning and incubating for long periods of time in salt containing solutions. During the operation of the platform, a 2.5 mm diameter well of buffer is placed on top of the

working area of the device; a single pinhole or defect in the insulating oxide can be penetrated by the ion-containing solution, resulting in an observable leakage current from the embedded Pt to the surface electrodes. Therefore, the film and resulting processing requires a high-quality insulation. $SiO_2$ was chosen for its high breakdown voltage (13-14 MV/cm),[124-126] high density, and its resistivity to piranha.

**Table 2.1** summarizes some of the available methods in the CNST cleanroom facilities for depositing $SiO_2$. PECVD films have the advantage of being produced at a fast deposition rate, but the films may have residual precursors. Often these films are annealed at high temperature in a nitrogen furnace to densify the films. Processing of initial protype platforms avoided temperatures above 300 °C because of concerns of Pt forming hillocks.[127] Later iterations confirmed that Pt/Ti hillocks are more common on silicon substrates and thicker Ti adhesion layers. Because the Pt thin film was on fused silica with a 5 nm Ti layer, the wafers could be heated up to 800 °C. For this reason, dry oxide films were not used. Sputtering films (e-beam evaporator with ion assist and cluster sputter) have been shown to be more porous and have larger grain boundaries. Because of the slow deposition rate of ALD, the film quality is higher and the coating is more conformal. Due to the 200 to 220 nm step height of the PRT and the need to insulate up to 20 V, at least 300 nm of conformal coating was set as the mininum thickness. Since ALD would take a long period of time (over 12 hours) and use a large amount of precursor in completing the full 300 nm in the ALD tool, sandwich oxides were considered.

**Table 2.1.** Summary of $SiO_2$ deposition methods.

| **Method** | **Temperature** | **Deposition Pressure** | **Precursors** | **Deposition Rate (nm/min)** |
|---|---|---|---|---|
| PECVD | 180 °C | 5 x $10^{-3}$ T | Ring $SiH_4$, $O_2$ (Ar) | 132 |
| E-beam evaporator with ion assist | ~155 °C | 5 x $10^{-6}$ T | $SiO_2$ in graphite crucible, $O_2$ | 18.0 |
| Cluster sputter | Cooling stage at 20 °C | 3 x $10^{-4}$ T | $SiO_2$ target, $O_2$, (Ar) | 2.3 |
| IAD | * same conditions as cluster sputter with etch gun on at gun 200 V, 60 mA, resulting in a slightly lower deposition rate | | | |
| ALD | 300 °C | 15-80 x$10^{-3}$ T | BTBAS, $O_2$, (Ar) | 0.15 nm/cycle |

*Information provided by CNST NanoFab staff members
BTBAS - bis(tertiarybutylamino)silane

To investigate the processing that yields the best quality $SiO_2$ films, several different methods of deposition were explored and evaluated. Some important factors affecting and determining $SiO_2$ quality are etch rate, refractive index, and film stress. The refractive index has been linked to both density and contaminations in the film. Impurities, for example, could be due to small amounts of precursors trapped in the film.

### *2.4.1 XPS analysis of trace impurities in oxides*

*XPS collection and analysis was performed by Dr. Kristen L. Steffens in the Biomolecular Measurements Division at NIST.*

XPS measurements were performed using a Kratos Analytical Axis-Ultra DLD X-ray Photoelectron Spectrometer with a monochromated Al Kα source (150 W) and a nominal analysis area of 300 × 700 $\mu m^2$, detected normal to the surface. The mono(Al)

x-ray source impinges the sample surface at an angle 60 degrees from the surface normal. Low resolution survey scans (160 eV pass energy, 0.5 eV step size) were obtained at each position. In addition, high resolution scans (20 eV pass energy, 0.1 eV step size) were measured for Si 2p, C 1s, N 1s, O 1s, F 1s, and Fe 2p. To prevent charging of the sample, the charge neutralizer (electron flood source) was on during the data collection. XPS curve-fitting and analysis was performed using CasaXPS software (v. 2.3.1PR1.0) including the CasaXPS Kratos relative sensitivity factor (RSF) library. Prior to fitting peaks with a 70% Gaussian/30% Lorentzian peak shape, a linear background was subtracted. The binding energy scale was calibrated to the C 1s peak at 284.5 eV.

Samples that had available $SiO_2$ deposition temperatures below 300 ºC were tested and the corresponding ellipsometry data was collected. The thickness of the samples was chosen based on dimensions of sandwich oxide iterations. Samples included for analysis were as follows: silicon test wafer, cluster sputtered $SiO_2$ (103.76 nm, n = 1.48767, MSE= 2.146), PECVD $SiO_2$ (323.72 nm, n = 1.45644, MSE= 7.128), ALD $SiO_2$ (75.24 nm, n = 1.44898, MSE= 1.187), and ion assisted deposition (IAD) cluster sputtered $SiO_2$ (75.91 nm, n = 1.526, MSE = 2.072). Two spots from each sample were analyzed to obtain the relative silicon to oxide ratio as well as to detect any trace impurities. Representative spectra of the Si 2p and O 1s regions are shown in **Figure 2.7**.

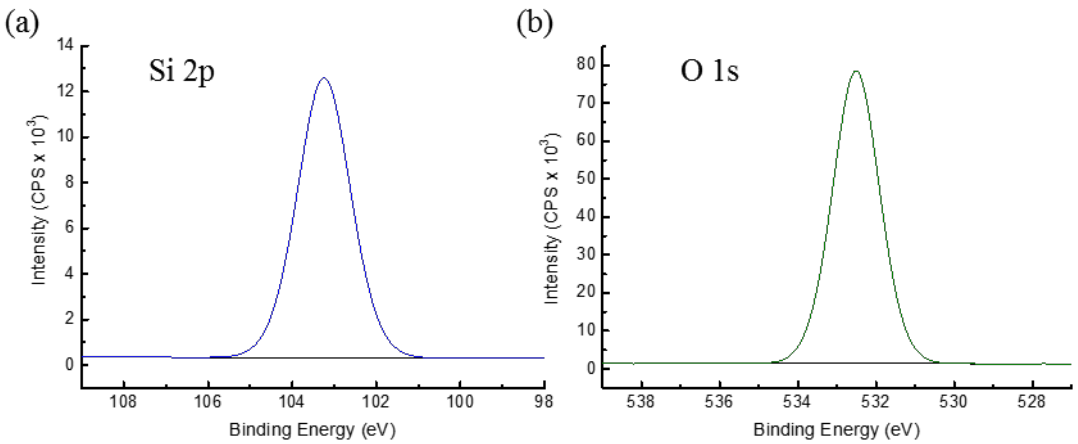


**Figure 2.7.** XPS regions of (a) Si 2p and (b) O 1s regions of a sample of ALD $SiO_2$.

**Table 2.2** displays the elemental analysis obtained by XPS. Samples were not sputtered clean prior to analysis, so surface oxide can still be seen on the silicon test wafer, and adventitious carbon appears on the surface of the films. The Si 2p spectra for deposited films show a single peak at 103.3 eV due to $SiO_2$ (**Figure 2.7a**). The Si($SiO_2$):O ratio for these films is 2:1, indicating stoichiometric $SiO_2$ within the expected accuracy of the XPS measurements.

**Table 2.2.** XPS component analysis of thin films.

| | C 1s % | F 1s % | Fe 2p % | N 1s % | O 1s % | Si 2p Si % | Si 2p $SiO_2$ % | Si($SiO_2$): O ratio |
|---|---|---|---|---|---|---|---|---|
| Silicon Wafer | 17.7 | - | - | 0.83 | 29.5 | 44.5 | 7.5 | 1 : 3.9 |
| | 17.0 | - | - | 0.71 | 29.7 | 44.9 | 7.6 | 1 : 3.9 |
| ALD | 7.5 | - | - | 0.43 | 62.4 | 0 | 29.6 | 1 : 2.1 |
| | 7.6 | - | - | 0.58 | 62.1 | 0 | 29.6 | 1 : 2.1 |
| Cluster Sputter | 8.3 | - | 0.19 | 0.29 | 61.0 | 0 | 30.2 | 1 : 2.0 |
| | 8.5 | - | 0.12 | 0.35 | 60.8 | 0 | 30.3 | 1 : 2.0 |
| IAD | 8.6 | - | 0.20 | 0.13 | 61.3 | 0 | 29.7 | 1 : 2.1 |
| | 8.0 | - | 0.12 | 0.21 | 61.4 | 0 | 30.3 | 1 : 2.0 |
| PECVD | 6.1 | 0.31 | - | 0.37 | 60.8 | 0 | 32.5 | 1 : 1.9 |
| | 5.8 | 0.32 | - | 0.60 | 59.9 | 0 | 33.3 | 1 : 1.8 |

XPS is a highly sensitive technique with the ability to detect both surface and film contamination. For the PECVD films, there were trace amounts of fluorine which could be due to contamination in the tool from $CF_4$, which is used along with $O_2$ plasmas for chamber cleaning. Trace amounts of Fe were found in the cluster sputter films and attributed to sputtering of the target shield material. Analyses led to the replacement of the grid set and adjustments of the gas flow through the deposition gun.

### *2.4.2 Probing electrical insulation*

One of the primary problems of the insulating films investigated was that they would fully insulate in air, but leakage current from the PRT to the surface electrodes could be detected when a droplet was applied to the surface. Water and salts can find small defects in the oxide and cause current leakage from the embedded Pt thin film to the surface electrodes. Initial iterations of the devices were fabricated to completion before testing. The “buffer test” as shown in **Figure 2.8** was instituted to test the insulation of

blanket films without having to perform lithography. As an example, for the sample probed in the picture in **Figure 2.8**, blanket films were deposited as described in Section 2.3.2 (5 nm Ti, 220 nm Pt), and then then two coupons of silicon test wafer were used as a shadow mask during the deposition of 75 nm of ALD $SiO_2$ and 320 nm PECVD $SiO_2$. Next small aliquots of buffer were pipetted on the top of the wafer. Using either probe tips attached to a multimeter, or tungsten probe station tips (**Figure 2.8**), one connection was made to the exposed Pt thin film and the second connection was made to the top of the buffer droplet, with care not to touch and puncture the film. The resistivity of the oxide should be high enough that a multimeter will read "open". If there is a pinhole defect, salts in the buffer solution can conduct electricity through oxide and the resistivity of the film will be low enough to measure, typically 1-35 MΩ.

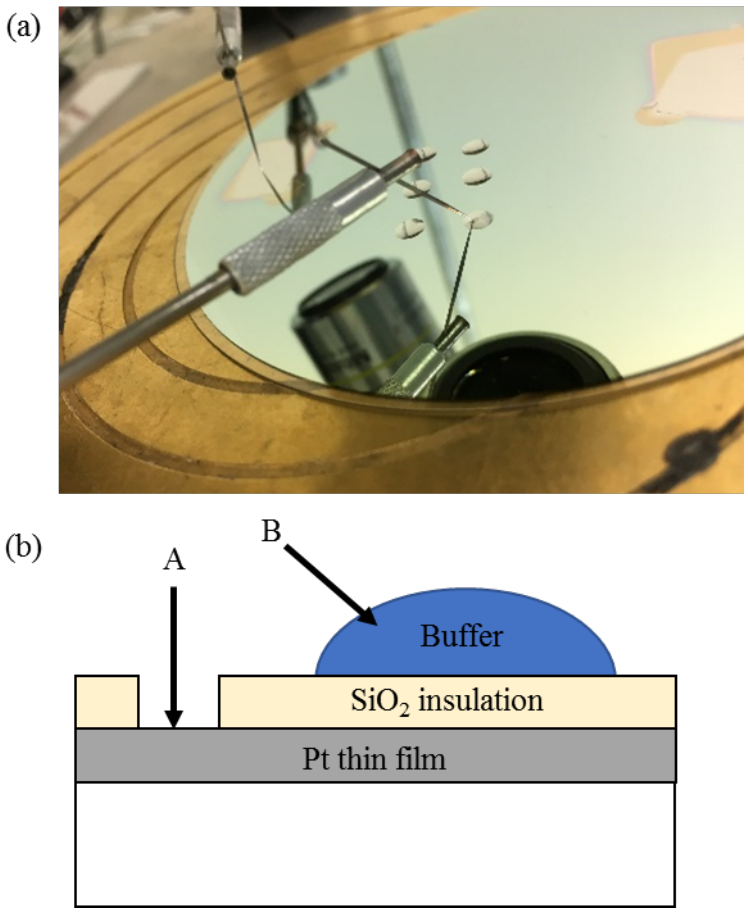


**Figure 2.8.** (a) Photo of "buffer test" performed with probing station. (b) Schematic of side profile of test films: arrows point to two connections (A & B) where a voltage is applied, and the resistivity is measured.

Sometimes the defects were visible, shown by the pinhole imaged by focused ion beam (FIB) SEM in **Figure 2.9**. The hole was most likely due to a particle that was present before the deposition of the Pt thin film and was coated over. Eventually stress (either electrical or chemical) may have caused the particle to leave, resulting in a void. FIB SEM imaging was performed by Dr. Jacob Schumacher.

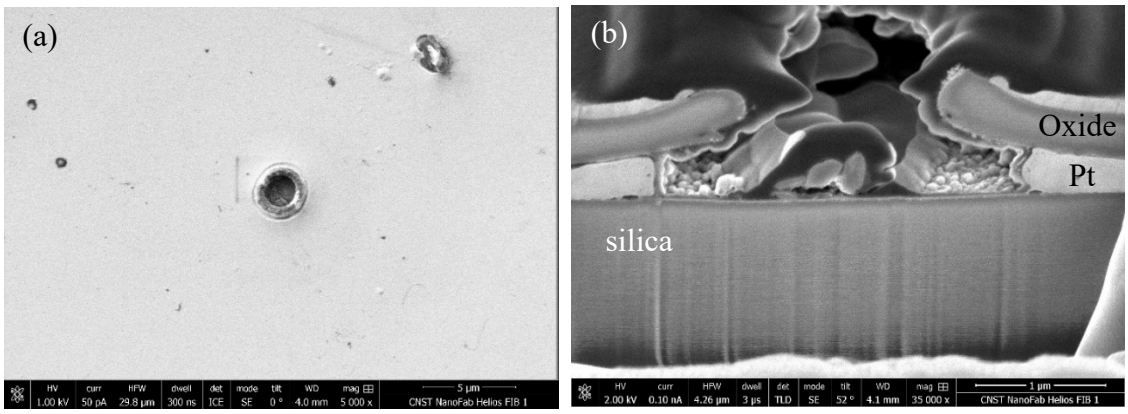


**Figure 2.9.** (a) SEM image of pinhole defect and (b) FIB SEM image of cross-section of defect.

### *2.4.3 Identification of defects*

Defects and impurities can come from the fabrication processing before, during or after the deposition of the oxide. In order to monitor the source of the visible defects, all devices were investigated with an optical microscope and a few devices from each wafer were imaged with SEM at each major step in the fabrication process. **Figure 2.10** shows SEM images of PRT traces before and after oxide deposition. Although lower magnification images are shown below, the traces were viewed, scanned, and examined under much higher magnification for the presence of particles and defects.

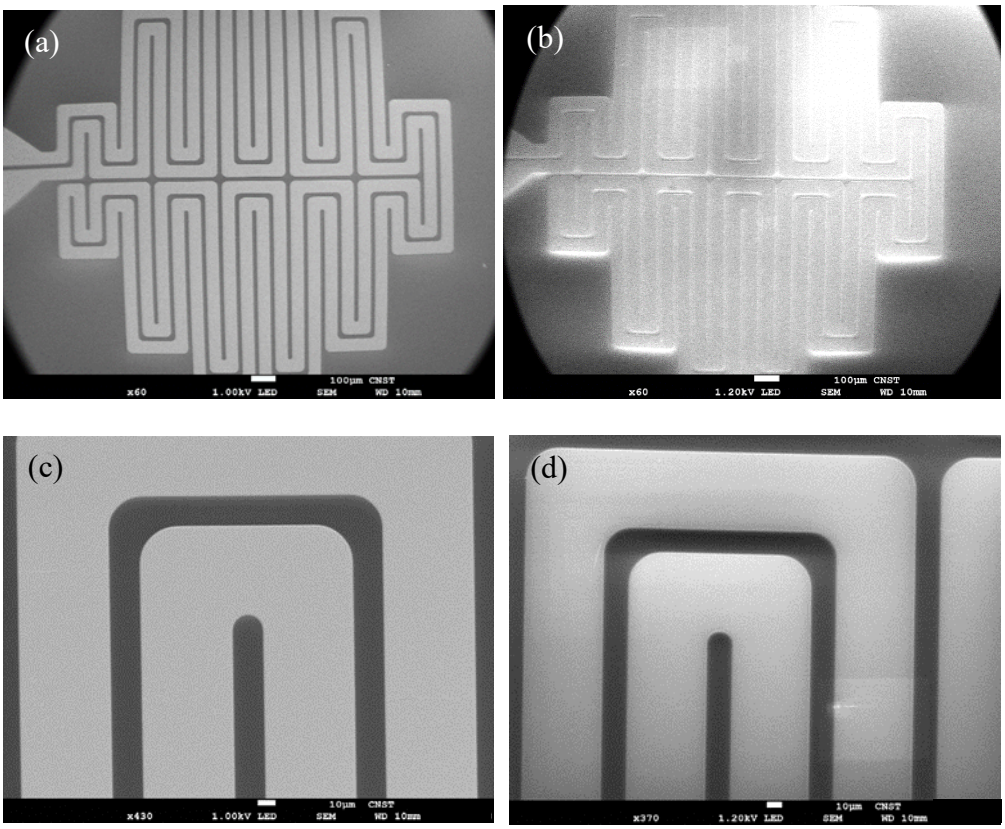


**Figure 2.10.** SEM image of device before (a and c) and after (b and d) oxide deposition.

### *2.4.4 Incorporation of $Al_2O_3$*

Additionally, there were concerns that electrical insulation issues might arise due to grain boundaries propagated from the Pt thin film, and poor adhesion. Aluminum oxide films have been shown to be pinhole-free and have been used as electronic device protection from salt containing fluids used with biomedical devices.[128] As a result, a thin layer of $Al_2O_3$ was incorporated to encase the Pt thin film. $Al_2O_3$ can etch in the presence of TMAH, a photoresist developer; therefore, it was not used on any of the outer layers so that TMAH could be used without concern for the process of depositing the surface electrodes. Because of the high dielectric constant of $SiO_2$,[124-126] the bulk

of the insulation consisted of $SiO_2$, but a thin film of $Al_2O_3$ was added at one of two places at the platinum-oxide interface: (1) in the cluster sputter deposition as a adhesion layer on top of the Ti/Pt/Ti stack (Wafer 8, **Figure 2.11a**), or (2) as another sandwich oxide, which involved depositing a conformal coating of ALD $Al_2O_3$ separately after the heater patterning and etching (Wafer 9, **Figure 2.11b**).

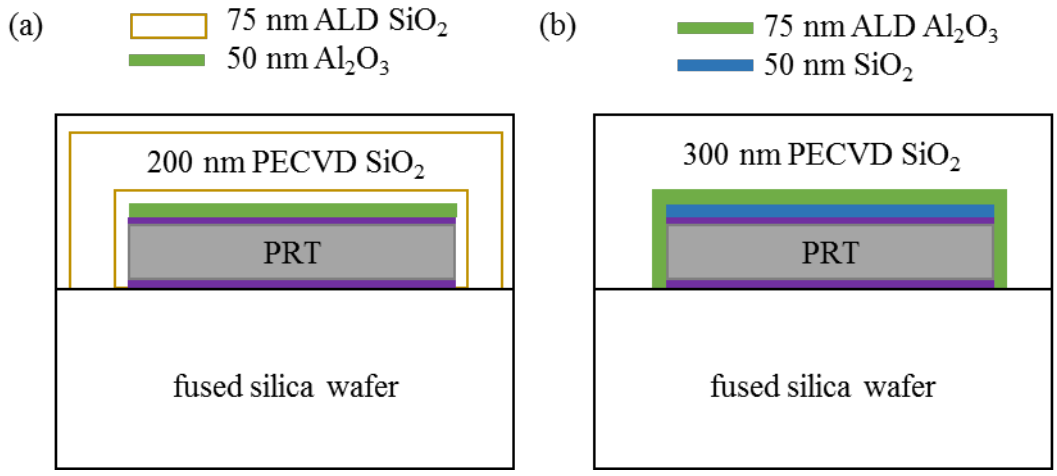


**Figure 2.11.** Oxide stacks with the incorporation of $Al_2O_3$ either as (a) a cluster sputter deposited adhesion layer or (b) a conformal coating deposited with ALD.

### *2.4.5 Stress-induced dielectric breakdown*

Lastly, after all processing precautions were taken, it was noted that some devices would insulate until stressed under the type of conditions experienced in operation. **Figure 2.12** shows an image of a device that was insulating properly and passed all previous quality checks. A drop of buffer was placed on top of the device and the heater was undergoing test ramping, when a current leakage was measured. Upon imaging the device, a defect was found on the reference electrode. **Figure 2.12b** shows the surface Pt of the reference electrode down to the embedded Pt thin film. The current passing

through the defect must have been high enough to melt the surface Pt and caused Pt to spread around the area of the device in a snow-globe like effect.

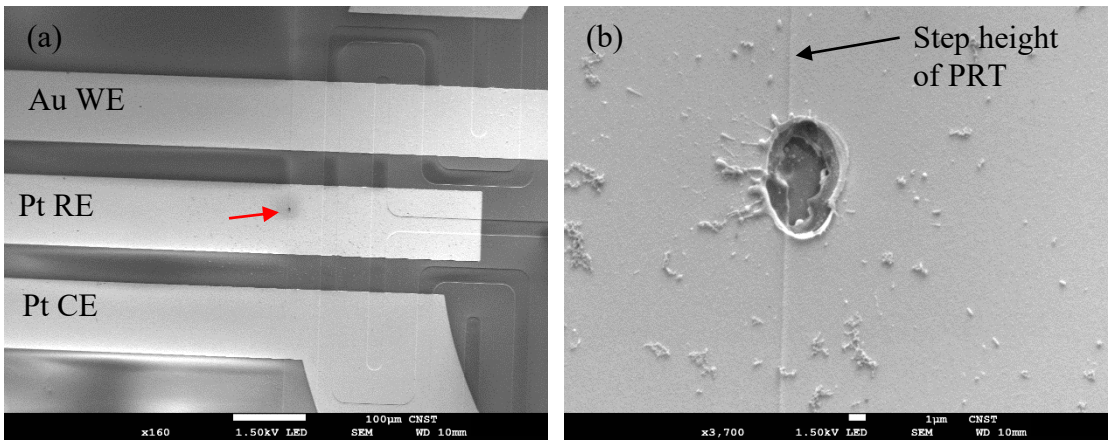


**Figure 2.12.** (a) SEM images of device defect (red arrow) due to arcing. Device components visible include: Au working electrode (WE), Pt reference electrode (RE), and Pt counter electrode (CE). (b) Higher magnification SEM image showing the melting of the surface Pt RE and exposing embedded Pt thin film.

On a separate device that had 75 nm ALD $Al_2O_3$ (Wafer 9, **Figure 2.11b**), a defect was identified as the location of a short circuit through a modification of the "buffer test" as shown in **Figure 2.8**. In this set up, small aliquots were pipetted on the completed device and once the buffer covered the pinhole defect, a resistance could be measured from the solution to the embedded Pt. SEM image was taken of the doughnut shaped defect (**Figure 2.13a**). Using the focus ion beam (FIB) SEM, a region of the device was etched to reveal the cross-section before the start of the defect (**Figure 2.13b**). Regions of the device were progressively etched, and an image the cross-section in the middle of the defect showed a gap between the oxide and the Pt (**Figure 2.13c and d**). It was hypothesized that the $Al_2O_3$ that could have been chemically

etched through a defect causing the gap to spread under the PECVD $SiO_2$. FIB SEM imaging was performed by Dr. Jacob Schumacher.

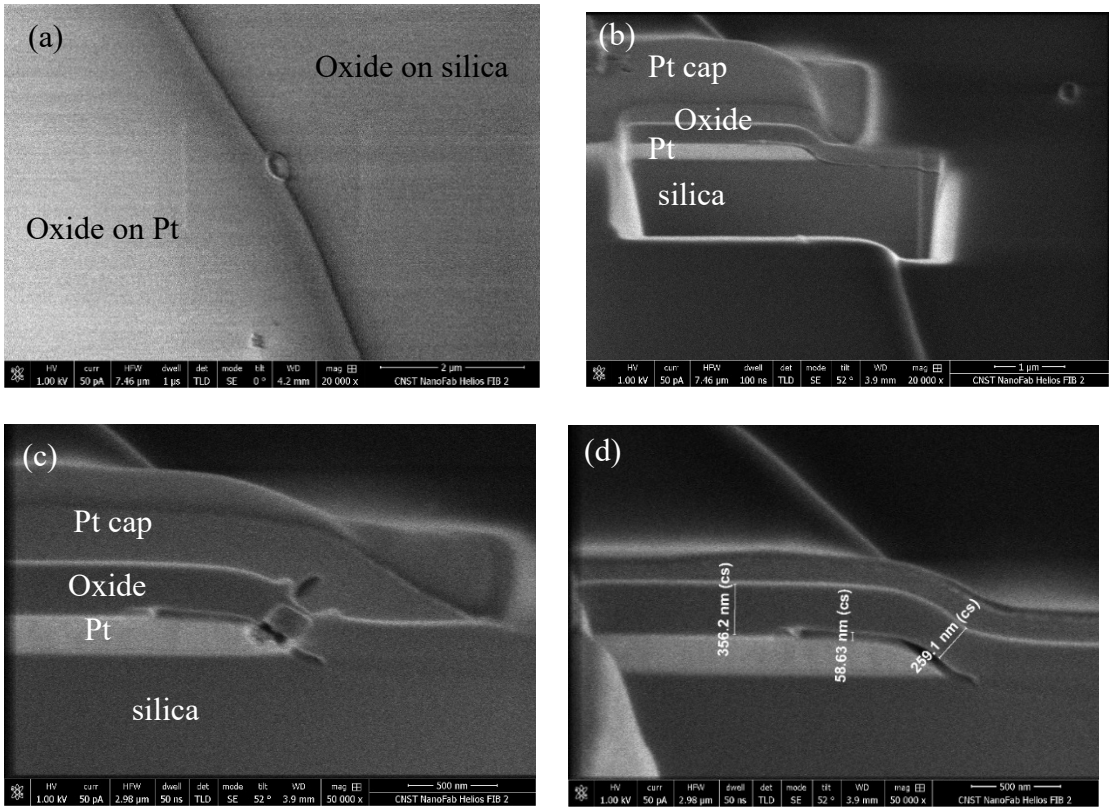


**Figure 2.13.** FIB SEM images of pinhole defect of Wafer 9. (a) Top view of the defect, (b) cross-section before, (c) during, and (d) after slicing through area of interest.

### *2.4.6 Thicker oxide layers and post anneals*

Due to the issues with the ALD/PECVD/ALD sandwich oxides and other oxides investigated, ALD, IBD, and PECVD films were characterized by measuring breakdown voltages using a mercury probe station by the CNST NanoFab staff. As expected, the ALD films had the highest breakdown voltages. Oxides annealed in a nitrogen furnace for 1 hr at 600 ºC, 700 ºC, and 800 ºC were also tested; films annealed at 800 ºC had the lowest leakage current and highest etch resistance. From these

conclusions and considering particle contaminants, a thicker insulator should encapsulate any small defects; as such, a 1 μm thick PECVD oxide was deposited on blanket Ti/Pt/Ti/$SiO_2$ films (as described in Section 2.3.2) to make sure there were not any large scale issues or stress concerns. From there the blanket films were annealed in the nitrogen furnace for 1 hr at 800 ºC. There were no observable concerns from the stress or annealing the embedded Pt thin film, so the oxide procedure was incorporated in the fabrication procedure described in Section 2.3.6.

## 2.5 Conclusions

The fabrication of electrochemical microdevices with sufficiently robust insulating layers was achieved through sandwich oxides, or thicker films and annealing steps. The films with 1 μm of annealed PECVD $SiO_2$, provided the best insulation for devices needed to be used for resistive heating. Although the failure mechanism is still unclear, the lifetime of the insulation was still not as long as expected (less than 10 to 12 thermal profiles). With the incorporation of the thermoelectric module discussed further in Chapter 3, the devices that have leakage current that would cause electric interference in the electrochemical measurements (when using the embedded microheater for temperature control) could still be used with thermoelectric heating as long as the current through the PRT is negligible (i.e., no applied voltage).

While a thinner annealed insulating layer could potentially be developed with further optimization, increasing the thickness from a 350 nm sandwich oxide to the 1 μm thick non-sandwich oxide does not seem to make a noticeable difference in the

overall performance of the platform. **Figure 2.14** summarizes the versions of the oxide stack that were used in the assembly presented in Chapter 3 and the analysis in Chapters 4 and 5.

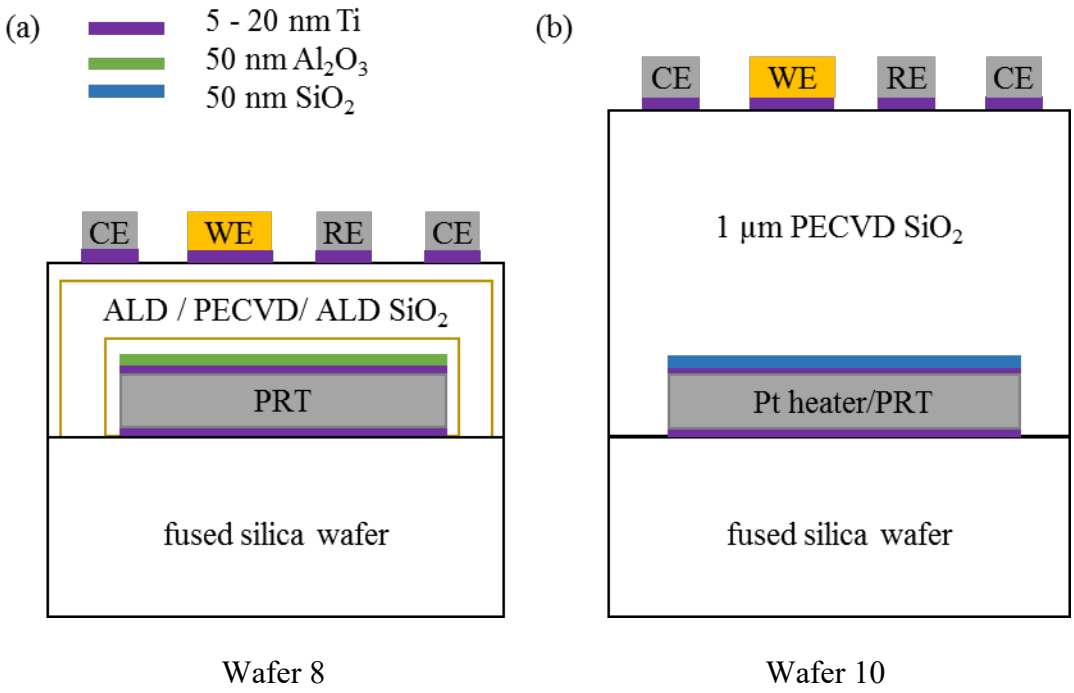


**Figure 2.14.** Summary of device dimensions referenced in later chapters. (a) Wafer 8, devices from this generation were used for thermoelectric controlled devices in Chapter 4. (b) Wafer 10, devices from this generation were used for resistive heating in Chapter 4 and thermoelectric controlled devices in Chapter 5.

One of the long-term goals of the platform is to build systems with larger arrays. The design of the device layout on a full 4-inch wafer (**Figure 2.15**) was set up so the platform was amenable to an array format. As seen by the image, the pattern has devices in 2 x 1 and 2 x 2 arrays as designed by Dr. Zuliang Shen.[123] Currently only 2 x 1 arrays have been tested and will be discussed in Chapter 3. However, while work here was

focused on having ample research samples to test the feasibility of measurements on biomolecular stability, it is easy to see the layout could be configured to create arrays with larger numbers of elements.

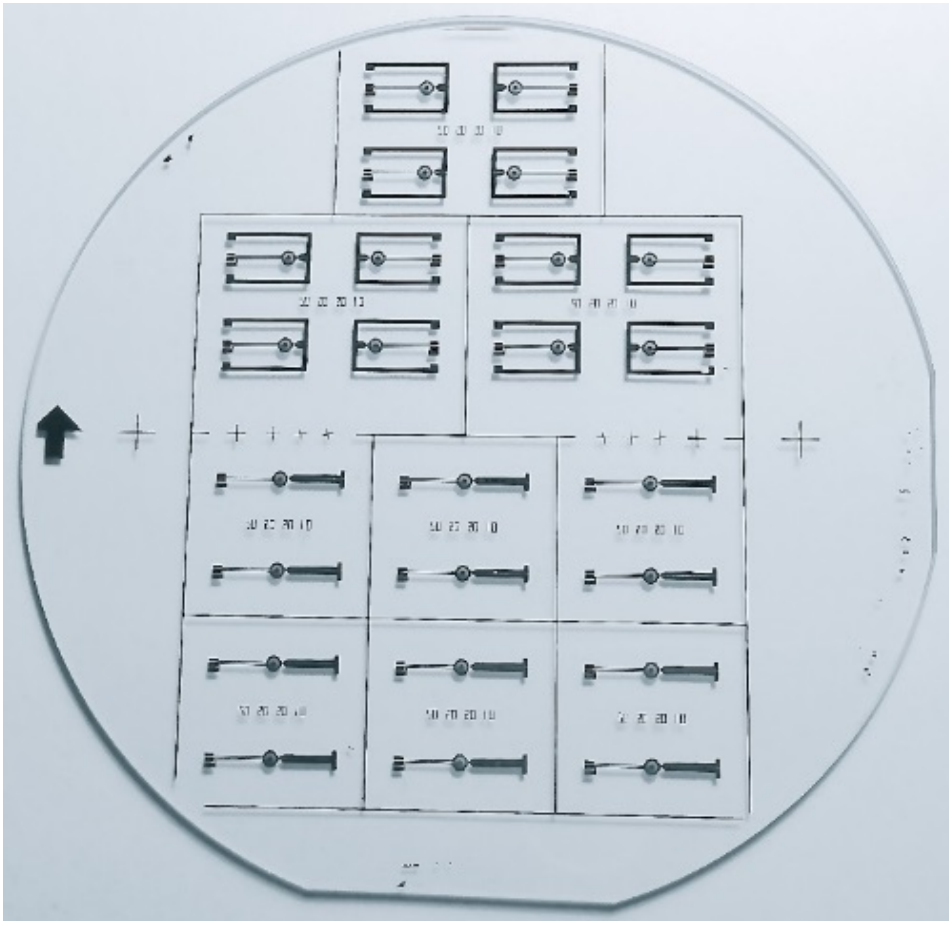

**Figure 2.15.** Image of full wafer of completed devices.

# Chapter 3 Assembly, Calibration, and Automation

*Christopher Montgomery assisted in the mounting and wire bonding of the devices. Operational software was developed in collaboration with Dr. Jon Askim.*

## 3.1 Overview of platform assembly

When developing a platform that is scalable to HTS, incorporation of devices that are mounted on printed circuit boards (PCB) and can easily be connected to commercial electronics is an important aspect that narrows the gap between an experimental prototype and something that can be adopted and scaled up to commercial usage. Additionally, having automated program control over the device performance increases measurement repeatability and also facilitates the operation of more than one device simultaneously.

Previous work with a similar platform showed that the devices could be mounted to custom PCBs, but the experimental setup used required manual increases to the source measure unit (SMU) providing voltage to the resistive heater.[22, 123] All current values of the heaters were recorded manually before increasing to the next voltage set point. Additionally, each electrochemical experiment was initiated manually, saved, and then moved to the next voltage set point. These earlier results were able to highlight the potential of the platform. The work described in this chapter addresses improvements to the assembly and incorporation of programmatic control. The new programming provided real-time feedback of device temperature, automatic control of temperature ramping, and the addition of a software controlled proportional-integral-

derivative (PID) loop to allow for temperature rather than voltage set points. To achieve temperatures below room temperature without the need of a refrigeration box, and to use devices that had some leakage current (between the heater and surface electrodes), a thermoelectric heat pump was also incorporated (Sections 1.4.1 and 3.5).

## 3.2 Cleaving and mounting devices

Previously the completed wafer was diced into individual devices with a dicing saw. Due to observation that some devices had proper electrical insulation until being diced (potentially due to the oxide cracking from mechanical stresses), the method of separating the individual devices was switched to a method that provides less strain on the films. Prior to cleaving or dicing, the wafer was coated in a blanket photoresist to protect the surface of the device. The wafer was divided into individual devices by scoring with a diamond scribe and cleaving with wafer cleaving pliers. Afterwards, the photoresist was removed with acetone, IPA, and rinsed with DIUF. Once the devices were cleaned, the devices were mounted and assembled based on the procedures described in Sections 3.4 and 3.5.

## 3.3 PRT calibration[122]

The electrical resistance of Pt has a linear dependence on temperature (≈1 °C/Ω) in the temperature range of our experiments. With both assemblies, the embedded Pt thin film was used as a platinum resistance thermometer (PRT). Each PRT was calibrated independently due to the small center-to-edge difference in uniformity of the Pt deposition, which caused slight variations in the resistance values from device to

device. For calibration, the device was placed in a convection oven (Cole-Parmer Stable Temp 52412-78, Vernon Hills, IL, USA), and the temperature was increased in 10 °C increments and allowed at least 20 min to equilibrate at each temperature point. Two type K thermocouples (Omega HH501BK) were used to probe the temperature inside the oven and obtain an average temperature at each set point. The associated Pt resistance vs. temperature was determined from current measurements from a SMU (B2902A Keysight Technologies, Santa Rosa, CA, USA) at 0.5 V. The resulting linear least squares fit of the calculated resistance vs. measured temperature was used to report temperatures from resistance measurements made during the melting experiments (**Figure 3.1**).

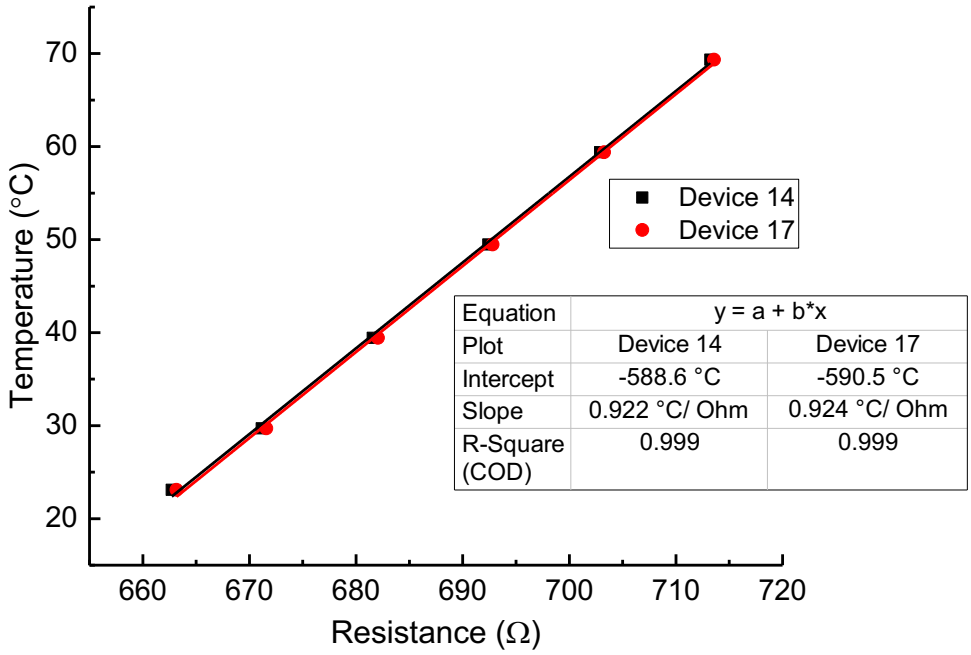


**Figure 3.1.** Example calibration curve of Pt microheater/PRT.[122]

## 3.4 Platform assembly: resistive heating[122]

A 6 mm hole was milled through the custom PCB centered under the device mounting location to reduce thermal anchoring by providing an air gap on the back of the device and to also allow contact of a thermoelectric device to the backside of the wafer (Section 3.5). Completed wafers with 1 µm PECVD $SiO_2$ were diced into individual devices and mounted on the PCB with epoxy. The leads of the device were wire bonded to PCB traces for easy electrical connection. A picture of the assembled platform can be found in **Figure 3.2**.

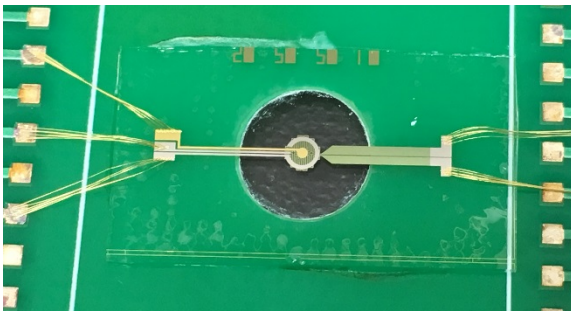

**Figure 3.2**. Top view of mounted device with airgap.

## 3.5 Platform assembly: thermoelectric heating[122]

Devices fabricated with 350 nm $SiO_2$ (Chapter 4) and 1 µm SiO2 (Chapter 5) were used for the thermoelectric heating studies with the Pt thin film used as the PRT for temperature monitoring. As described previously, a 6 mm hole was milled through the PCB and the completed device was secured to the board with epoxy so that the hole in the PCB was centered under the PRT. Room-temperature-vulcanizing (RTV) silicone pillars were placed on an aluminum block heat sink with two screws on either side of the PCB for securing the back side of the glass wafer at the height of the thermoelectric

module (Peltier MS2,010,06,06,11,11,00,W2, Laird Technologies Inc., Chesterfield, MO). A picture of the assembled platform can be found in **Figure 3.3**. The thermoelectric module was placed on an aluminum block and the PCB was screwed in place on top to ensure efficient heat transfer between the thermoelectric module, the backside of the wafer, and the aluminum heat sink. Dow Corning 340 (Dow Chemical Company, Midland, MI, USA), a silicone heat sink compound, was used at the interface between the fused silica wafer and the top of the thermoelectric.

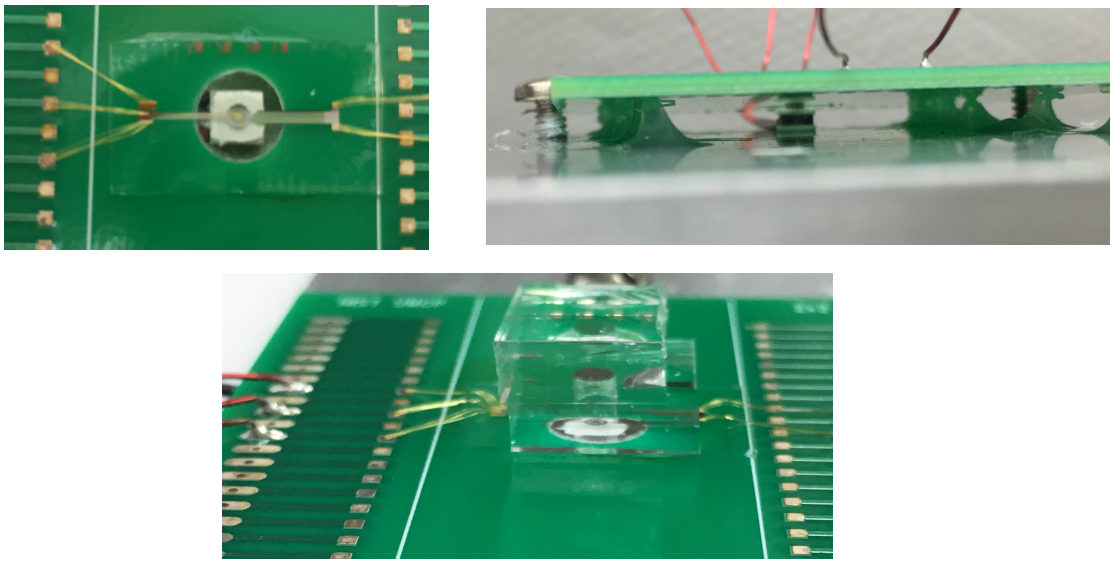

**Figure 3.3.** Images of mounted device with TE on backside.

## 3.6 Automation

Previous measurements were performed by manually increasing the voltage on the SMU, measuring the current, and then running the SWV procedure. Even with monitoring the time and stepping the voltage at set intervals, there was some inherent variability induced by the manual procedure. To minimize measurement error and increase repeatability, a software program (the electrochemistry control program, ECP) was created to control the source meter and potentiostat.

### *3.6.1 ECP Version 1: voltage control*

The initial version of the ECP controlled two channels on the SMU and one channel on the potentiostat. The display showed the electrochemical response and a baseline correction. The summary table included the last temperature before the electrochemistry step, the peak current, and the peak potential (**Figure 3.4**).

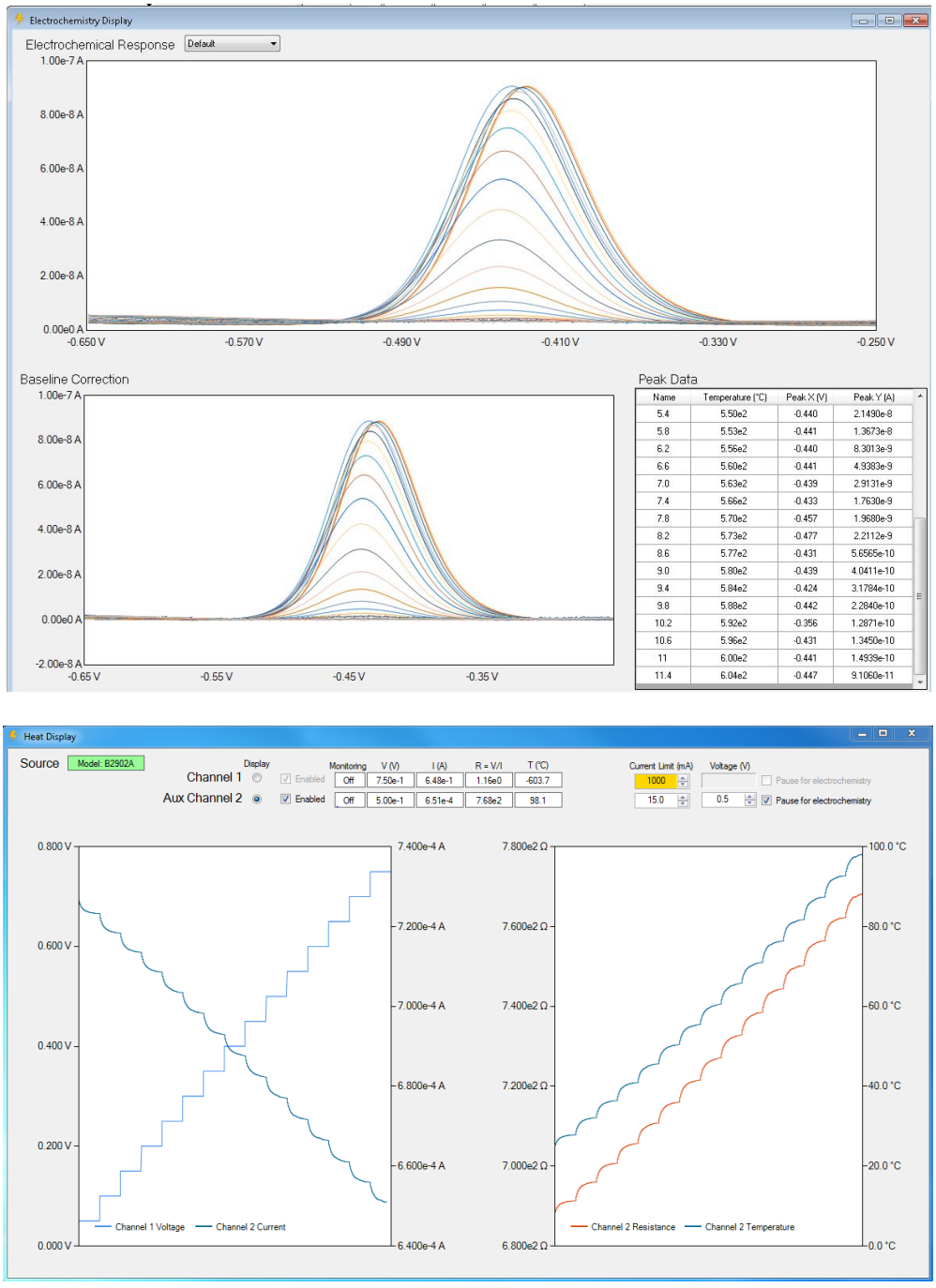


**Figure 3.4.** Version 1 program display. Screenshots are of representative experiments: (top) electrochemical display of early resistive heating experiment and (bottom) heat display of thermoelectric controlled test experiment.

#### *3.6.1.1 Resistive heating*[122]

A mounted device was placed in a polystyrene foam box with an ice pack and allowed to equilibrate for 30 min before analysis. A SMU supplied a voltage for resistive heating and also monitored the current through the Pt heater (thereby permitting temperature monitoring). A voltage of 0.5 V was initially used to monitor the temperature during the equilibration time, then the voltage was increased by 0.4 V every 15 s from 1.0 V to 11.4 V to produce the stepped temperature ramp for the melting experiments described in Chapter 4 with resistive heating.

#### *3.6.1.2 Thermoelectric heating*[122]

The SMU supplied a voltage for heating or cooling of the thermoelectric module, and also monitored the current of the PRT on a separate channel. The sample was allowed to equilibrate at room temperature for 15 min; during that time, 0.001 V was applied to the thermoelectric module and 0.5 V to the PRT, allowing for temperature monitoring. To reach 10 °C, 0.2 V was applied for 20 min, and then for the heating cycle, the voltage was stepped by 0.25 V every 25 s from 0.2 V to −0.4 V. The PRT was monitored at 0.5 V for all temperatures, and this monitoring was terminated before each measurement of the electrochemistry program to minimize any leakage current. The thermal profile with voltage control is shown in **Figure 3.5**. This procedure was used for the thermoelectric cooling and heating melting profiles shown in Chapter 4.

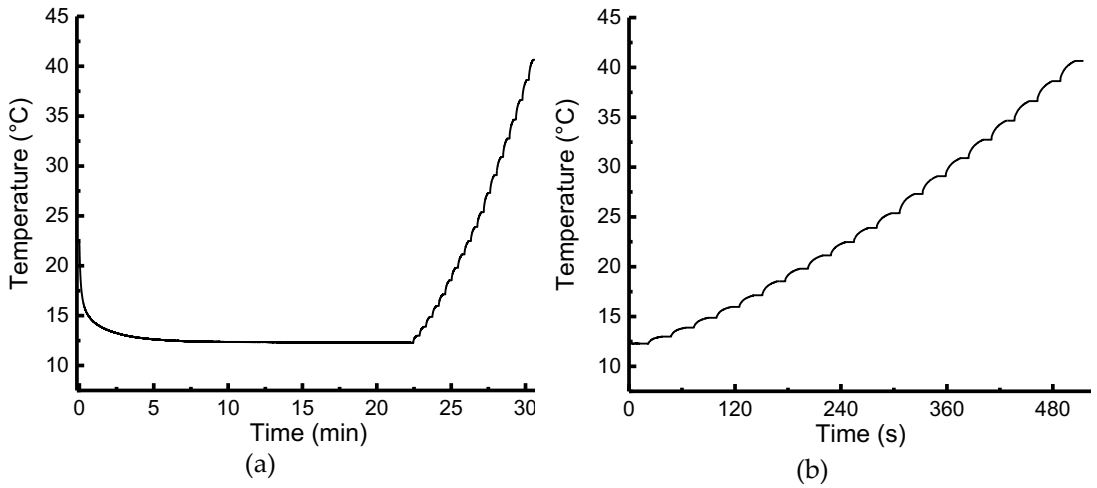


**Figure 3.5.** (a) Full temperature program of platform in a melting experiment with 20 min of cooling at 0.3 V applied to thermoelectric, and (b) an expanded view of the melting portion of the experiment. The voltage was stepped by 0.25 V every 25 s from 0.3 V to −0.3 V.[122]

### *3.6.2 ECP Version 2: two devices*

When using the thermoelectric and the PRT, each device needs two source channels to control and monitor temperature; to run two devices, four channels are needed. The SMU only has two channels, so an additional source unit (E36313A Keysight Technologies, Santa Rosa, CA, USA) was incorporated to power the Peltier modules, while the SMU was used to monitor the PRT. Negative voltages were required to induce cooling in the thermoelectric module; the source used was only capable of applying a positive voltage, so a relay control was used to reverse current polarity when necessary.

### *3.6.3 Program Version 3: PID controller*

Versions 1 and 2 of the ECP used a fixed voltage ramp; that is voltages applied to the thermoelectric module were pre-programmed, and monitored temperatures had no

effect on what voltages were applied. Due to each device having slightly different resistances and the existence of slight variabilities between Peltier modules, however, this fixed voltage ramp resulted in variations in the thermal responses between different devices. Additionally, the voltage ramps were generally linear and did not give a completely uniform heating rate (**Figure 3.5**), which is desirable when analyzing a melting profile. To address this issue, a proportional integration derivative (PID) controller was incorporated in the software program to control the voltage applied to the thermoelectric module via feedback from the PRT. Standard optimization procedures were performed to determine the proportional, integral, and derivative coefficients for each ramp, placing a priority on roughly minimizing temperature overshoot (at the cost of increased equilibration time). **Figure 3.6** shows the new temperature ramp allowing 15 s at each 1 °C step to equilibrate.

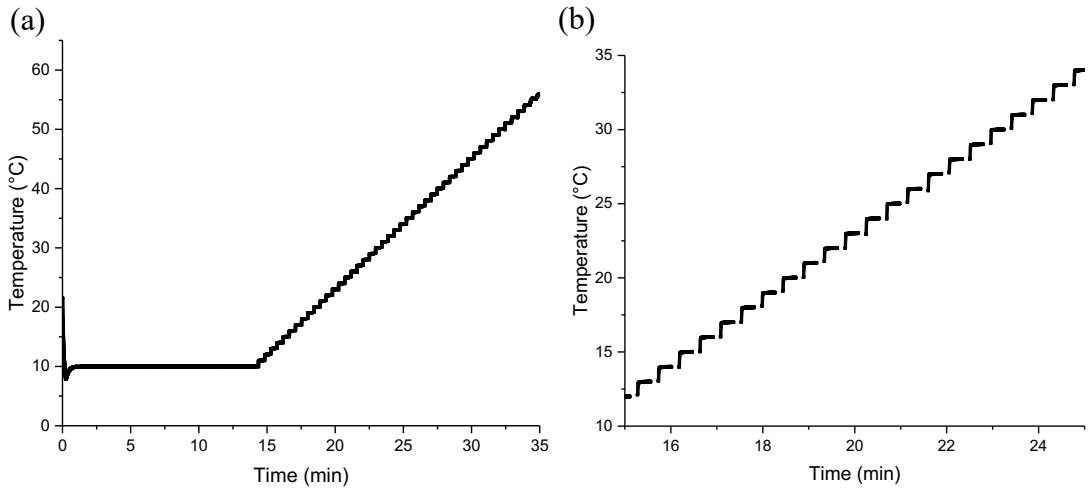


**Figure 3.6.** PID controlled temperature ramp: (a) full view and (b) enlargement on 10 min of thermal profile. Addition of the PID dramatically increased the linearity of the temperature ramp.

## 3.7 Conclusions

The inclusion of automated control increased the amount of data that could be collected and reduced measurement variability. The automation also allowed for real-time feedback of device temperatures. Development of a 2-device program doubled data collection and set the framework for larger arrays; additionally, while only SWV electrochemical programs were ultimately used, the program was also set up to run several other broadly-useful electrochemical programs. Currently, the primary limitation of the setup is rooted in the number of available channels used to monitor the PRT, drive the thermoelectric module, and perform electrochemical experiments; a specially designed hardware setup to run a large number of devices is feasible and readily achievable.

The currently used potentiostat (CHI1040c, CH Instruments Inc., Austin, TX, USA) has a limitation of 8 simultaneous channels. Future work would be greatly improved by fully utilizing these 8 channels; this would require 8 simultaneous source channels to drive the thermoelectric modules, and a timed routing scheme to allow the SMU to measure the PRT channels pseudo-simultaneously (e.g. using a microcontroller switching rapidly between channels using MOSFETs as switches).

# Chapter 4 Measuring Ligand-Induced Stabilization of Duplex DNA

Portions of this chapter have been published in the following publication[122]

Sarah M. Robinson; Zuliang Shen; Jon R. Askim; Christopher B. Montgomery; Herman O. Sintim; Steve Semancik. Ligand-based stability changes in duplex DNA measured with a microscale electrochemical platform. *Biosensors*, **2019**, *9*, 54, doi: 10.3390/bios9020054.

*My contribution to the publication is the majority of the written analysis, as well as fabrication of the devices, testing the program automation, sample preparation, data collection, and data analysis.*

## 4.1 Introduction

Many small molecules (i.e., ligands) that bind to DNA have been investigated as anti-cancer therapeutics.[129-131] Starting with the discovery of the changes in bone marrow caused by mustard gas poisoning in as early as 1917, advances related to the binding of ligands to DNA have continued over the last century.[132] Topoisomerases are critical to DNA transcription and replication.[133] Molecules that interact with duplex DNA breaks while bound to topoisomerases can cause replication miscoding or prevent the proper processing of supercoils in DNA, and therefore can be used as anticancer or antibacterial drugs.[133] Duplex DNA binders, such as doxorubicin and daunorubicin, have already yielded clinical successes for the treatment of cancers such as breast

cancer, esophagus cancer, liver cancer, osteosarcomas, non-Hodgkin's lymphoma, and acute myeloid leukemia.[134-136] On the other hand, DNA binding compounds cause mutagenicity, so, if duplex DNA is not the intended target, binding could also cause undesired toxicity effects.[137]

DNA has shown to form a wide range of structures. Most common structures of duplex DNA are the A-form and B-form, right-handed helixes.[138] The Z-form is less common and the resulting helix from alternating anti and syn glycosyl bonds yields a left-handed helix.[138] Other DNA structures that are naturally occurring, such as G-quadruplexes, will be discussed in more detail in Chapter 5.

### *4.1.1 Ligand binding*

There are several different binding modes of small molecules to duplex DNA as displayed in **Figure 4.1**. Ligands can bind to the minor grooves of DNA. Typically these ligands are crescent shaped that can hydrogen bond with the exposed portions of the base pairs, such as the N3 of adenine and the O2 of thymine.[138] The binding of these ligands also can be highly sequence-dependent which allows for some selectivity of binding. For example, diminazene aceturate (DMZ or Berenil) binds to sequences with AT-rich regions.[139] It has also been shown to have a secondary binding site of CG-rich sequences.[140] Ligands that have aromatic rings in planar structures can intercalate between the base pairs and are stabilized by pi stacking with the aromatic rings of the base pairs. Common intercalating ligands are proflavine, daunomycin, and doxorubicin.[134]

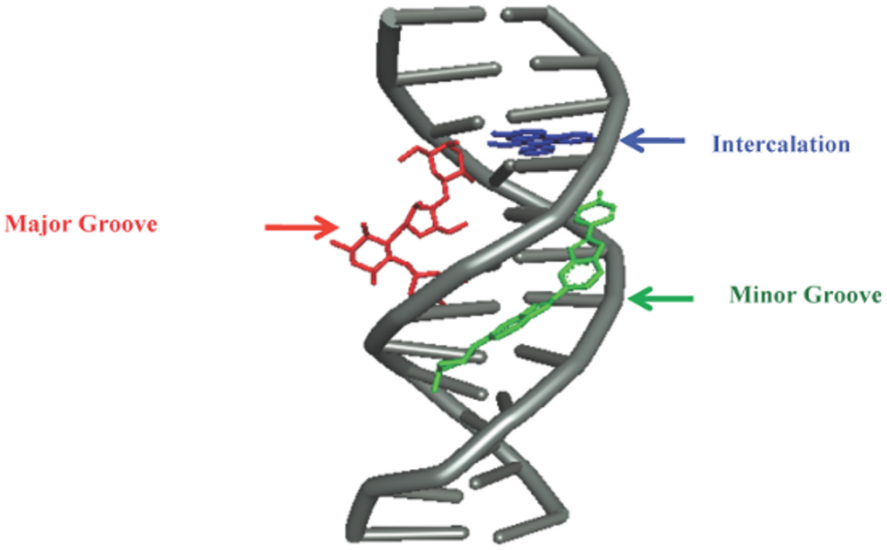


**Figure 4.1.** Binding modes of ligands to duplex DNA.[138] [Reprinted from Bhaduri, S.; Ranjan, N.; Arya, D. P. *Beilstein J. Org. Chem.* 2018**,** *14,* 1051–1086. doi:10.3762/bjoc.14.93. Published by The Beilstein Journal of Organic Chemistry and licensed under CC BY 4.0.]

Utilizing the concept of ligand binding, fluorescent displacement assays are also used to look at relative selectivity of ligands binding to DNA.[141] In this case, when a fluorophore binds to a target the fluorescence increases.[141] When the fluorophore is displaced by a molecule that can bind stronger, the fluorescence decreases.[141] Fluorescence based assays can be limited to screening molecules that do not have inherent fluorescence or interact with the fluorophore. Electrochemical approaches are a great alternative since potential drug molecules do not tend to have a redox active component in the same region as many commercially available redox tags. A range of electrochemical approaches to understand anticancer drugs interaction with duplex DNA has been reviewed by Rauf and coworkers.[142]

### *4.1.2 Surface chemistry*

Using the foundations and well-established methods for preparing DNA-modified electrodes, the procedure for immobilizing duplex DNA for analysis in this chapter is shown in **Figure 4.2**. The steps of this procedure are as follows: (a) First the gold surface must be cleaned. When one employs large macro disk electrodes, this is commonly done by mechanical polishing with an alumina slurry. With fabricated planar electrodes, cleaning is typically limited to chemical and electrochemical means.[143-144] Piranha solution is commonly used as a cleaning solution because the mixture of sulfuric acid and hydrogen peroxide forms a super acid, which acts as a strong oxidizer that produces very clean surfaces. One major benefit, and also a limitation with piranha, is that it will oxidize most organic materials, and therefore photoresists, polydimethylsiloxane (PDMS) wells, and other lithographic materials used to contain solutions. UV-ozone cleaning is a milder alternative but requires an ozone generator, and the films are not always as free of impurities. (b) Herne and Tarlov pioneered DNA assembly and characterization of probe sequences tethered with thiol linkers.[12-13] In the early 2000s, Plaxco and coworkers developed these technologies further, outlining a protocol that uses methylene blue (MB)-labeled DNA for electrochemical DNA (E-DNA) sensors.[17] Research in the application of thiol-modified DNA on gold surfaces has expanded to a variety of applications.[15, 18-19, 21] (c) After immobilization of DNA, backfilling with 6-mercaptohexanol (6-MCH) has been shown to minimize nonspecific adsorption of DNA to the gold surface.[12] (d) Lastly, the sensor is incubated with a complementary DNA sequence that is labeled with MB.

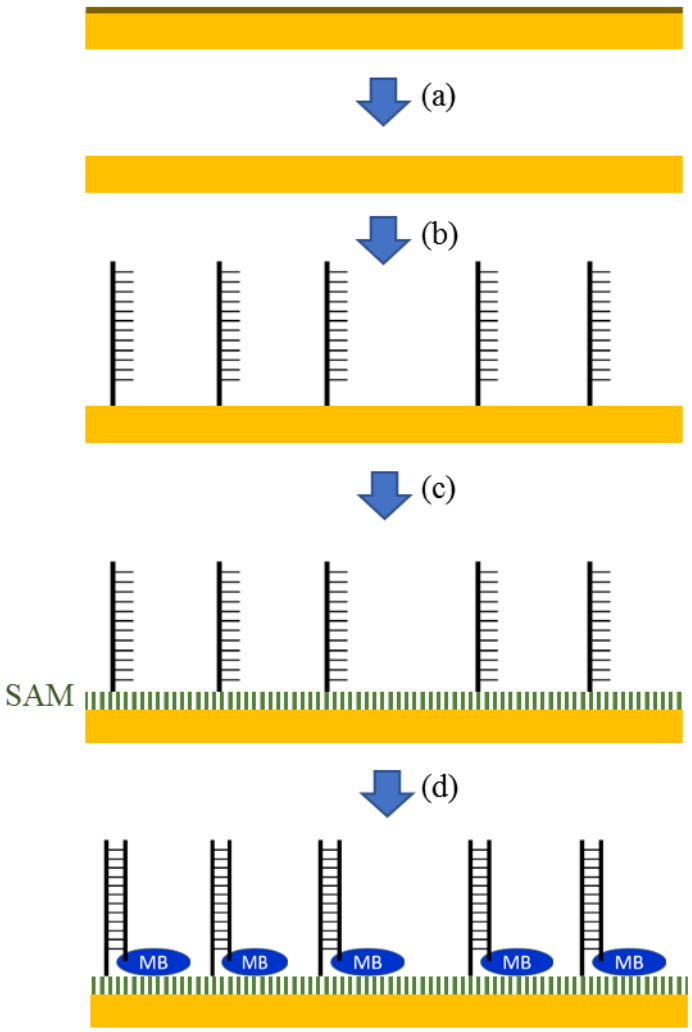


**Figure 4.2.** Schematic of surface preparation steps. (a) Piranha and electrochemical cleaning. (b) Immobilization of thiol-modified DNA. (c) Backfill with 6-mercaptohexanol to form a self-assembled monolayer (SAM). (d) Hybridization with methylene blue (MB)-labeled complimentary DNA.

### *4.1.3 Prior related work*

Microscale platforms such as the one presented here can ultimately enable a new approach for rapid screening of ligand binding properties of duplex DNA or other DNA structures, and thus facilitate the drug discovery process. Nucleic acid binders have

previously been identified via melting-curve analysis of nucleic acids in the presence/absence of ligands.[23-24, 145] When screening ligands as potential drug molecules, those that bind to and stabilize the duplex, causing shifts in melting temperature, $T_m$, can be considered "hits". If duplex DNA is the intended drug target, these "hits" indicate compounds that warrant further investigations including structure–activity relationship (SAR) studies. If duplex DNA is not the intended drug target, these "hits" could be used when screening a library of compounds with other known targets for potential genotoxicity.

The majority of studies that use melting-curve analysis have employed optical monitoring systems.[23, 146] A complementary approach, amenable to development of electronic array formats and hence high-throughput screening, is melting-curve monitoring via electrochemical detection of electrode-tethered DNA.

Temperature control is a critical variable for investigating kinetics and thermodynamics of biomolecular materials including DNA. Having a heat source that is compatible with microdevice architectures opens the opportunity of arrays with locally heated sites. Prior examples of coupling electrochemical detection with controlled temperature capability include: thermoelectric modules,[107, 147] heating wells of solutions[99, 148] and heated wire electrodes.[118, 149] The incorporation of copper resistive heaters on the backside of fiberglass epoxy sheets has been used for quantitative polymerase chain reaction (PCR) biosensors.[150] Fiche and coworkers used a heated flow cell to analyze the thermal stability of DNA with surface plasmon resonance (SPR),[66] and Buhot and coworkers continued the approach to work with Au

nanoparticles (AuNP) for SPR imaging.[68] Additional work was done by Bartlett and coworkers on denaturing DNA by electrostatic repulsion and monitoring the process through surface-enhanced Raman spectroscopy (SERS).[73-74] The Levicky group used disk electrodes to analyze the thermal stability of DNA–ligand complexes, and the sample volumes in such studies are governed by the size of the electrodes.[99] Additionally, the Plaxco and Soh groups created a microelectrochemical dynamic allele-specific hybridization device (MicroE-DASH).[102] The results of these studies and other prior work have shown that immobilization of DNA to the surface affects enthalpies and entropies of hybridization when compared to standard solution-phase methods.[61, 64, 99]

Previous studies by our group demonstrated the utility of microheater systems integrated with a three-electrode electrochemical cell to detect single- or multiple-base mismatches in immobilized duplex DNA,[22] and to study temperature-induced enhancement of signals due to temperature-dependent diffusion and thermal convection in model redox systems.[113] Our platform is unique in having an individual embedded platinum heater integrated with each planar three-electrode set, thus positioning our methodology for rapid profiling as well as easy scale-up to addressable arrays such as those for studying immobilized DNA under a variety of conditions. The microheater provides programmable, localized heat and also functions as a thin-film platinum resistance thermometer (PRT), probing resistance, and thus temperature, less than 1 μm from the electrodes. The platinum heater is insulated from the surface three-electrode system by a $SiO_2$ layer varying in thickness from 350 nm to 1 μm, depending

on device generation. To extend the temperature range for analysis below room temperature, the electrochemical platform can be contained in a refrigerated box, or an external thermoelectric (TE) module can be placed on the backside of the wafer for localized cooling. When the thermoelectric module is used as both a cooling and heating source, the embedded platinum heater is still employed as a PRT to monitor temperature. A polydimethylsiloxane (PDMS) sample microchamber mounted above the electrodes contains the analyte solution. This configuration enables rapid temperature ramping and independent current monitoring.

Herein, the use of our temperature-controlled electrochemical microplatform in two different assemblies is demonstrated, namely with a resistive heater, or with a thermoelectric module, to perform duplex DNA melting in the presence/absence of (1) proflavine, a well-known intercalator and one of the first published DNA binders,[151-152] and (2) diminazene aceturate (DMZ or Berenil), a minor groove binder.[153-154] Chemical structures of the examined binders are shown in **Figure 4.3**. For investigating DNA, a full-matched duplex was formed by an immobilized 5'-thiolated, single-stranded DNA (ssDNA) hybridized with a complementary sequence labeled with a redox-active MB on C7 of the 3' end. The results of our previous study, which involved investigating single-nucleotide polymorphism (SNP) in immobilized DNA,[22] motivated us to further explore whether changes in DNA melting temperature, $T_m$, in the presence of DNA ligand binders could also be assessed using our platform. While our proof-of-concept work was done with known duplex DNA binders, the method could be easily employed to test induced stability changes for a variety of other ligands.

It is worth noting that these selected ligands have also shown binding to other nucleotide structures such as c-di-GMP and G-quadruplexes.[154-156] The magnitude of changes in $T_m$ upon binding of these ligands was readily observable. In this chapter, additional specific enhancements to the performance of the microheater and the $SiO_2$ insulating layer for increased robustness as well as the incorporation of measurement automation routines to decrease measurement variability will be discussed.

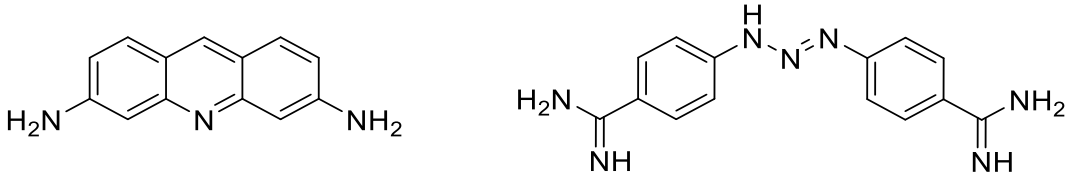


Proflavine Diminazene aceturate (DMZ)

**Figure 4.3.** Structures of ligands used in duplex DNA studies.[122]

## 4.2 Materials and methods

### *4.2.1 Materials*

The oligomers for the duplex DNA formed by ssDNA (5' HO-$(CH_2)_6$-S-S-$(CH_2)_6$-TTT ACC TTT ATT-3') and cDNA (3'-(MB)-AAA TGG AAA TAA CC-5') were synthesized by and purchased from Integrated DNA Technologies (Coralville, IA, USA) and Biosearch Technologies (Novato, CA, USA), respectively. Dimethyl sulfoxide (DMSO), diminazene aceturate (DMZ), 6-mercaptohexanol, proflavine hemisulfate salt hydrate, sodium phosphate dibasic, sodium phosphate monobasic, magnesium chloride heptahydrate, sodium chloride, and tris-(2-carboxyethyl) phosphine hydrochloride (TCEP) were purchased from Sigma-Aldrich (St. Louis, MO,

USA). All chemical reagents were of analytical grade or higher. Stock solutions of proflavine and DMZ were prepared at 14 mmol/L in DMSO and then diluted to 140 μmol/L in PBS buffer (10 mmol/L phosphate-buffered saline, pH 7.4) with 100 mmol/L NaCl. Deionized ultra-filtered (DIUF) water (18.2 MΩ·cm) was used in all preparations. Fused silica wafers were purchased from University Wafers (Boston, MA, USA).

### *4.2.2 Microfabrication of three-electrode device with embedded microheater*

Device fabrication methods were described in more detail in Chapter 2, but fabrication of specific devices used in the data collection of this chapter is summarized below. To increase the lifetime of the devices relative to devices that were previously reported,[22] fabrication steps were modified to increase both the quality of the platinum heater and the electrical and defect properties of the silicon oxide insulator. The new fabrication design uses an ion beam sputtering cluster tool (4Wave Inc., Sterling, VA, USA) with two process modules, biased target deposition and ion beam deposition, both including an etch gun for in situ precleaning. The wafers were etched for 60 s (at 20.6 nm/min) to expose fresh $SiO_2$ and coated with a Ti adhesion layer (5 nm at 0.86 nm/min). Then, a Pt layer was deposited (220 nm, 2.35 nm/min) and capped with an additional Ti adhesion layer (5 nm at 0.86 nm/min). The wafer was transferred to the other process module, and either a $SiO_2$, for the resistive heated wafer (50 nm, 2.31 nm/min), or an $Al_2O_3$ seed layer, for the thermoelectric heated wafer (50 nm, 5.24 nm/min), was deposited in another ion beam deposition process module without breaking vacuum.

Afterwards, lithography was used to pattern the heater mask for ion beam milling (4Wave Ion Mill, 4Wave Inc.), thereby creating the etched heater. The photoresist was removed using Microposit Remover 1165 (Dow Chemical Company, Marlborough, MA, USA) and rinsed with acetone, isopropyl alcohol, and then DIUF water. The clean wafers were etched for 7 to 9 min at low power in the ion mill to round the edges of the heater traces. For the wafer used for the thermoelectric heating, the $SiO_2$ layer was deposited (75 nm, 0.15 nm/cycle, 500 cycles) with remote plasma atomic layer deposition (ALD) (Oxford FlexAL atomic layer deposition, Bristol, UK), then a second layer (200 nm, 112.3 nm/min) was deposited with plasma-enhanced chemical vapor deposition (Plasma-Therm Versaline High Density Plasma Chemical Vapor Deposition (PECVD), Saint Petersburg, FL, USA), and lastly it was capped with an additional ALD $SiO_2$ layer (75 nm, 0.15 nm/cycle, 500 cycles). For the wafer used with the embedded heater, 1 μm of PECVD oxide was deposited on top of the etched heater traces. The wafer was then annealed in a nitrogen furnace at 800 °C for 1 h (Sandvik MRL Diffusion Furnace, Sandviken, Sweden). The top electrodes were patterned with lithography, and an e-beam evaporator (Denton Infinity 22 E-Beam, Morristown, NJ, USA) was used to deposit a Ti adhesion layer (20 nm, 6.0 nm/min), and then the Pt reference and counter electrodes (200 nm, 6 nm/min). The process was repeated for the gold working electrode (200 nm, 6.0 nm/min), which has an exposed area of approximately 0.003 $cm^2$. Once the fabrication was complete, the contact pads were patterned with lithography, and the $SiO_2$ was etched with a reactive ion etcher (Plasma-Therm/Unaxis 790 RIE, Saint Petersburg, FL, USA).

### *4.2.3 Platform assembly: resistive heating*

The resistive heating experiments used devices completed with 1 μm PECVD $SiO_2$ and were assembled as described in Section 3.4 The experimental procedure utilized the voltage control program explained in Section 3.6.1. In summary, the devices were placed in an ice box and a voltage of 0.5 V was used to monitor the temperature during the equilibration time and then the voltage was increased by 0.4 V every 25 s from 1.0 V to 11.4 V to produce the stepped temperature ramp for the melting experiments.

### *4.2.4 Platform assembly: thermoelectric heating*

Devices fabricated with 350 nm $SiO_2$ were used for the thermoelectric heating studies with the Pt thin-film used as the PRT for temperature monitoring and the assembly was detailed in Section 3.6.2. In summary, thermoelectric module (Peltier MS2,010,06,06,11,11,00,W2, Laird Technologies Inc., Chesterfield, MO). As described in Section 3.6.1, to reach 10 °C, 0.2 V was applied for 20 min, and then for the heating cycle, the voltage was stepped by 0.25 V every 25 s from 0.2 V to −0.4 V. The temperature was monitored at 0.5 V while the sample was cooled and then heated, and this monitoring was terminated before each measurement of the electrochemistry program, to minimize any leakage current.

### *4.2.5 Electrode cleaning and preparation of duplex self-assembly on Au electrodes*

The Au working electrode was first cleaned with a drop of piranha solution (3:1 volume mixture of concentrated $H_2SO_4$ and 30% (w/w) $H_2O_2$ in $H_2O$) for 2 min (Caution! Piranha solutions can be explosive if they contact organic materials), rinsed with DIUF

water, and then electrochemically cleaned with 20 µL of 0.5 mol/L $H_2SO_4$. The potential was swept from 0 V to 0.9 V (vs. the platinum reference electrode) at a scan rate of 0.1 V/s for a total of twenty cycles. To reduce disulfide bonds in the ssDNA, 1 µL of 200 µmol/L ssDNA was mixed with 2 µL of 20 mmol/L TCEP in DIUF water at room temperature in the dark for 90 min. The solution was then diluted to a DNA concentration of 2 µmol/L with 100 µL PBS buffer (10 mmol/L phosphate-buffered saline, pH 7.4) with 1 mol/L NaCl and 1 mmol/L $MgCl_2$. After cleaning, the Au electrode was incubated with 10 µL of 2 µmol/L ssDNA for 90 min in a dark, high-humidity chamber. The electrodes were thoroughly rinsed with DIUF water and dried with nitrogen. To form a self-assembled monolayer (SAM) and minimize nonspecific adsorption to the Au surface, the electrodes were incubated with 10 µL of 2 mmol/L 6-mercaptohexanol solution in PBS with 1 mol/L NaCl and 1 mmol/L $MgCl_2$ for 1 h at room temperature, in a dark, high-humidity chamber. The electrodes were rinsed for 1 min using DIUF water to remove any remaining 6-mercaptohexanol solution, and again dried with nitrogen. To study the hybridization interactions, the PDMS chamber with a 2.5 mm diameter hole was filled with 10 µL of 2 µmol/L cDNA in PBS buffer containing 100 mmol/L NaCl; this sample was left to stand for 15 min at room temperature, and then cooled to 10 °C. The melting profile was performed as described in Sections 4.2.3 and 4.2.4, and then samples were allowed to cool to room temperature over 15 min. When examining ligand stabilization, 1 µL of 140 µmol/L ligand stock solution was added to the PDMS well after the ~ 15 min at room temperature. The sample was then cooled to 10 °C for 20 min and the melting profile was analyzed again.

After completion, the PDMS well was removed and the device was rinsed in DIUF water. Due to the possibility of microelectronic component degradation in buffer, the devices were stored dry and prepared fresh for each set of experiments.

### *4.2.6 Melting-curve analysis*

For duplex DNA melting-curve analysis, all electrochemical measurements were performed with an electrochemical workstation (CHI1040c, CH Instruments Inc., Austin, TX, USA). Sample temperature was controlled and monitored (as discussed above for the two different set-ups in Sections 4.2.3 and 4.2.4) using the embedded platinum thin film as a PRT in both cases.

The temperature was increased incrementally with selected voltage steps under computer control, 15 s were allowed to equilibrate the sample, and then 10 s were allowed to acquire the square wave voltammetry (SWV) scan for that temperature. The thermal profile of the temperature measurements is shown in **Figure 3.5**. SWV was carried out in all studies from −0.75 V to −0.35 V, or −0.70 to −0.30 V, with a 0.001 V interval, 60 Hz frequency and 0.025 V amplitude. Baseline correction was performed by fitting a straight line to the two lowest points on either side of the MB peak and then subtracting the baseline from the peak current to measure the peak height. All data were plotted in Origin (OriginPro 2016, OriginLab Corp., Northampton, MA, USA) and a Boltzmann function was fit to the data to find the $T_m$. In cases where the current had an initial increase at low temperature, at least one data point before the maximum was

included in the Boltzmann function to find the $T_m$. These values were also confirmed by taking the derivative of the thermal profile.

## 4.3 Results and discussion

Because MB has a known reversible oxidation-reduction potential,[17] the current produced by the MB at the working electrode can be monitored as a function of temperature. When the maximum amount of the complementary sequence is bound, the high relative concentration of MB proximal to the surface (**Figure 4.4**) leads to high electron transfer (eT), and therefore produces the highest current. As the temperature increases incrementally, the equilibrium of bound and unbound complementary DNA shifts as less of the MB-labeled complementary sequence is hybridized, meaning the concentration of MB close to the surface decreases, causing the current measured to decrease. A melting curve was constructed by plotting the peak currents of MB at each temperature step vs. temperature, with the inflection point determining the melting point, $T_m$. An increase in stability, such as that caused by ligands bound to the DNA probe, requires more energy to denature the duplex, causing an increase of $T_m$ and thus a positive change, $\Delta T_m$. In addition, the more a ligand stabilizes the structure, the greater is the $\Delta T_m$.

To maximize the measurement repeatability for quantifying the effect introduced by a given ligand under specific conditions, a sequential melting protocol was used, illustrated schematically in **Figure 4.4**. Because of interest in the shift, or $\Delta T_m$, a baseline measurement of the duplex DNA melting, $T_{m,\,baseline}$, was taken before adding

the ligand. After allowing the duplex to rehybridize, the sample was melted again either in the absence or in the presence of the ligand of interest. With this protocol, the $\Delta T_m$ of no ligand added, $\Delta T_{m,\ DNA}$, could be compared to confirm that the hybridization is reversible. Incubation with two molecules known to bind to duplex DNA, proflavine and DMZ, were examined to determine whether the change in stability caused by ligand binding, $\Delta T_{m,\ ligand}$ could be quantified.

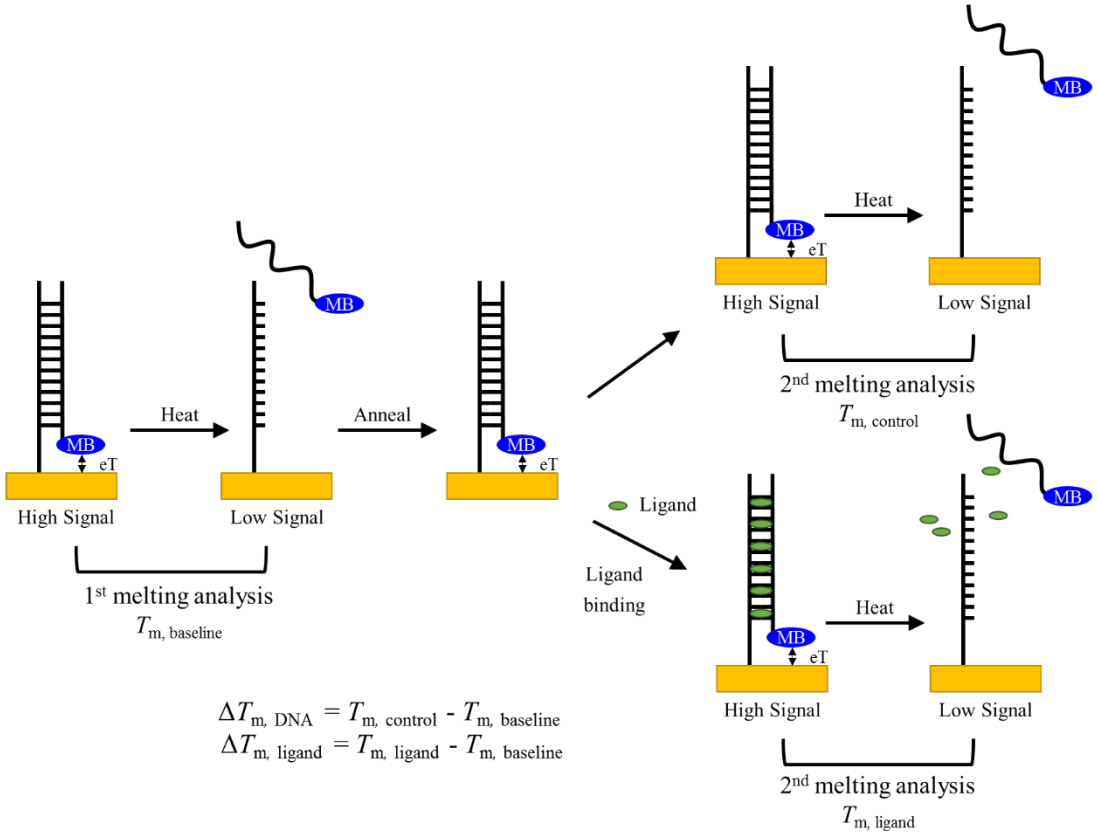


**Figure 4.4.** Melting analysis protocol for duplex DNA to probe for ligand-induced stabilization and to minimize measurement variability.[122]

Experiments to obtain melting curves for different samples were performed with two different methods for cooling and heating: (1) using an insulated container for cooling and the embedded platinum thin film for resistive heating (**Figure 4.5**); and (2)

using a thermoelectric (Peltier) module to cool and heat the device while monitoring the temperature with the PRT (**Figure 4.6**). Each of these methods has its own advantages. For example, a resistive heating device is relatively inexpensive compared to a Peltier module for temperature control, and it offers a straightforward approach to run many devices in parallel with different thermal profiles.

The results shown in **Figure 4.5** for the first method using resistive heating indicate that our microscale platform could perform melting-curve analyses on duplex structures, as well as ligand-based stabilization. Stabilization effects (higher $\Delta T_m$) were observed for proflavine, which intercalates between the base pairs,[151-152] and DMZ, which binds to the minor groove of duplex DNA.[153-154] An example of a SWV acquired during the melting of the duplex DNA is shown in **Figure 4.5a**. A five-point moving average was performed to smooth the electronic noise. Although a platinum pseudo-reference was used, the potential of MB was highly consistent, and the potential did not drift significantly over several experiments.

To start an experiment below room temperature (20 °C) using resistive heating, an icepack was placed in a polystyrene foam cooler and the entire device platform was positioned inside. Although the same icepack and insulating box were used, small day-to-day variations in the temperature and thus the thermal load on the microheater could occur. The resulting heating profile can vary slightly to produce slightly increased standard deviations (**Table 4.1**). In addition, over time there can be some loss of integrity of the device's insulating oxide layer, which leads to the observation of leakage current (noise) in the SWV that can become problematic in typically less than

10–12 melting profile analyses. The resistive heating data collected over three devices produced similar results.

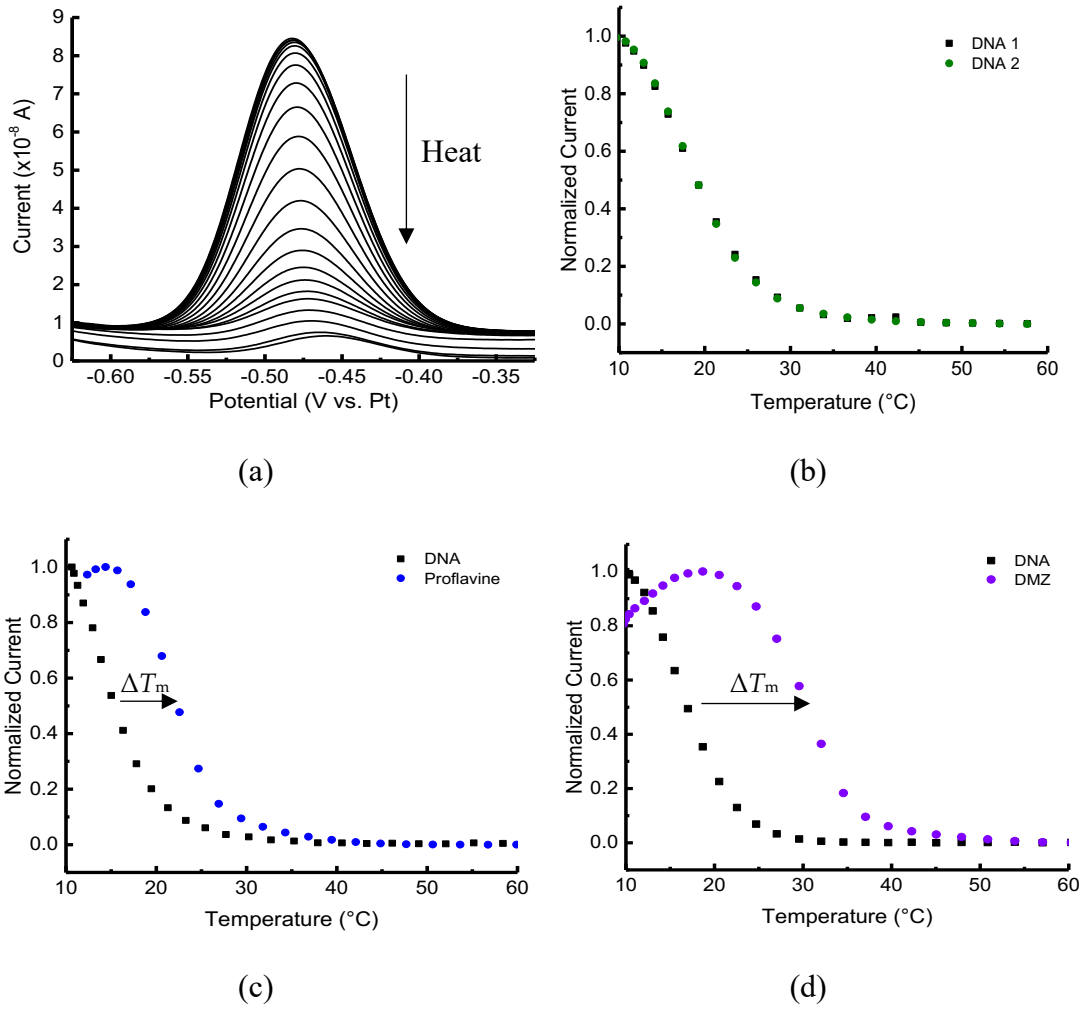


**Figure 4.5.** Melting-curve analysis of duplex DNA in the presence/absence of binding ligands performed with an embedded heater. (a) Square wave voltammograms of 2 µmol/L MB-labeled cDNA in 10 mmol/L PBS with 100 mmol/L NaCl, pH 7.4. Melting curves (normalized) of duplex in the absence (b) and presence of 13 µmol/L ligands: proflavine (c), and diminazene aceturate (DMZ) (d). (b–d) The first baseline curve is shown in black, and the second melting analysis with or without ligand is shown in its respective color.[122]

Data collection was also investigated with the second method of cooling/heating using a thermoelectric module. Though inherently less integrated, this

approach offers the convenience of being able to vary the current direction of the thermoelectric to both cool and heat the samples when placed on the backside of the electrochemical platform, removing the need for an ice box. The PRT can still be used (even with devices having a degraded insulating layer due to chemical and thermal stress from multiple experimental cycles) to record the temperature in thermoelectric-driven experiments as long as the monitoring voltage is not applied in the periods while the electrochemistry is monitored. This extends the lifetime of the devices (typically over 30 thermal profiles), while the PRT still provides proximal temperature measurements. **Figure 4.6** shows the data collected with cooling and heating via a thermoelectric module and monitoring the temperature with the PRT.

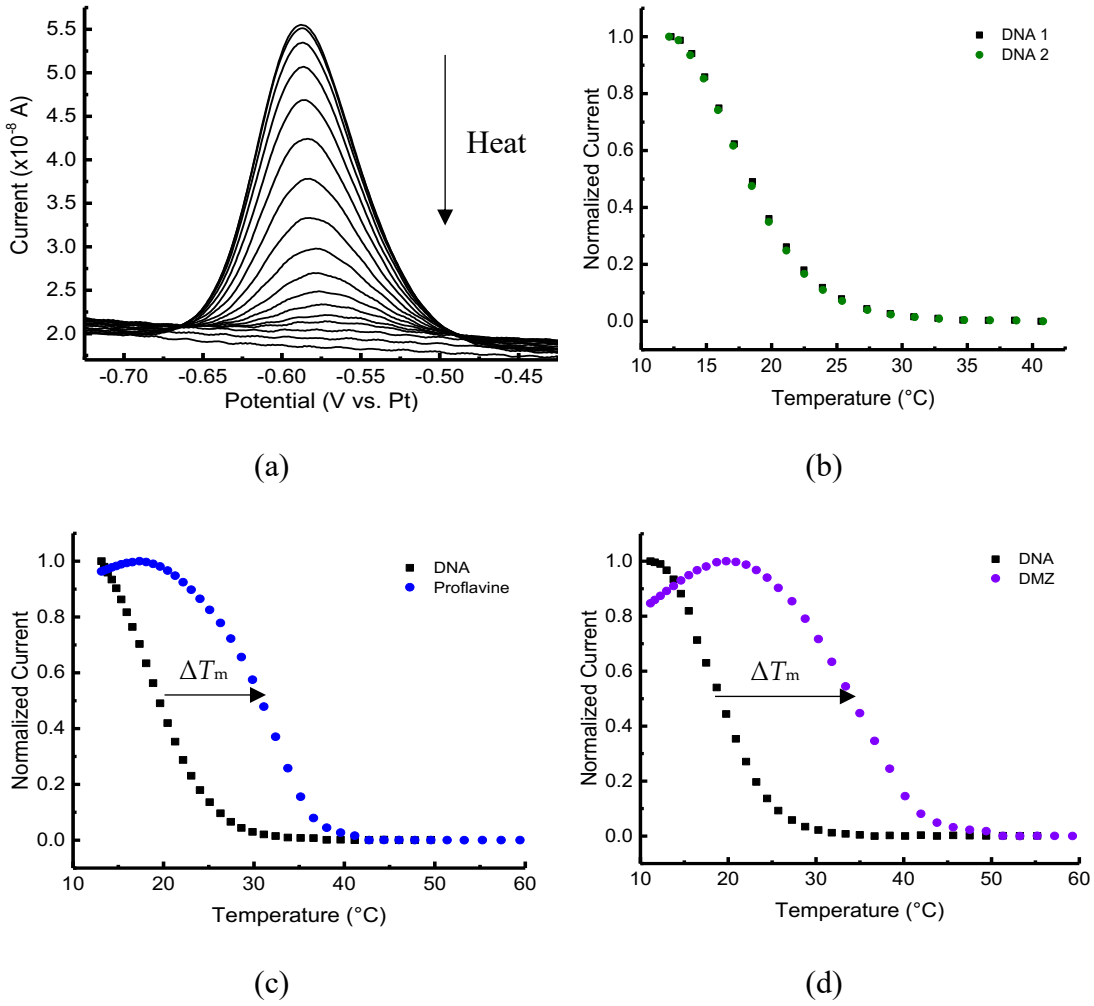


**Figure 4.6.** Melting-curve analysis of duplex DNA in the presence/absence of binding ligands performed with a thermoelectric module. (a) Square wave voltammograms of 2 μmol/L MB-labeled cDNA in 10 mmol/L PBS with 100 mmol/L NaCl, pH 7.4. Melting curves (normalized) of duplex in the absence (b) and presence of 13 μmol/L ligands: proflavine (c), and diminazene aceturate (DMZ) (d). (b–d) The first baseline curve is shown in black, and the second melting analysis with or without ligand is shown in its respective color.[122]

Since $\Delta T_{m,\,DNA}$ was approximately zero, $-0.3 \pm 0.4$ °C (all uncertainties reported as the standard deviation of at least three replicates unless otherwise noted), the duplex DNA melting profile is highly reversible, and the successive measurements do not affect the thermal stability of the duplex. This can be clearly seen in the two sequential

melting profiles in **Figure 4.5** and **Figure 4.6**. This sequential procedure may not be appropriate for more complicated biomolecular systems, but it was used in this foundational study to more thoroughly probe the capabilities of the platform and decrease measurement variability. As expected, the $T_m$ values measured for immobilized DNA are lower than the corresponding solution-phase measurements.[61, 64, 99] Using the OligoAnalyzer software (www.idtdna.com/calc/analyzer), it was determined that the solution-phase $T_m$ for 2 μmol/L DNA with 100 mmol/L NaCl was approximately 32 °C. Concerns with doing sequential melts involve uncertainty of the stability of the 6-mercaptohexanol SAM, and whether any desorption of DNA from the surface occurs.[99] With our platform and microfabricated electrodes, however, no changes in the baseline response were observed after melting the DNA duplexes at least three times with temperature excursions up to 60 °C. Additionally, a control experiment was done with preparing the device without the thiol modified DNA and incubating a SAM with 2 μmol/L cDNA and in the preliminary experiment current increases were only seen above 75 °C (**Figure S4.1**).

The shift in the melting temperatures caused by the two different ligands are seen in **Figure 4.5c,d** and **Figure 4.6c,d**. The stabilization shifts (all positive) are summarized for sets of triplicate measurements (unless otherwise noted) in **Table 4.1**. The initial melting profile of the duplex DNA is shown in black with each set of curves in **Figure 4.5** and **Figure 4.6**. Ligand-induced curves were produced after allowing the sample to cool for 15 min and then adding 1 μL of 140 μmol/L ligand in PBS to the PDMS chamber. The sample containing the ligand was allowed an additional 20 min

to equilibrate at 10 °C before starting the second melting analysis. Note that these experiments were done on several different devices (**Figure S4.2**), as well as on different days.

**Table 4.1.** Summary of duplex thermal profiles.[122]

| | Thermoelectric Cooling/Heating | | | Refrigerated w/ Resistive Heating | | |
|---|---|---|---|---|---|---|
| | No ligand | Proflavine | DMZ | No Ligand | Proflavine | DMZ |
| $T_{m,\ baseline}$ (°C) | 17.0 ± 1.0 | 18.5 ± 0.1 | 16.8 ± 1.0 | 18.1 ± 1.8 | 11.8 ± 1.2 [1] | 15.8 ± 0.8 |
| $T_{m,\ control}$ (°C) | 17.0 ± 1.0 | - | - | 18.1 ± 2.2 | - | - |
| $T_{m,\ ligand}$ (°C) | - | 30.3 ± 0.4 | 31.5 ± 2.0 | - | 21.9 ± 0.2 [1] | 28.1 ± 1.6 |
| **$\Delta T_m$ (°C)** | **−0.3 ± 0.4** | **11.8 ± 0.3** | **14.6 ± 0.6** | **0.0 ± 1.1** | **10.1 ± 1.0** [1] | **12.3 ± 1.7** |

Standard deviations given for three replicates except for [1] ($N = 2$).

The results indicate that the electrochemical microplatform can detect and quantify the $T_m$ shift of the duplex DNA arising due to the binding of ligands. Both distinct heating/cooling methods employed showed the expected positive $\Delta T_m$ in the presence of the two ligands. Additionally, the difference in magnitude of $\Delta T_{m,\ DMZ}$ and $\Delta T_{m,\ proflavine}$ was approximately 2.5 °C for both methods, which shows self-consistency between the two different set ups. In both experimental methods, the difference in $\Delta T_m$ was large enough to discriminate the binding affinities of the ligands, and showed proflavine, a well-known intercalator, had the smaller magnitude shift compared to DMZ, a minor groove binder.

The automation of the experimental program used in these reported studies has greatly improved measurement repeatability over manually running each SWV and

then increasing the voltage to the heater. The limitation of the current automation program is that it supplies a fixed voltage, and as a result, the power applied to heat the well is proportional to $1/R^2$. Therefore, when applying a fixed voltage ramp to devices that may have a slight difference in the resistance, the power input and the resulting temperature ramp can show small changes between devices. To reduce this factor, a proportional-integral-derivative (PID) controller can be included in the automation so that a fixed resistance or temperature set-point could be reached at each interval.

The motivation of this study was to develop platform capabilities and investigate performance levels as steps toward realizing an automated system for which an array of these microplatforms could be used to simultaneously probe a variety of conditions that alter biomolecular characteristics. Fabrication of a reliable array platform would enable investigations of mechanistic effects and binding kinetics in a highly efficient manner.

## 4.4 Conclusions

In summary, a temperature-controlled electrochemical microplatform, with the ability to perform rapid melting-curve analyses on duplex DNA in the presence/absence of the binding ligands, was demonstrated. By acquiring the peak current values at different temperature values, melting-curves were constructed to determine the $T_m$ of different DNA analytes. The obtained $\Delta T_m$ values that develop in the presence of the binding ligands show the stabilizing effect these compounds can have on duplex DNA. The measurement of these shifts was demonstrated with two different cooling/heating

approaches with good reproducibility, observed over several days and with different devices. It is expected that this microscale platform may have more general utility for determining temperature-dependent stability in other types of biomolecular interaction studies. The fabrication methods used for this microscale device can be extended to produce systems of arrays with incorporated microfluidics, for high-throughput, parallel measurements of binding ligands and other biomolecular system screening, on small-volume samples.

## 4.5 Supplemental

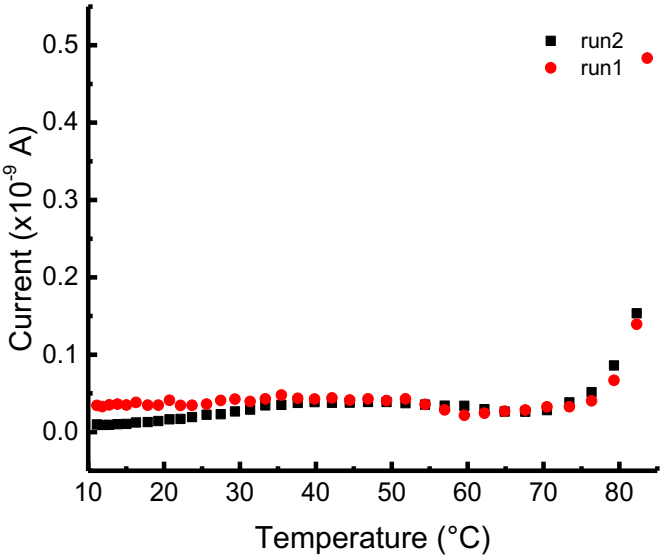


**Figure S4.1**. Control melting curves with SAM prepared without tethered DNA in 2 μmol/L cDNA in solution.

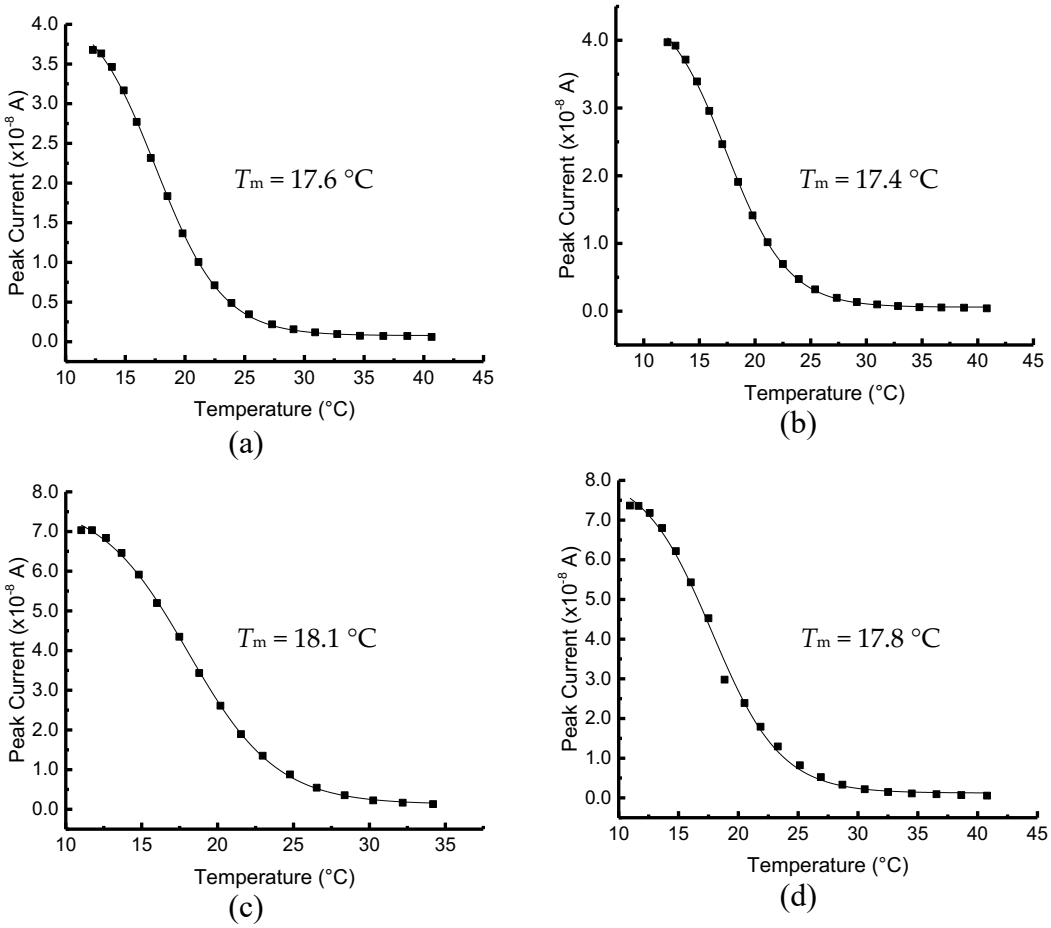


**Figure S4.2.** Duplex melting curves on two different devices on the same day. (a) and (b) show results for Wafer 8, Device 17, trials 1 and 2; (c) and (d) show results for Wafer 8, Device 14, trials 1 and 2. All data were plotted in OriginPro 2016 and a Boltzmann function was used fit to the data to find $T_m$.[122]

# Chapter 5 Measuring Thermal Profiles of Immobilized G-Quadruplexes

## 5.1 Introduction to G-quadruplexes

Selectively targeting genetic information is a key area in drug discovery. Telomeres are regions at the end of chromosomes that contain repeats of sequences such at $(TTAGGG)_n$ and that have been shown to form G-quadruplexes *in vivo*.[157] Small molecules have been shown to bind to G-quadruplexes and affect transcription.[158] These guanine-rich sequences form tetrads with Hoogsteen base pairing, known as G-tetrads or G-quartets (**Figure 5.1a**), and those tetrads are π-stacked to form the secondary structures shown in **Figure 5.1b-h**.[159] Based on the number of strands involved, sequence, loop-length, stabilizing cations, and conditions, the secondary structure can vary greatly.[160] The structure of the G-quadruplex is classified by the relative orientation of the strands (parallel or antiparallel) and the syn and anti glycosidic conformations.[159] **Figure 5.1b** shows the structure of a four-stranded G-quadruplex where all strands are in parallel orientation.[161] The same core can be formed with two strands with loops connecting neighboring strands (**Figure 5.1c**).[162-163] When two of the core strands are oriented in an opposite directions, the structure is called antiparallel, and an example dimeric antiparallel structure is shown in **Figure 5.1d**.[162] Monovalent cations coordinate to the carbonyl groups and affect the preferred conformation; potassium-stabilized telomeric sequences have been shown to form the parallel structure (**Figure 5.1e**)[163] and sodium-stabilized telomeric sequences have

been shown to form the antiparallel basket structure (**Figure 5.1f**).[164] When three strands are oriented in one direction while the fourth strand is antiparallel, the structures are termed (3+1) or hybrid structures and a wide range of such hybrid structures have been discovered (two examples are shown in **Figures 5.1g** and **h**).[159]

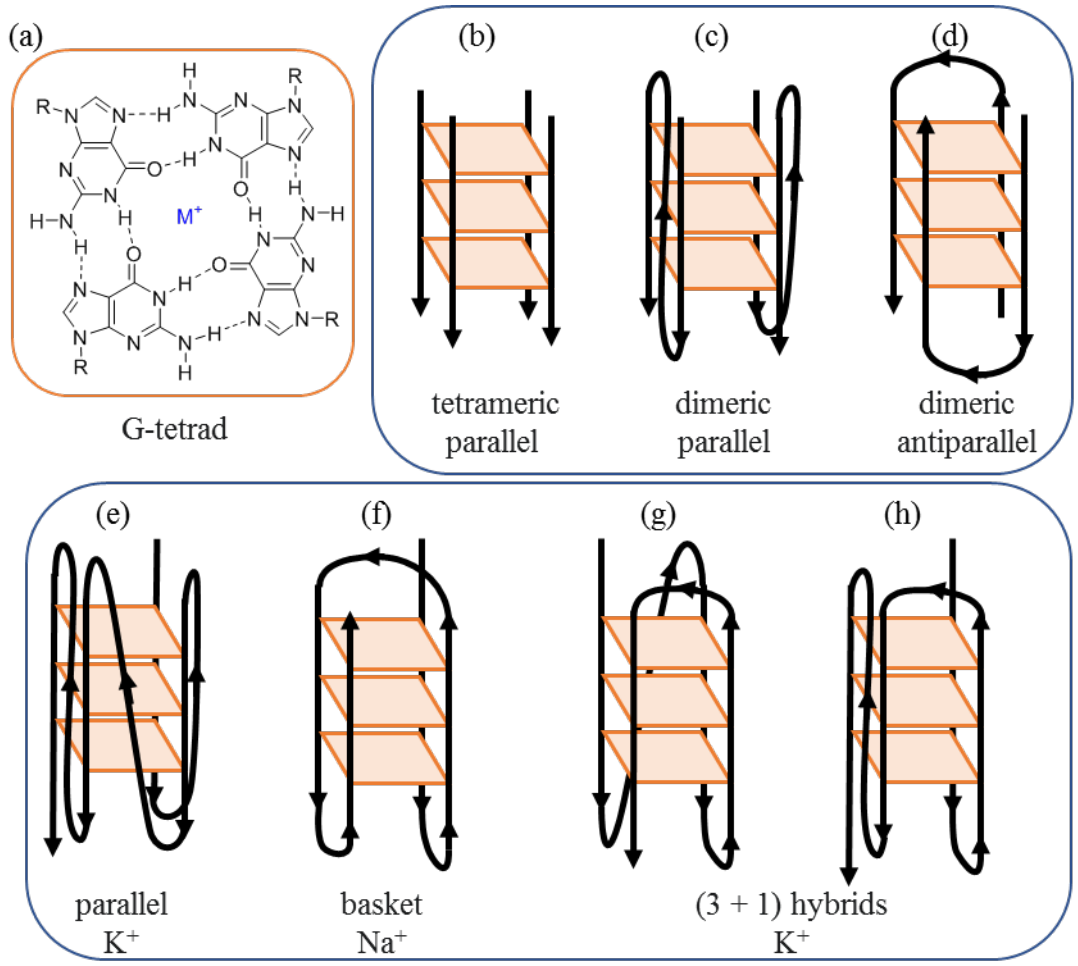


**Figure 5.1**. (a) G-tetrad composed of 4 guanines represented as orange rectangles. (b-d) Intermolecular telomeric G-quadruplex structures. (e-h) Intramolecular telomeric G-quadruplex structures stabilized with potassium and sodium. [Adapted from reference [159].]

G-quadruplexes were also discovered in promotor regions of genes and small molecules that can selectively bind to those G-quadruplexes can then also selectively

inhibit the transcription of the corresponding gene.[165] Quarfloxin was a G-quadruplex binding molecule that reached Phase II clinical trials, but was terminated in March 2010 due to issues with bioavailability.[131] CX-5461 is currently in Phase I for clinical trials for patients with BRCA1/2 deficient tumors.[166] The interest in finding new G-quadruplex binding ligands for new drug discovery has increased and has recently been reviewed.[167]

Finding ligands that are highly selective and have high binding affinities is critical to further progress in this area of cancer research. Current research has been focused on detecting ligand-induced stabilization via fluorescent ligand displacement[168] or Fluorescence Resonance Energy Transfer (FRET) melting.[165, 169]

Cian and coworkers used FRET melting to detect ligand stabilization and selectivity towards the human telomeric G-quadruplex.[40] The researchers highlight the limitations of the technique including cases where the ligand molecule of interest is highly fluorescent, especially in the region of the "donor" fluorescence, or if the molecule interacts with the fluorescein or TAMRA (donor or acceptor molecules) instead of binding to the G-quadruplex.[40]

Although calorimetry represents the gold standard for measuring the unfolding of secondary structures, currently it has not been configured for HTS. Electrochemistry methods using a redox probe can have much higher sensitivity and can use significantly lower sample volumes and concentrations. In addition, it is rare to have any interference or background noise that would affect the detection of the redox probe.

Plaxco's group has tethered the G-quadruplex-forming thrombin aptamer on the surface for electrochemical sensing aimed at protein detection.[170] Further work has shown that the largest signal changes occur upon binding when the aptamer is initially completely unfolded due to instability at lower ionic strength buffers prior to binding.[171] One point to note that is although researchers have included proper controls to make sure the signal changes upon binding of thrombin to the thrombin aptamer, conclusions are being formed about the structural changes on the surface from established solution-phase structural analyses and the observed current changes.

Palacký and coworkers have characterized human telomeric G-quadruplex with Raman spectroscopy in solution.[172] Although the method provides considerable conformation information, researchers required DNA concentrations of 8 to 240 mmol/L.[172] Surface-enhanced Raman scattering (SERS) provides signals based on the vibrations specific to certain conformations and thus can be used to help understand the structure of G-quadruplexes on the surface. Cao and coworkers developed a visible, near-infrared metamaterial split-ring resonator, and characterized a G-quadruplex forming sequence, AS1411.[173] Researchers were able to monitor a sharp peak at 1482 $cm^{-1}$ which is associated with Hoogsteen hydrogen bonding.[173] Qiu and coworkers used nanoporous gold disks to sense the binding of malachite green to a G-quadruplex forming sequence, $d[T_9(GGT)_7GG]$.[174] In their sensor, they do not have measurable signal from the G-quadruplex, but can detect the binding of the malachite green.[174] Both previously reported examples for SERS of G-quadruplex[173-174] were analyzed dry, which can affect the structure. Although not tethered to a gold surface, telomeric G-

quadruplex, $(TTAGGG)_4$ has been studied in $Na^+$ and $K^+$ with citrate- and chloride-covered Ag nanoparticles.[175] Li and coworkers were also able to detect Raman shifts of nine G-quadruplex forming sequences in solution by aggregating with $Al^{3+}$ and Ag nanoparticles.[176]

To the best of our knowledge the structure of G-quadruplex tethered to a surface has not been studied as a function of temperature. The goal in our proposed study was to employ an off-on approach (**Figure 5.2**) to analyze the telomeric G-quadruplex sequence, $(TTAGGG)_4$ with low current measured when the G-quadruplex was formed at the Au electrode surface. As the temperature increased, the G-quadruplex would be expected to unfold. It has been previously reported that an unfolded structure is more flexible and thus can produce higher current.[177] Using this premise, thermal profiles could be measured and investigated for stabilization effects introduced through ligand binding or changing chemical conditions. Additional related experiments were also performed on a DNA sequence of the same number of base pairs as the G-quadruplex sequence studied, but all thymine bases, to have an approximation of the thermal profile of a DNA sequence with minimal secondary structure.

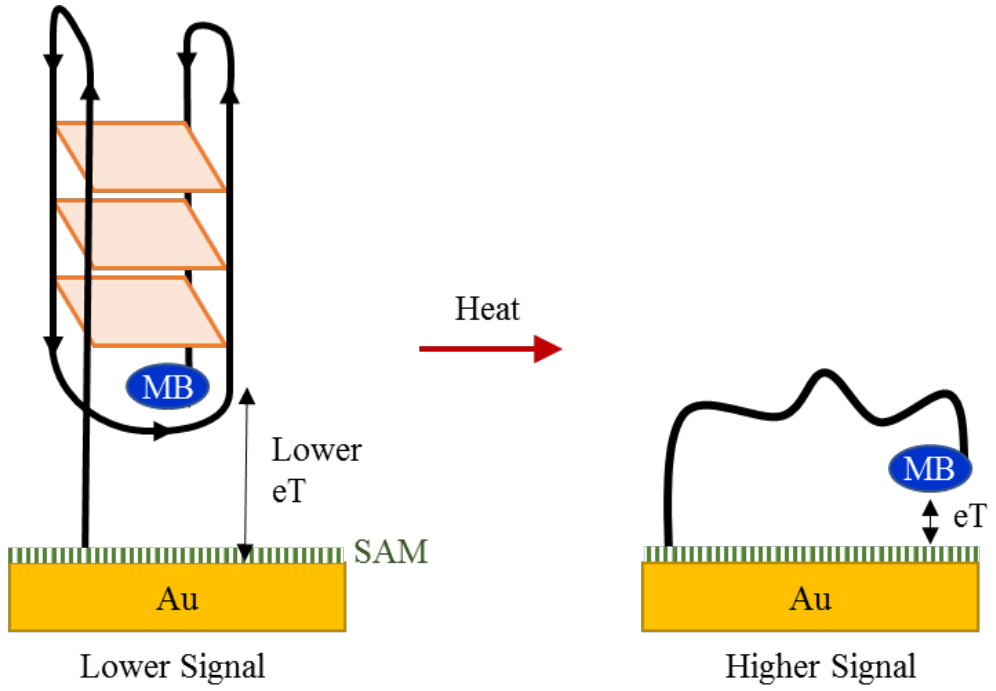


**Figure 5.2**. Proposed thermal response of telomeric G-quadruplex, HS-(TTAGGG)$_4$-MB.

This concept becomes less clear when there is not a direct on-off pathway, as with simpler duplex system, and the unfolding pathway is more complicated. Steps to measure the thermal profile of a telomeric G-quadruplex and factors that affect the resulting thermal profile will be discussed in this chapter. Ligands used in studies of how the stability of the G-quadruplexes might be altered are shown in **Figure 5.3**. SYUIQ-5 has been shown to bind to telomeric G-quadruplexes and inhibit telomerase activity,[178] and diminazene aceturate (DMZ) has been shown to bind to a range of G-quadruplex forming sequences.[154-155, 179]

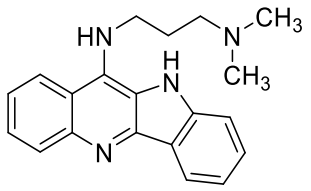


SYUIQ-5

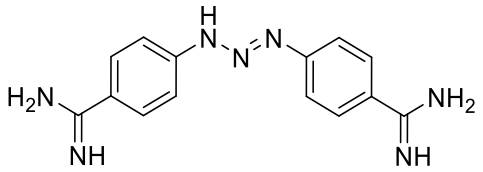


Diminazene aceturate (DMZ)

**Figure 5.3.** Structures of ligands used in G-quadruplex stability studies.

## 5.2 Materials and experimental methods

### *5.2.1 Materials*

The oligomer for the G-quadruplex DNA (5' HO-$(CH_2)_6$-S-S-$(CH_2)_6$-d$(TTAGGG)_4$-MB 3') was synthesized by and purchased from both Biosearch Technologies (Novato, CA, USA) and Integrated DNA Technologies (Coralville, IA, USA). The oligomer for the d$(T)_{24}$ DNA (5' HO-$(CH_2)_6$-S-S-$(CH_2)_6$-d$(T)_{24}$-MB 3') used to related investigations was synthesized by and purchased from Integrated DNA Technologies (Coralville, IA, USA). All sequences were ordered with dual HPLC purification. G4 DNA Batch 1 and 2 stock solutions were diluted to 200 µmol/L in DIUF. Due to supply issues, G4 DNA Batch 3 was purchased from Integrated DNA Technologies (Coralville, IA, USA). The available coupling of MB from IDT also had a one-shorter carbon linker. The IDT oligomers, Batch 3 and d$(T)_{24}$, were reconstituted to 100 µmol/L in TE buffer (10 mmol/L Tris with 1 mmol/L EDTA buffered to pH 8.0 with HCl). Upon reconstituting, G4 Batch 3 was heated to 90 ºC for 10 min and cooled to room temperature at 1 ºC/ min; all aliquots were stored at -20 ºC.

Dimethyl sulfoxide (DMSO), diminazene aceturate (DMZ), ethylenediaminetetraacetic acid (EDTA), magnesium chloride heptahydrate, 6-mercaptohexanol (6-MCH), sodium phosphate dibasic, sodium phosphate monobasic, sodium chloride, SYUIQ-5, tris-(2-carboxyethyl) phosphine hydrochloride (TCEP), and Trizma base were purchased from Sigma-Aldrich (St. Louis, MO, USA). All chemical reagents were of analytical grade or higher.

Buffers were prepared for the relative concentration of $Na^+$: PBS100 (5 mmol/L sodium phosphate monobasic, 5 mmol/L sodium phosphate dibasic, 85 mmol/L NaCl, and buffered to pH 7.4 with NaOH), PBS250 buffer (5 mmol/L sodium phosphate monobasic, 5 mmol/L sodium phosphate dibasic, 235 mmol/L NaCl, and buffered to pH 7.4 with NaOH), PBS1000 (5 mmol/L sodium phosphate monobasic, 5 mmol/L sodium phosphate dibasic, 985 mmol/L NaCl, and buffered to pH 7.4 with NaOH), and also PBS1001 (5 mmol/L sodium phosphate monobasic, 5 mmol/L sodium phosphate dibasic, 985 mmol/L NaCl, 1 mmol/L $MgCl_2$ and buffered to pH 7.4 with NaOH). Deionized ultra-filtered (DIUF) water (18.2 MΩ·cm) was used in all preparations.

DMZ stock solution was prepared at 8.4 mmol/L in DMSO and diluted to 10 µmol/L or 1 µmol/L in PBS250. The extinction coefficient of 36,7000 $(mol/L)^{-1}$ $cm^{-1}$ was used to verify the DMZ stock solution concentration. Stock solutions of SYUIQ-5 were prepared at 10 mmol/L in DMSO and then diluted to 100 µmol/L in PBS250.

### *5.2.2 Platform assembly*

Device assembly was performed as described in Sections 3.5. In short, devices fabricated with 1 µm of annealed PECVD oxide (**Figure 2.14**, **right**) were used and mounted on a PCB with a hole allowing for the placement of a Peltier module on the backside of the wafer. Once assembled with a heat sink compound at the interface between the back of the wafer and the top of the thermoelectric, the device was connected to both the source and SMU. The source controlled the voltage to the heater regulated by the ECP Versions 1 and 2 (Sections 3.6.1.2 and 3.6.2), and for the enabled PID loop as described in Section 3.6.3. In both cases the SMU monitored the current through the PRT at 0.5 V when the electrochemistry was not running, and thereby monitoring the temperature of the device. The temperature recorded for each SWV was the last measurement before the voltage was terminated before the SWV was started.

### *5.2.3 Electrode cleaning and preparation of self-assembly on Au electrode*

Similar to the description in Section 4.2.5, the devices were cleaned with 2 min of piranha solution (3:1 volume mixture of concentrated $H_2SO_4$ and 30% (w/w) $H_2O_2$ in $H_2O$: Caution! Piranha solutions can be explosive if they contact organic materials), rinsed with DIUF and dried with nitrogen. An electrochemical cleaning procedure was done with 20 µL of 0.5 mol/L $H_2SO_4$. The potential was swept from 0.9 V to 0 V (vs. the platinum pseudoreference electrode) for 20 cycles at a scan rate of 0.1 V/s.

To reduce disulfide bonds and cleave the protecting thiol group, 1 µL of the respective stock solution was mixed with 2 µL of 10 to 20 mmol/L TCEP in DIUF

water at room temperature in the dark for 60 to 90 min. The solution was then diluted to a DNA concentration of 2 μmol/L with 100 μL with either PBS250 or PBS1000.

After cleaning, unless otherwise noted, 10 μL of 2 μmol/L G4 DNA was immobilized for 60 min in a dark, high-humidity chamber. The electrodes were thoroughly rinsed with DIUF water and dried with nitrogen. The surface was backfilled with 6-MCH by incubation with 10 μL of 2 mmol/L 6-MCH solution in the same PBS buffer as the immobilization for 1 h at room temperature, in a dark, high-humidity chamber. The device was rinsed for 30 s using DIUF water, and again dried with nitrogen. To study the hybridization interactions, the PDMS chamber with a 2.5 mm diameter hole was filled with the working buffer described with each set of experiments.

### *5.2.4 Melting-curve analysis*

For G-quadruplex DNA melting-curve analysis, all electrochemical measurements were performed with an electrochemical workstation (CHI1040c, CH Instruments Inc., Austin, TX, USA). Sample temperature was controlled and monitored (as discussed above for the set-up in Section 3.6.2 and 3.6.3 using the embedded platinum thin film as a PRT. The temperature was increased incrementally, periods of 15 s were allowed to equilibrate the sample, and then 10 s were allowed to acquire the square wave voltammetry (SWV) scan for that temperature. SWV was carried out in a potential window to centering the MB peak, typically from −0.70 to −0.30 V (slight shifting due to the platinum pseudoreference electrode variability), with a 0.001 V interval, 60 Hz

frequency and 0.025 V amplitude with anodic current positive. Baseline correction was performed in the software by fitting a straight line to the minima located on either side of the MB peak and then subtracting the baseline from the peak current to measure the peak height. All data were plotted in Origin (OriginPro 2016, OriginLab Corp., Northampton, MA, USA).

### *5.2.5 XPS sample preparation and analysis*

1 µL of 200 µmol/L G4 DNA was reduced with 2 µL of 20 mmol/L TCEP in DIUF. The devices were piranha cleaned for 2 min, rinsed with DIUF and dried with nitrogen. The devices were electrochemically cleaned as described previously with 20 µL of 0.5 mol/L $H_2SO_4$. Probe tips were used to achieve contact to the electrode bond pads since the devices were not mounted on a PCB, where normally the bond pads would be wire bonded to electrical contacts. After cleaning, the devices were rinsed with DIUF, and dried with nitrogen. The DNA was then diluted in PBS1001 to the respective incubation concentrations, and 10 µL of the solution was placed on the device in a high humidity chamber. A range of immobilization concentrations were analyzed on each of three days (Day 1: 0.002, 0.02, 0.2, 2, and 20 µmol/L; Day 2: 0.05, 0.5, 1, and 2 µmol/L; Day 3: 0.01, 0.02, 0.05, 0.1, 0.5, 1, 2, 5, and 10 µmol/L). After 60 min, the devices were then rinsed, dried with nitrogen, and then incubated in 10 µL of 2 mmol/L 6-MCH for an additional 60 min. The samples were rinsed with DIUF, dried with nitrogen, and placed under vacuum of the XPS within 1 hour. (Note on concentrations: G4 Batch 1 was used for the first 2 days and reconstituted based on the amount provided by the

vendor. UV-concentration checks were done on aliquots of the stock solution at room temperature and found the concentrations to be lower than expected, but the UV-Vis system did not have a thermal block for proper quantification when the G-quadruplex is unfolded at 90 ºC. A new stock solution was made, G4 Batch 2 and used for Day 3. As seen by the overlay of data for different days (**Figure 5.7** in Section 5.3.2), there is not a noticeable difference in the immobilized concentrations for Day 3.)

XPS collection and analysis was done by Dr. Kristen L. Steffens in the Biomolecular Measurements Division at NIST. XPS analysis was performed using a Kratos Analytical Axis-Ultra DLD X-ray Photoelectron Spectrometer with a monochromated Al Kα source (150 W) and a nominal circular analysis area of 110 μm diameter, detected normal to the surface. The mono(Al) x-ray source impinges the sample surface at an angle 60 degrees from the surface normal. Low resolution survey scans (160 eV pass energy, 0.5 eV step size) were obtained at each position. In addition, high resolution scans (40 eV pass energy, 0.1 eV step size) were measured for Au 4f, P 2p, S 2p, C 1s, N 1s, and O 1s. To prevent charging of the sample, the charge neutralizer (electron flood source) was on during the data collection. XPS curve-fitting and analysis was performed using CasaXPS software (v. 2.3.1PR1.0). Most peaks were fit with a 70% Gaussian/30% Lorentzian peak shape, after subtracting a linear background. For Au 4f, a 10% Gaussian/90% Lorentzian peak shape was used along with Shirley background. The binding energy scale was calibrated to the Au $4f_{7/2}$ peak at 84.0 eV.

### *5.2.6 $d(T)_{24}$ sample preparation*

A similar procedure to Section 5.2.3, was done. In short, to reduce disulfide bonds and cleave the protecting thiol group, 1 µL of 100 µmol/L $d(T)_{24}$ DNA in TE Buffer was mixed with 2 µL of 20 mmol/L TCEP in DIUF water at room temperature in the dark for 90 min. The solution was then diluted to a DNA concentration of 2 µmol/L with 100 µL PBS250. The solution was then diluted again to 50 nmol/L in PBS250. After device cleaning, 10 µL of 50 nmol/L $d(T)_{24}$ was immobilized for 60 min in a PDMS well. The surface was backfilled with 6-MCH by incubation with 10 µL of 2 mmol/L 6-mercaptohexanol solution in the same PBS buffer as the immobilization for 1 h at room temperature, in a dark, high-humidity chamber. To study the thermal response of the $d(T)_{24}$ sequence, the PDMS chamber was filled with PBS250.

## 5.3 Results and discussion

As shown in **Figure 5.2**, it was hypothesized that the immobilized G-quadruplex would be folded at low temperature with the MB fixed in a position offering lower electron transfer to the electrode, and as the G-quadruplex unfolded, the flexibility would allow the MB to approach the surface, producing a higher current. Initial electrochemical measurements were done at high salt concentrations to stabilize the G-quadruplex and to support the electron transfer on the surface as described by Xiao and coworkers.[17] Preliminary results for immobilized G-quadruplex produced by a previous graduate student, Dr. Zuliang Shen, showed feasibility for monitoring this biomolecule, but also indicated further optimization was required.[123]

### *5.3.1 Observed variability of thermal profiles*

Initial results analyzed in the presence of 1 mol/L $Na^+$ and 1 mmol/L $Mg^{2+}$ all showed an increase of current with temperature as described by Shen, but the shape of the curved were initially not reproducible. In order to bring salt concentrations closer to physiological relevant conditions, the sequence was reduced in TCEP, immobilized at the existing salt concentrations (2 μmol/L G-quadruplex in PBS1001), and then the running buffer salt concentration was reduced to 100 mmol/L $Na^+$ and variability was observed. Improvements were therefore incorporated to operational schemes (as described in Chapter 3). Most importantly, automated voltage control and temperature monitoring were added to the interfacing program so that temperature set points could be monitored and controlled rather than voltage set points (which can vary the input power and thus the heating ramp between devices). Two examples of the thermal profiles are shown in **Figure 5.4.** The data was collected with ECP Version 1 as described in Section 3.6.1.2.

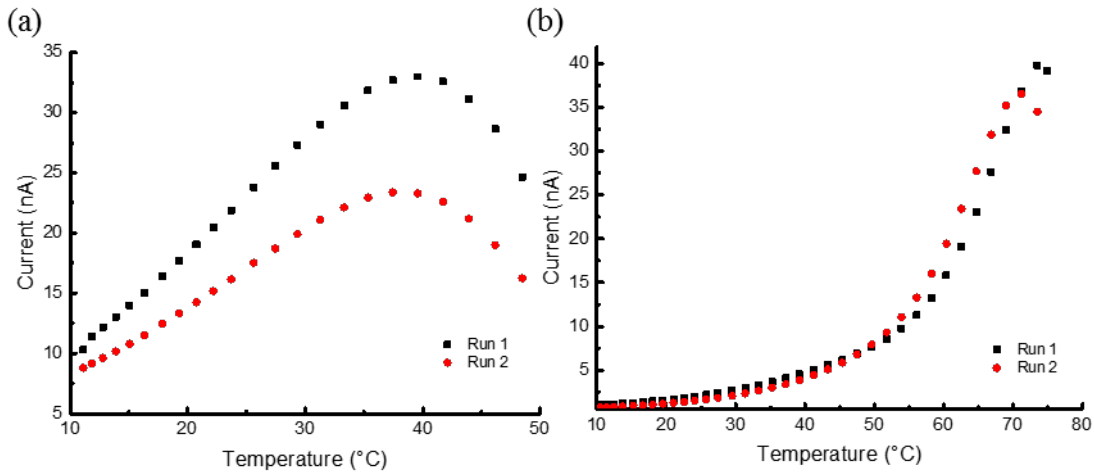


**Figure 5.4.** Case examples of variability in electrochemical thermal profiles of G-quadruplex in PBS100. The first thermal profile was collected (Run 1), allowed to equilibrate to room temperature, and then incubated for 20 min at 10 °C, before repeating (Run 2). Data shown was collected on Device 7 from Wafer 8 on (a) Day 1 and (b) Day 2.

Early concerns centered on the premise sample preparation variability was not understood. Initially, to address the concern of sample preparation variability, investigations into duplex DNA studies were investigated to better understand the complexities of surface chemistries required before resuming investigation on the G-quadruplex systems (Chapter 4). When resuming investigation into the G-quadruplexes, there was a concern that the packing density for the immobilized species might be too high, allowing the tethered sequences to interact with neighboring strands, and not form an intramolecular G-quadruplex.

### *5.3.2 Characterizing surface coverage*

To troubleshoot the issue of coverage (density) of DNA on the electrode surfaces, researchers have previously used the amount of ruthenium hexamine coordinated to the

phosphate backbone of DNA to approximate the charge and therefore the concentration of DNA on the surface.[12-13] This method is dependent on exposed phosphates (typically done with single strand or duplex DNA) and is reported in molecules/cm$^2$.[12] In order to employ this approach to obtain DNA density, current values from the ruthenium rely more heavily on a known applied potential and a fixed working area.

In this work, the platform was designed to probe changes in current of a known redox active component. Additionally, any material typically used to contain the analyte solution (here a PDMS well) covers the electrode traces is designed to be removable to avoid it being oxidized during the piranha and sulfuric acid cleaning. Therefore, in our experiments, a removable PDMS well was used, but the placement of the well was done by eye, meaning that while it always included the three relevant electrodes, there could be some variability in the area of the electrode traces included in the sample solution. Additionally, a pseudoreference electrode was used, and therefore the potentials are not as precise as using a true reference electrode such as Ag/AgCl. Another measure to calculate the surface density is to use the current of the MB label,[17, 170, 180] but if the current is increasing with temperature, it is unclear what current value to use (room temperature to compare to literature or high temperature to use the maximum current). Therefore, to overcome these challenges, a non-electrochemical method was used for a more complete analysis of the coverage of DNA on the surface.

The quantification of DNA on Au electrodes was developed using X-ray photoelectron spectroscopy (XPS) by Petrovykh and coworkers.[12, 181] XPS is a

characterization method that can measure the chemical composition of surfaces by measuring the energy of photoelectrons from the surface. For XPS sample analyses, the probe density on the surface should closely represent the preparation done for the electrochemical experiments. Due to the limited number of the current-generation devices available, and because the sample holder bar of the XPS instrument utilized can readily fit approximately 12 devices at once, multiple XPS samples were prepared on older device platforms. The older generation devices had oxide peel-up and could not be used for electrochemical experiments, but the gold working electrode areas and surfaces were prepared with the same method as the current generation of devices used for electrochemical studies. Therefore, analysis of these samples should offer a good approximation of the immobilization density as a function of incubation concentration.

Since DNA has a high proportion of nitrogen in the nucleobases (**Figure 5.5**), the nitrogen signal (N 1s) provided a unique feature attributable to DNA. The signal intensity from the DNA thiol attachment (S 2p) was both small and expected to be dominated by the abundance of sulfur atoms from 6-MCH SAM compared to the sulfide in the DNA attachment, and therefore is not a good indicator of the quantity of DNA.

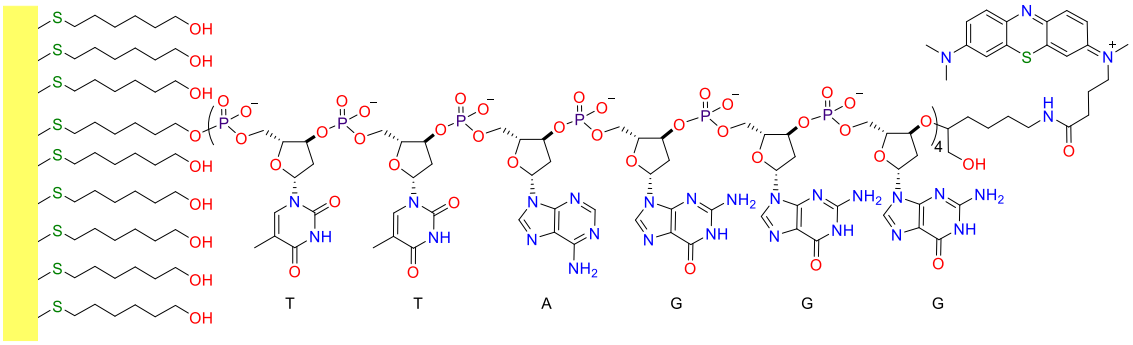


**Figure 5.5.** Schematic of DNA-SAM surface preparation highlighting elemental components of the molecules: carbon (black), sulfur (green), oxygen (red), nitrogen (blue), and gold surface of the working electrode (yellow).

**Figure 5.6** shows representative peaks for each of the region scans performed on Day 2. The phosphates from the backbone of the DNA can also be measured but are significantly lower in intensity to the extent that it is difficult to quantify above the noise of the background (**Figure 5.6d**). Additionally, the oxygen peak attributed to the silica substrate exhibited differential charging in some cases, causing it to overlap with the neighboring Au 4p peak (**Figure 5.6a**). The green curves were measured for a device incubated for 60 min with 2 µmol/L G-quadruplex DNA in PBS1001 (original conditions used by Xiao et. al. and Shen),[17, 112] and then backfilled with 10 µL of 2 mmol/L 6-MCH in the same buffer for 60 min. The black curves are of a device incubated in only PBS1001 during the immobilization step and then incubated in 6-MCH.

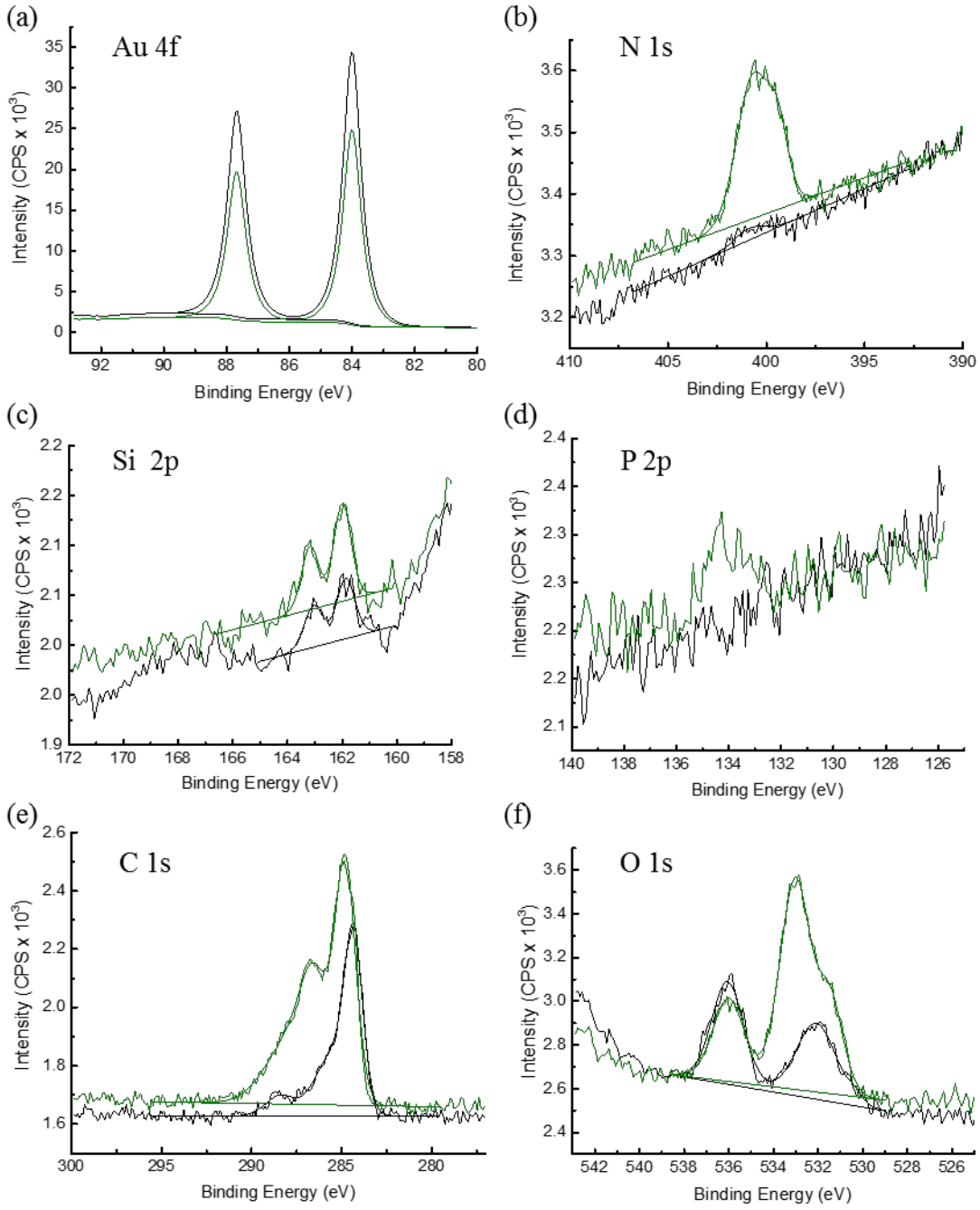


**Figure 5.6.** XPS regions (a) Au 4f, (b) N 1s, (c) S 2p, (d) P 2p, (e) C 1s, and (f) O 1s of 2 µmol/L G-quadruplex DNA (green) compared with 6-MCH SAM (black) as prepared on Day 2.

Because of the large aperture size chosen to obtain a higher signal intensity, only one spot per sample was taken per device (each device having a single concentration), but data were collected for multiple immobilized concentrations on three different days (Day 1: 0.002, 0.02, 0.2, 2, and 20 µmol/L; Day 2: 0.05, 0.5, 1, and 2 µmol/L; Day 3: 0.01, 0.02, 0.05, 0.1, 0.5, 1, 2, 5, and 10 µmol/L). All immobilization steps were done for 60 min in the respective solution and then followed with 60 min in 6-MCH. Due to low signal-to-noise ratios in the spectra of S 2p and P 2p (**Figure 5.6c** and **d**), the component analysis for these species shown in **Table 5.1** does not exhibit an measurable increase in the amount of P 2p with increasing amounts of immobilized DNA. Lower S 2p signal intensities are detected for the Au and buffer samples compared to the rest of the SAM-containing samples, which correlates to the high amounts of thiol in the 6-MCH SAM.

**Table 5.1.** XPS region abundance data from Day 2 of analysis.

| | Au 4f % | C 1s % | N 1s % | O 1s % | P 2p % | S 2p % |
|---|---|---|---|---|---|---|
| Au | 59 | 27 | 0.39 | 13 | 0.00 | 0.00 |
| Buffer | 54 | 29 | 3.22 | 15 | 0.00 | 0.05 |
| SAM | 53 | 31 | 0.00 | 15 | 0.73 | 0.73 |
| 0.05 µmol/L | 42 | 33 | 4.09 | 19 | 1.01 | 0.86 |
| 0.1 µmol/L | 43 | 31 | 3.13 | 22 | 0.33 | 0.85 |
| 0.5 µmol/L | 33 | 39 | 6.28 | 18 | 2.24 | 1.14 |
| 1 µmol/L | 31 | 41 | 6.78 | 20 | 1.02 | 1.02 |
| 2 µmol/L | 28 | 44 | 6.47 | 19 | 1.50 | 0.85 |

Due to the presence of nitrogen in the DNA oligomer that is not present in the 6-mercapotohexanol, the amount of DNA on the surface will track with the amount of

nitrogen detected. The area of the N 1s spectral region was plotted vs. immobilization concentration to produce the curve in **Figure 5.7**.

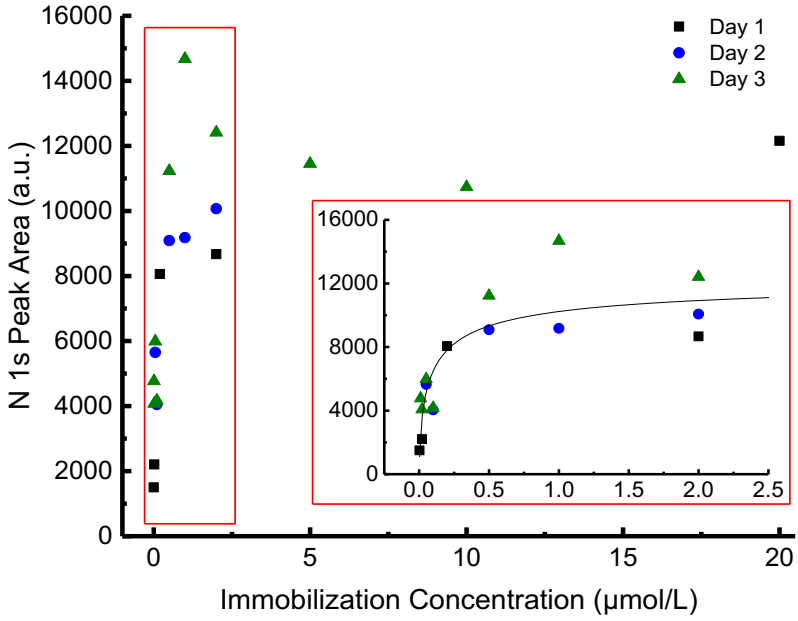


**Figure 5.7.** N 1s region area as a function of immobilization concentration of G-quadruplex DNA. A Hill fit was performed on the full concentration range of all three data sets and shown in the inset.

Although there is some variability in the samples, the overall trend showed that there was an increase in the N 1s signal, which reaches an approximate saturation above ~ 1 µmol/L. In addition to the N 1s increase, the Au 4f intensity was attenuated with the increasing amount of DNA on the surface and showed a plateau after ~ 1 µmol/L (**Figure 5.8**).

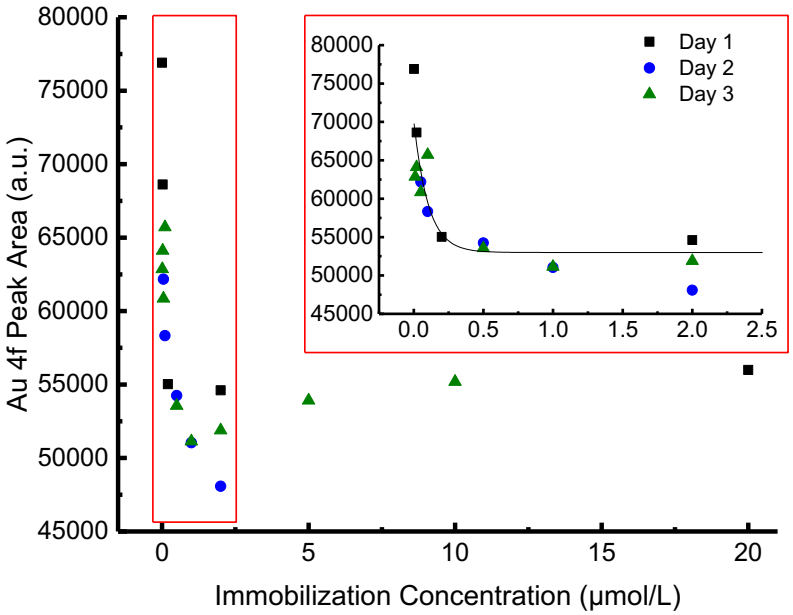


**Figure 5.8.** Attenuation of Au 4f region area as a function of immobilization concentration of G-quadruplex DNA. An exponential decay fitting was performed on the full concentration range of all three data sets and shown in the inset.

The plotted correlation provided an opportunity to estimate where the concentration of DNA saturates and then adjust the immobilization concentration to significantly lower values in order to minimize intermolecular forces on the surface.

### *5.3.3 Varying immobilized density through concentration control*

Based on the XPS results showing a saturation of N 1s signal above 1 µmol/L the immobilization concentrations for electrochemical measurements were decreased 10-fold from 2 to 0.2 µmol/L (**Figure 5.9a** and **b**). The maximum current measured did not seem to decrease drastically, so the immobilization concentration was then decreased another 10-fold to 0.02 µmol/L, but the current read-outs of the SWV were too low to process presumably because the immobilized coverage supported only weak

signal. The concentration was then increased to 0.1 µmol/L to achieve the curves in **Figure 5.9c**. Each data set in **Figure 5.9** is an overlay of two different devices with the same sample preparation measured simultaneously with the 2-device set-up functionality described in Chapter 3.

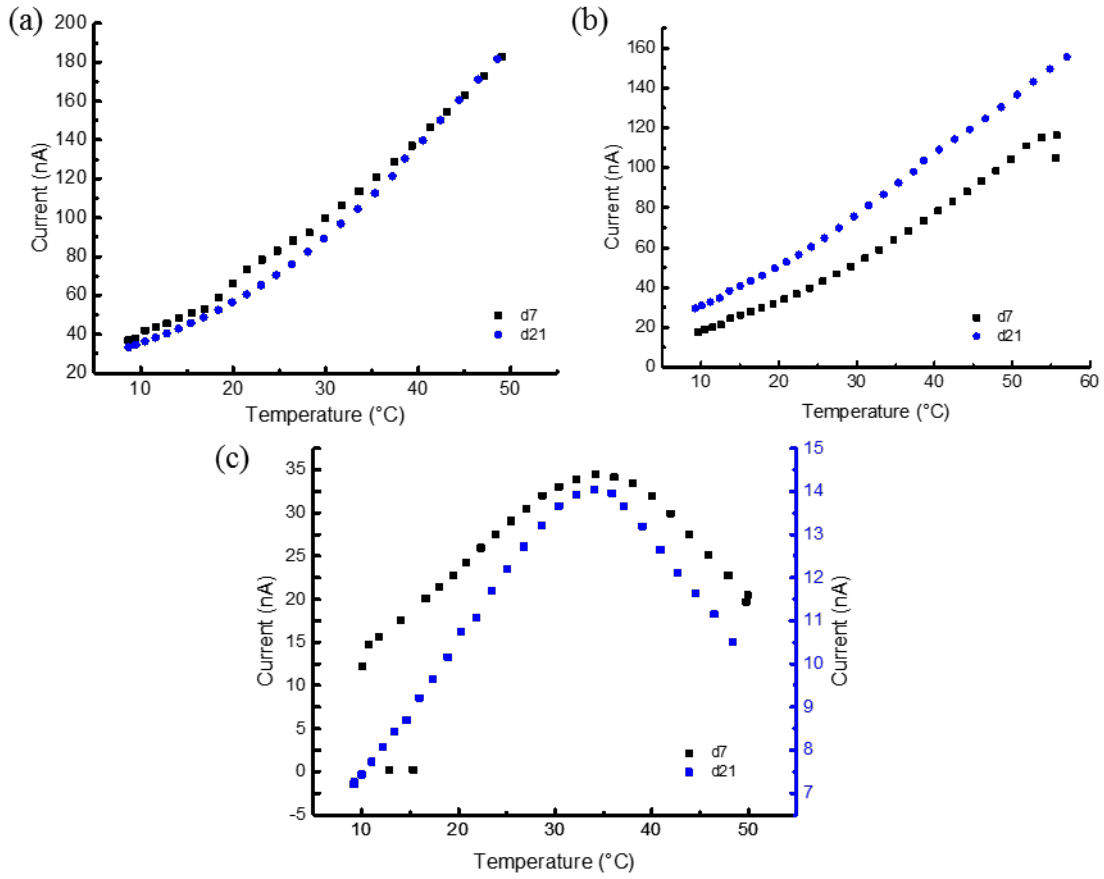


**Figure 5.9.** Temperature-dependent electrochemical measurements on G-quadruplex DNA immobilized at (a) 2 µmol/L, (b) 0.2 µmol/L, and (c) 0.1 µmol/L in PBS1001. Each set was taken on two devices on the same day: Wafer 10 Device 7 (black) and Device 21 (blue).

It is clear that decreasing the immobilization concentration affected the shape of the thermal profiles, but they were still not providing a sigmoidal shape as expected for thermally-driven transition from a completely folded structure to an unfolded

structure. (For a further discussion of context of initial and subsequent confirmations see Section 5.3.9.)

### *5.3.4 Effects of annealing before immobilization*

One concern was the G-quadruplex may have not been folded correctly before immobilization. Therefore, an annealing step was added immediately prior to immobilization. In the preliminary experiments the annealing was done by placing the reduced DNA in a thermal block at 90 °C for 10 min and then allowing it to slowly cool by quickly wrapping the Eppendorf tube in aluminum foil to slow the cooling rate (improvements to this step will be discussed in next section). The salt concentration for all steps was lowered from 1 mol/L $Na^+$ with 1 mmol/L $Mg^{2+}$ to 250 mmol/L $Na^+$. Lastly, the immobilization concentration was chosen to be between the previously undetectable level of 10 nmol/L and the previous lowest detectable level of 0.1 µmol/L (in PBS1000). **Figure 5.10a** shows two data sets of electrochemical measurements for samples immobilized with 50 nmol/L G-quadruplex for 60 min. **Figure 5.10b** shows two data sets incubated in 50 nmol/L G-quadruplex at 4 °C overnight before analysis. Due to the poor signal attributed to the lifetime of the devices (potentially due the incubation in buffer overnight), **Figure 5.10b** is collected on two separate days. All data sets show the same overall trend of an increasing current to a maximum between 45 °C and 50 °C.

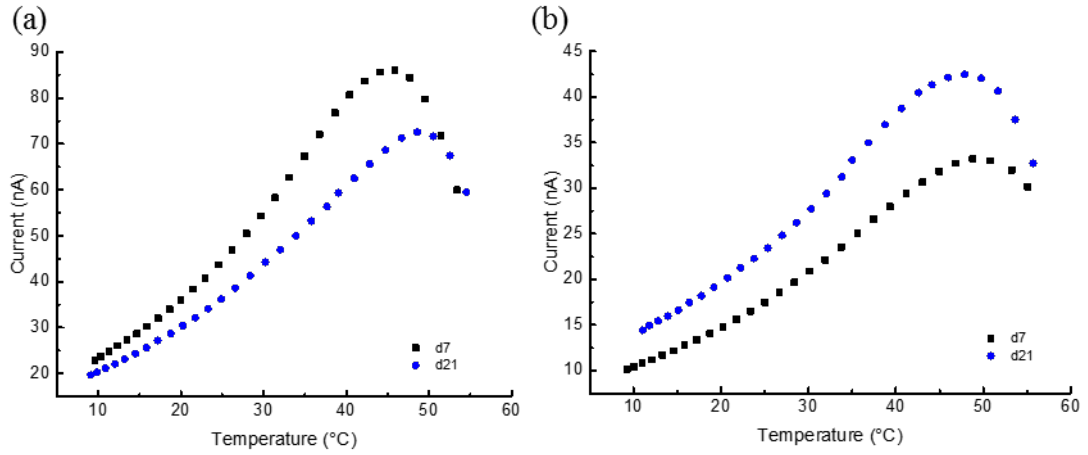


**Figure 5.10.** Temperature-dependent electrochemical measurements on G-quadruplexes incubated at 50 nmol/L and annealed prior to immobilization in PBS250. (a) immobilization for 60 min of two devices on the same day: Wafer 10 Device 7 (black) and Device 21 (blue) and (b) immobilization overnight. Data shown for two different days: Wafer 10 Device 7 (black) and Device 21 (blue).

### *5.3.5 Incorporation of PID control and thermal block anneal*

The anneal step as described previously did not have a control cool and when probed with a thermocouple, upon removal from the thermal block, the outside of the Eppendorf tube would cool to room temperature within a few min even in large amounts of aluminum foil. To make the anneal more repeatable, a ThermoMixer (Eppendorf) was used to heat the reduced DNA at 90 °C for 10 min and then cool to 20 °C at a rate of 1 °C/ min. Also, improvements to the automation, as described in Section 3.6.3, implemented to have the temperature controlled by a PID with fixed temperature set points. The PID program involved incubation of 10 min at 10 °C, and then heated at a rate of 1 °C every 25 s (15 s for equilibration and 10 s for electrochemical analysis). The changes helped make the temperature ramp more reproducible although there still were some temperature-dependent shifts based on

different devices and the magnitude of the current change would also vary. **Figure 5.11** shows electrochemical measurements prepared by annealing the G-quadruplex in the Thermomixer and then incubating the devices in 50 nmol/L G-quadruplex for 60 min. The thermal profiles utilize the 2-device setup with PID control.

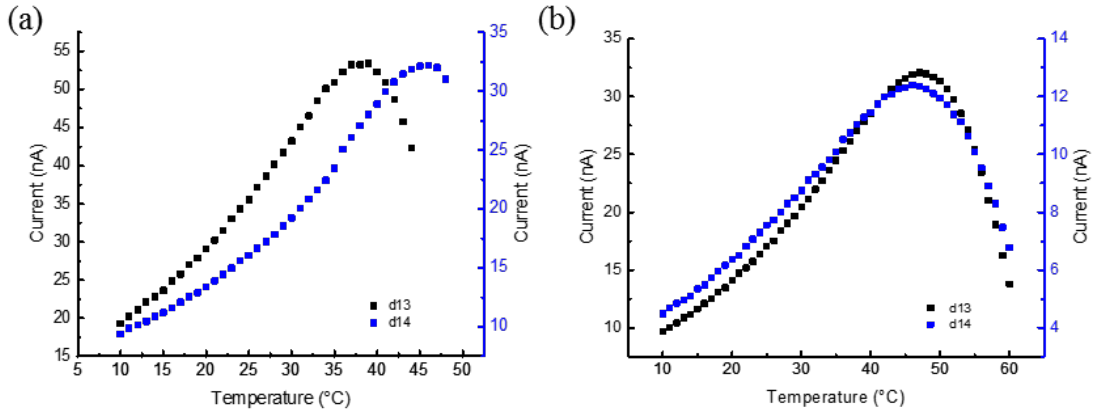


**Figure 5.11.** Temperature-dependent electrochemical measurements on G-quadruplexes incubated at 50 nmol/L and annealed with thermal block control prior to immobilization in PBS250. Each set was taken on two devices, Wafer 10 Device 13 (black) and Device 14 (blue), on Day 1 (a) and Day 2 (b).

### *5.3.6 Linear correction at low temperatures*

Based on the data presented in **Figure 5.11**, there appears to be a linear portion of the melting curve, especially at lower temperatures. Our original hypothesis was that this could be due to the distance-dependent diffusion of MB as a function of temperature, and possibly not a consequence of the structure unfolding. If that linear correction is extrapolated and subtracted, then the analysis can focus on the change in current above the linear component. To consider the way removal of this component would affect the profile, a line of best fit was done with the data points from 10 to 20 °C (**Figure 5.12a, solid red line**). The slope of the linear fit was $6 \times 10^{-10} \pm 3 \times 10^{-10}$ $^{o}C^{-1}$ and had an

intercept of 7 x $10^{-9}$ ± 3 x $10^{-9}$ A (standard deviations calculated from 6 replicates). Using the individual slope and intercept from the fitting from 10 to 20 °C, that component was extrapolated to form a new "baseline" (**Figure 5.12b, red dashed line**). Then the "baseline" subtraction could be performed giving the blue curve (**Figure 5.12a** and **b**). The resulting figure could be then analyzed with a Boltzmann fitting to determine if there was an inflection point in the nonlinear component which could be the melting temperature, $T_m$ (**Figure 5.12b**). Because of the steep decrease in current after the maximum, the data sets included in the fitting were selected from the lowest temperature to one to two points after the maximum current to achieve a better fit. In the example below the inflection point, or possible $T_m$, was determined to be 39 °C. The experiment was repeated for a total of 6 thermal profiles. The average inflection point, or possible $T_m$, for those experiments was determined to be 34 ± 3 °C. The standard deviation was determined from the calculation of the $T_m$ of the 6 replicates. This analysis was performed to attempt to separate the linear component from the non-linear component and although the term, $T_m$, is used, further investigation needs to be done to confirm if the inflection point is due to the G-quadruplex unfolding on the surface.

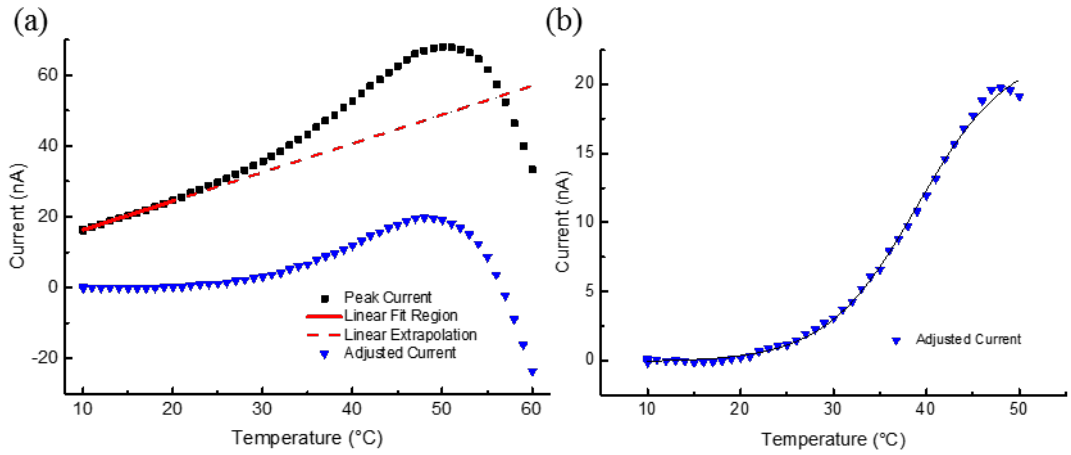


**Figure 5.12.** Temperature-dependent electrochemical measurements with PID control on G-quadruplexes incubated at 50 nmol/L and annealed with thermal block control prior to immobilization in PBS250. (a) Thermal profile (black) along with linear correction (red), resulting in the corrected profile (blue). Linear correction at low temperatures (10 to 20 ºC) (solid red) is shown along with the extrapolation (dashed red). (b) Boltzmann fitting of adjusted current values from 10 ºC to two points after the maximum showing an inflection point at 39 ºC.

The results after the linear correction produced sigmoidal-like curves, which would be what was expected if the G-quadruplex structure was going from a structure that the MB was primarily in the position farther away from the electrode and then unfolded to a more flexible structure, increasing the measured current. The standard deviations in the $T_m$ values were larger than were expected and it is understood that this larger standard deviation could be problematic for discerning relatively small ligand-modified $T_m$ shifts. Since the goal of the platform was to be able to measure a shift in the $T_m$, the capabilities of detecting stabilization effects were investigated next to test if a shift at high concentrations was even observable. Two ligands were chosen that bind to G-quadruplexes to see if there was a measurable stabilization effect, as evidenced an increase in $T_m$.

### *5.3.7 Effects of small molecules*

Diminazene aceturate (DMZ) is a known G-quadruplex binding ligand and has been shown to stabilize the telomeric G-quadruplex.[155] Upon binding, it was expected the G-quadruplex would be stabilized and therefore unfold at a higher temperature. Before fine tuning, an initial high concentration of DMZ was used to see if there was an effect. **Figure 5.13** shows four electrochemical data sets of the thermal profile as prepared and analyzed in Section 5.3.6, but in the presence of 10 µL of 10 µmol/L DMZ in PBS250. The prepared G-quadruplex/SAM was incubated with the DMZ for approximately 15 min while the set up was assembled and for 10 min at 10 °C and then heated at a rate of 1 °C every 25 s.

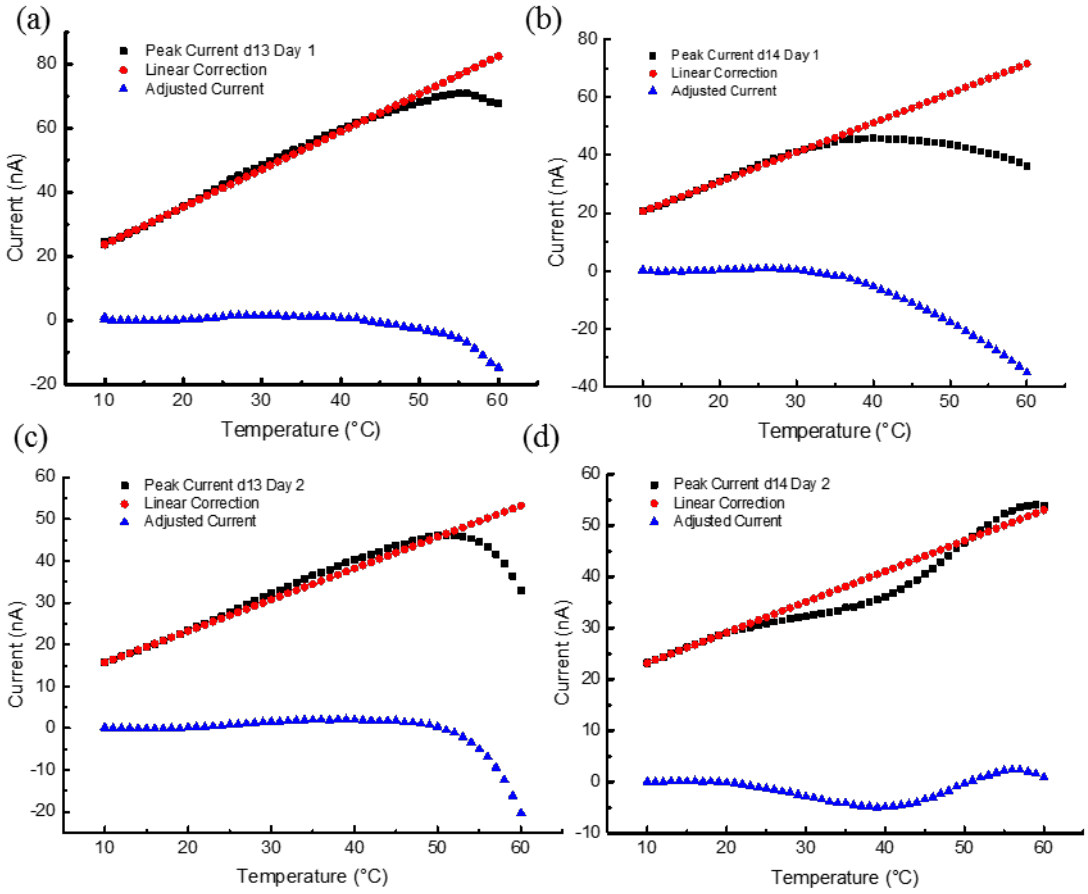


**Figure 5.13.** Temperature-dependent electrochemical measurements on G-quadruplexes incubated at 50 nmol/L and annealed with thermal block control prior to immobilization in PBS250 in the presence of 10 µmol/L DMZ. Each set was taken on two devices, Wafer 10 Device 13 (a and c) and Device 14 (b and d), on Day 1 (a and b) and Day 2 (c and d).

Rather than see the current component (black) above the linear baseline, the current increase remained linear for a larger temperature range when compared to the G-quadruplex without DMZ **(Figure 5.12**). The average slope of the linear correction factor was $9 \times 10^{-10} \pm 2 \times 10^{-10}$ $^{o}C^{-1}$ and had an intercept of $1 \times 10^{-8} \pm 3 \times 10^{-9}$ A (standard deviations calculated from all 4 replicates).

It is possible that the large excess of ligand could stabilize the structure or that it could be interfering with the electrochemical response. In order to better understand the nature of this factor, the concentration was lowered to 1 µmol/L DMZ (**Figure 5.14**). Two devices were analyzed on two separate days; one of the devices had a low irregular current response and therefore was not included in the dataset below. The results show a similar curve to the initial G-quadruplex (**Figure 5.11** and **Figure 5.12**) with more variability.

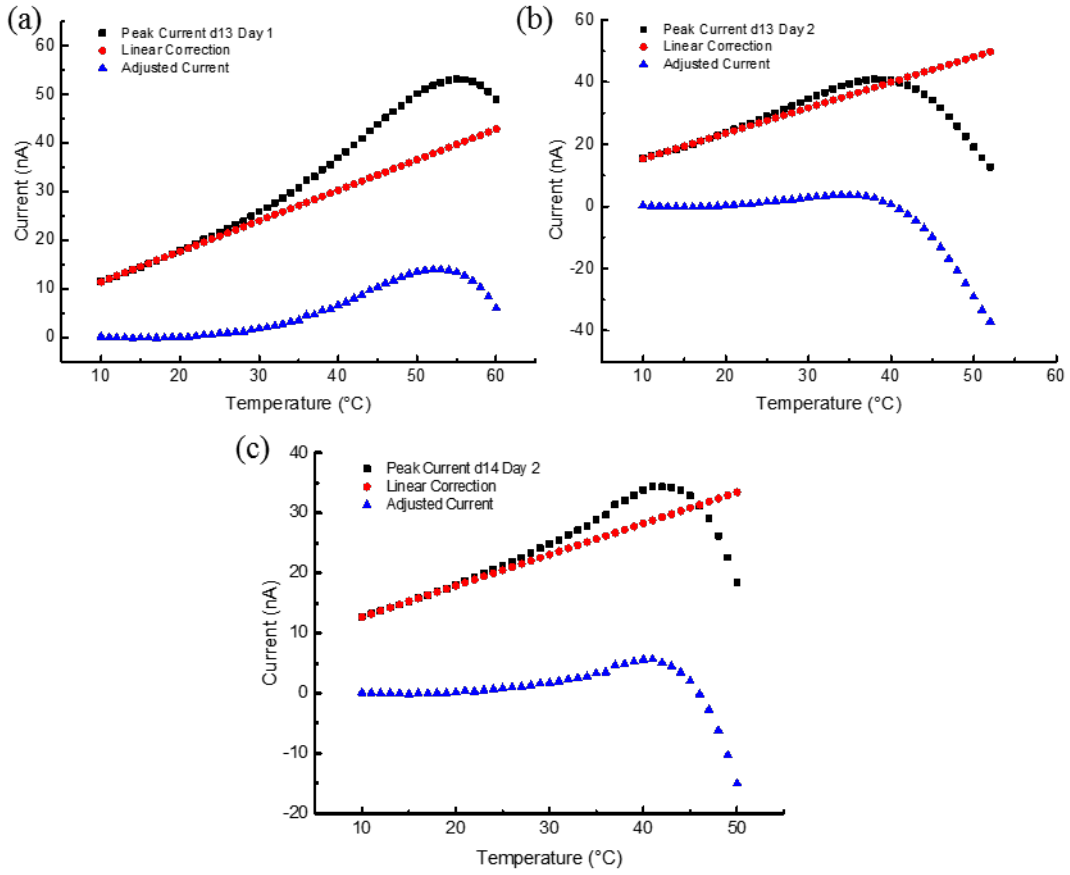


**Figure 5.14.** Temperature-dependent electrochemical measurements on G-quadruplexes incubated at 50 nmol/L and thermal block controlled anneal prior to immobilization in PBS250 in the presence of 1 µmol/L DMZ. Data sets were for (a) Wafer 10 Device 13 Day 1 and (b) Day 2, and (c) Device 14 Day 2.

The average slope of the linear correction factor was $7 \times 10^{-10} \pm 1 \times 10^{-10}$ $^{o}C^{-1}$ and had an intercept of $7 \times 10^{-9} \pm 1 \times 10^{-9}$ A (standard deviations calculated from 3 replicates). For the data sets above, the average $T_m$ was calculated to be 34 ± 6 ºC. The variability between samples is too large to make any conclusions about the stabilization effects of DMZ on surface immobilized G-quadruplexes.

To make sure the variability was not due specifically to the binding of DMZ, another ligand was also tested. SYUIQ-5, is a known to stabilize telomeric G-quadruplexes and inhibit telomerase activity.[178] Additionally, a new stock solution was used, G4 Batch 3, and to utilize the 2-device setup, one device was run as a control in the new batch with PBS250 and the second was incubated with 10 μmol/L SYUIQ-5. The data in **Figure 5.15** was collected on two separate days. Since Device 13 was produced more repeatable results, it was used for the samples with SYUIQ-5 and Device 14 was used for the control. The high current response and lack of maximum in the Device 14 data could be due to the variability of Device 14 or representative of the variability of the measurements. The noticeable feature is that the thermal profiles for the SYUIQ-5 show very little current increase with temperature.

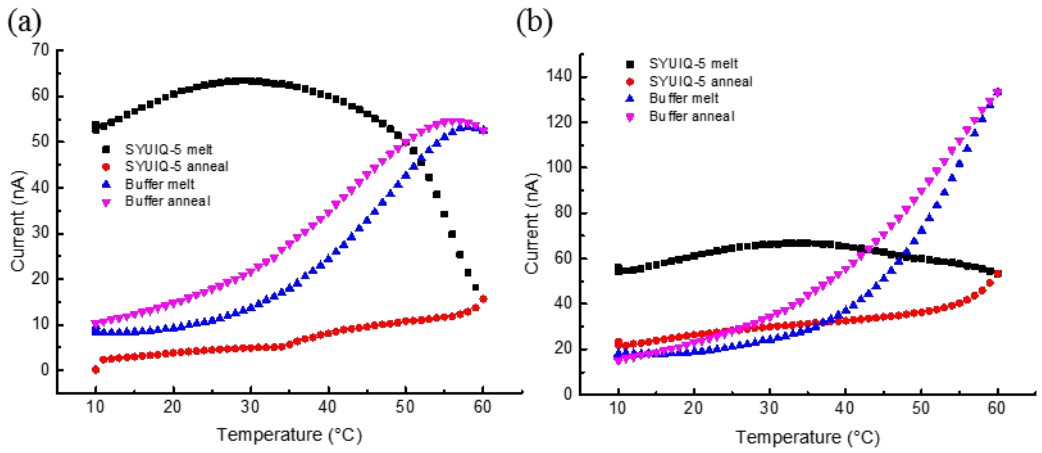


**Figure 5.15.** Temperature-dependent electrochemical measurements on G-quadruplexes incubated at 50 nmol/L and thermal block-controlled anneal prior to immobilization in PBS250 in the presence of 10 µmol/L SYUIQ-5 on Day 1 (a) and Day 2 (b).

The melting profiles in the presence of SYUIQ-5 were very different than the melting profiles of the G-quadruplex and of the melting profiles with DMZ. The current change is relatively small compared to the G-quadruplex in buffer, highlighting the need for further investigation of a simpler system to understand the temperature effects of a tethered MB sequence without a secondary structure.

### *5.3.8 Control experiments with d(T)$_{24}$*

Due to the increase of the linear component with the presence of ligands, a control experiment was performed with a DNA sequence of the same length as the G-quadruplex (24 nucleotides), but something that should have minimal intermolecular and intramolecular interactions. A poly-thymine sequence was chosen as it has been used previously for foundation electrochemical studies.[182] The samples were prepared in the same manner as the G-quadruplex, except without the annealing step. **Figure**

**5.16** shows that the $d(T)_{24}$ results did not give the expected linear behavior at as a function of temperature. Instead there was an initial increase, and then the current would decrease as a function of temperature. Because of the $d(T)_{24}$ results, the linear increase and correction in Section 5.3.6 cannot be attributed to an increase of diffusion of the MB to the surface and further studies need to be done to understand the cause of the linear increase in the G-quadruplex thermal profiles.

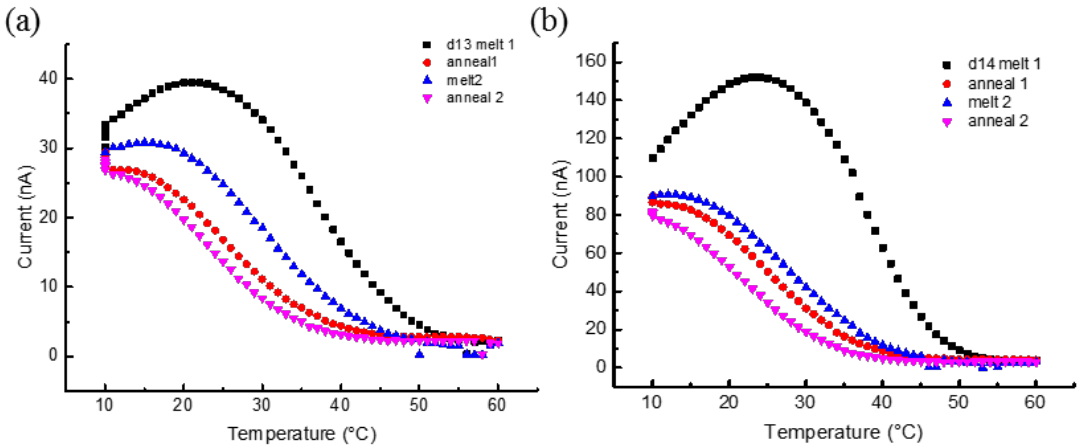


**Figure 5.16.** Example temperature-dependent electrochemical measurements on $d(T)_{24}$ melting profiles incubated at 50 nmol/L in PBS250 on Device 13 (a) and Device 14 (b) on the same day.

One of the major concerns with the $d(T)_{24}$ thermal profiles was that upon cooling the sample, the thermal profile was not completely reversible. This can be seen by the difference between the first melt (**Figure 5.16,** black) compared to the following anneal (red) and second melting (blue). This led to concern about desorption from the surface. With the PID control, the ramp rate was significantly slower than in the prior duplex measurements, resulting in longer periods of time spent at higher temperature, stressing the films. To measure if there was a temperature at the current ramp rate that

was not completely reversible, an interval ramp experiment was done. For the interval ramp, the sample was held at 10 ºC for 10 min, ramped from 10 ºC to 20 ºC, 19 ºC to 10 ºC, 11 ºC to 30 ºC, 29 ºC to 10 ºC, 11 ºC to 40 ºC, 39 ºC to 10 ºC, 11 ºC to 50 ºC, 49 ºC to 10 ºC, 11 ºC to 60 ºC, and 59 ºC to 10 ºC. Besides the initial incubation at 10 ºC, each set point was stepped at 1 ºC intervals and allowed either 15 s (**Figure 5.17a**) or 10 s (**Figure 5.17b**) to equilibrate, before running the SWV.

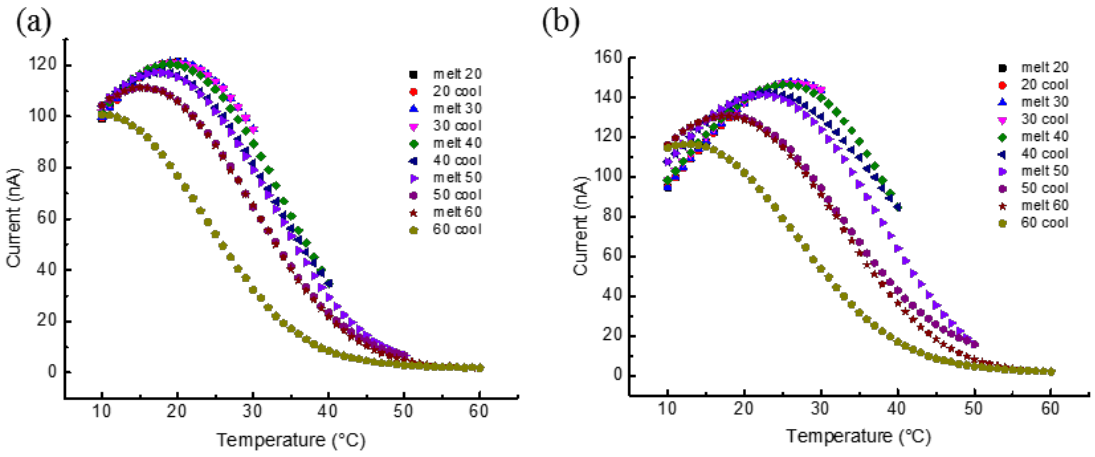


**Figure 5.17.** Temperature-dependent electrochemical measurements with interval ramping on $d(T)_{24}$ in PBS250 with (a) 15 s and (b) 10 s equilibration at each 1 ºC set point before SWV.

If there were issues of the thiol stability on the surface, it would be expected that the shorter equilibration time would have less desorption from the surface and therefore have less of a current difference from the start to the end of the experiment. Instead, there seems to be a larger current difference with the 10 s equilibration time. This could show that the longer equilibration time allows more of the solution to approach the temperature of the electrode surface and possibly minimize convection effects.

### *5.3.9 Complications of electron transfer measurements*

The major benefit of having an on-off system as presented in Chapter 4, is that the MB label is on the complimentary sequence that is either bound to the surface through hybridization or is in equilibrium in the solution (far from the electrode surface). Because SWV is a pulsed voltammetric technique that uses a forward and reverse pulse to account for any charging effects near the electrode, it increases the sensitivity to faradaic reactions, such as the oxidation and reduction of leuco-methylene blue and MB (**Figure 1.6**). The rate of electron transfer, $k_{ET}$ is controlled by the distance, d, as shown by **Equation 5.1** where $A$ is a preexponential factor, and decay constant, $\beta$.[101]

$$k_{ET} = Ae^{-\beta d} \qquad \textbf{Equation 5.1}$$

When MB-probe sequences are located in the bulk solution, the distance is so large that there is no measurable electron transfer. With the proposed system in **Figure 5.2**, the distance of MB is limited by the linker or bridge to the surface. Mass transport of the MB to the electrode surface can be grouped into three major categories: diffusion, convection, and migration.[88]

Migration is the movement of charged species due to an electric field.[88] It is not expected to have any issues of electric field effects with the microplatforms because of the use of either the thermoelectric modules or keeping the voltage to the PRT set to zero when the electrochemistry is running for the case of the active embedded PRT. Additionally, it is noted that there was not a difference in electrochemical response seen with the thermoelectric heating vs the resistive heating of the duplex system in Chapter 4.

Convection is the movement of a species based on the external mechanical energy from density gradients, stirring, or flowing of the solutions.[88] Because the temperature control is placed below the planar electrode system, the temperature of the surface of the electrodes will differ from the temperature of the bulk solution.[183] Contento and Semancik studied the temperature effects electrochemical response of potassium ferricyanide and ruthenium hexamine using a planar electrochemical device with an embedded platinum microheater.[113] Their models showed a signal enhancement at higher temperatures partially due to convection effects.[113] In our experiments, a 15 s of equilibrium at each set point should allow for the surface electrodes to reach equilibrium with the thermoelectric module, but it is not clear how the convection currents will affect the relative distance of the tethered MB on the surface and the temperature of the bulk solution.

Diffusion is the movement of species based on minimizing concentration differences, spontaneously flowing from high to low concentration areas.[88] The Arrhenius equation establishes the relationship between diffusion, D, and temperature, T, in **Equation 5.2** where $D_o$ is an empirical coefficient, $E_a$ is the activation energy for diffusion, R is the universal gas constant.

$$D = D_o e^{\frac{-E_a}{RT}} \qquad \textbf{Equation 5.2}$$

Researchers have shown that both the cooling and heating of microband electrodes follow the relationship from -10 ºC to 40 ºC.[184] As the amount of MB closer to the surface increase, to the amount of current measure also increases. The rate of diffusion of the MB to the surface can be affected by a wide range of factors: MB

interaction with nucleobases, MB screening at the electrode surface due to high packing density of DNA, flexibility of spacer/linker/DNA anchoring MB, instability of the immobilization and SAM.

MB is known to intercalate between base pairs and when tethered to the distal end of an immobilized duplex, the MB will bind to the end of the duplex and forcing the electron transfer to occur through the duplex.[18] Additionally, they showed that the electron transfer is affected by single-base mismatches forming lesions blocking the charge transfer pathway.[18] Silva and coworkers investigated the effect of having a redox label on the distal and proximal ends of a immobilized duplex and found that when the MB is close to the surface, screening effects are experienced compared to neutral ferrocene.[185] When the packing density of the DNA is high at the surface, the negatively charged phosphates can interact with the MB make it difficult for the MB to freely approach the surface.[185] It is presumed that the increase of temperature to the system would increase the flexibility of the SAM and allow more MB to reach the surface.

A key question to utilizing this method to screen for ligands is: does the G-quadruplex form the same structure on the surface as solution phase characterization methods?

As explained in the introduction of this chapter, the telomeric G-quadruplex, $d(TTAGGG)_4$, has been shown to form a basket structure in the presence of sodium ions in solution.[164] When tethered to the surface there are concerns with intermolecular interactions and also that the tethering to the surface affects the structure. To address

the effect of possible intermolecular interactions, the immobilization concentration was lowered while still allowing measurable current readouts.

Although it is well established that telomeric G-quadruplex forms a basket structure in the presence of sodium, Gray and coworkers have shown for the sequence d[AGGG(TTAGGG)$_3$] that the energy barrier between a potassium "hybrid" structure and the "basket" structure formed with sodium has an energy barrier of 1.4 to 2.4 kcal mol$^{-1}$.[186] Additionally, binding of TmPyP4 caused the conversion from the basket to hybrid form.[186] It is possible that the surface tethering would cause some conformations to be more stable than others. For example, if there was a structure that in solution had a loop that would wrap under the G-quadruplex structure near the same end that was tethered, the structure may either change in orientation, or adopt another conformation.

G-quadruplexes can also be stabilized by higher-order structures. Pagano and coworkers investigated a serious of repeating telomeric G-quadruplexes (TTAGGG)$_n$ and (TTAGGG)$_n$TT where n = 4,8, or 12.[187] They found that higher-order structures affect the stability of the G-quadruplexes and the unfolding may not be simple two-state melting process.[187] If these higher order structures are stabilizing the G-quadruplex in the form of "wires" on the surface, the thermal response will vary from the analysis of intramolecular G-quadruplexes.

A second key question relates to the difference in position of MB and being large enough to sense a difference in current. Recently, Bianchi and coworkers studied the telomeric G-quadruplex, Tel22 (d[A(GGGTTA)$_3$GGG] in 150 mmol/L KCl) with CD, ultraviolet resonance Raman (UVRR) scattering, and small angle X-ray and

neutron scattering (SAXS and SANS).[188] Their work showed that as the temperature increased, there was a change in population of anti-parallel basket-type and hybrid-type conformers, and that binding of Actinomycin D (ActD), an anticancer ligand, interacts with the nucleobases after the G-quadruplex unfolds which can be seen by the 3D models based on *ab-initio* calculations from their SAXS data (**Figure 5.18**).[188]

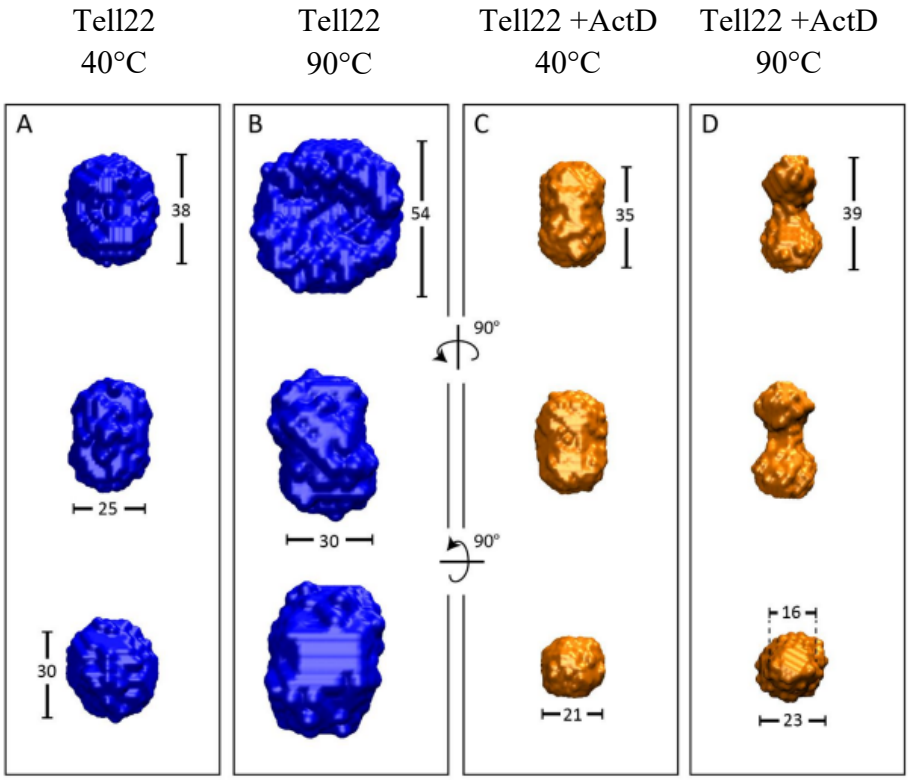


**Figure 5.18.** 3D models of Tel22 G-quadruplex in $K^+$ obtained by the ATSAS suite based on *ab-initio* calculations from SAXS data. Measurements are in Angstrom.[188] [Supplemental figure from Bianchi, F.; Comez, L.; Biehl, R.; D'Amico, F.; Gessini, A.; Longo, M.; Masciovecchio, C.; Petrillo, C.; Radulescu, A.; Rossi, B.; Sacchetti, F.; Sebastiani, F.; Violini, N.; Paciaroni, A., Structure of human telomere G-quadruplex in the presence of a model drug along the thermal unfolding pathway. *Nucleic Acids Research* **2018,** *46* (22), 11927-11938. Published by Oxford University Press and licensed under CC BY 3.0.]

As visualized by the 3D models in **Figure 5.18**, the melting changes the dimensions of Tel22 on the order of 5 to 16 Å, but the structure with ActD bound only

changes 2 to 4 Å.[188] Such slight changes in the dimension would be difficult to detect with a change in current. The binding of small molecules to the unfolded state could also support why there was relatively small current changes in the presence of SYUIQ-5 in **Figure 5.15**.

## 5.4 Conclusions

The possible complications discussed in considering the electrochemical results suggest that there is a wide area for further research. To understand these systems, more work needs to be done to probe the $d(T)_{24}$ sequences to understand how the electron transfer at the surface is affected by temperature fluctuations. Based on the initial increase of current below room temperature and then the decreasing current above room temperature, it is hypothesized that convection effects are influencing the electron transfer of MB. This is supported by the shorter equilibration times leading to more variability due to greater temperature differentials with the bulk solution. MB could also be interacting with the nucleobases or other intermolecular interactions could be occurring on the surface.

To investigate the G-quadruplex, the addition of longer spacers in the immobilization would allow for more flexibility of the structure to form the configuration favored in bulk solution analysis. Currently the sequence used has a 6-carbon thiol attachment and then an additional three bases (TTA) before the first guanine in the structure. The original work by the Plaxco group on the thrombin aptamer contained a 15 base pair spacer between the thiol attachment and G-quadruplex

portion of the sequence that binds to thrombin.[170, 189] For SERS melting studies, Meneghello and coworkers incorporated a hexaethyleneglycol spacer after immobilization of three disulfide attachments to increase the stability of the immobilization and to provide flexibility before the DNA sequence.[190]

Although the ideal case is to fully understand a complex system, the system proposed would be simpler if the G-quadruplex folding on the surface was reversible, allowing for analysis of a baseline, and then measure again in the presence of the ligand in question. Currently there are many variables that need to be tested methodically to understand the system in more detail and would benefit from a larger array system to screen for possible effects.

# Chapter 6 Conclusions and Proposed Work

## 6.1 Summary

Developing an electronic technology for acquiring thermal profiles of tethered analytes has the potential to enlarge the toolbox for bioanalytical HTS. Measurement of the thermal stability of biomolecular structures and the stabilization effects induced by ligands can be used to screen for binding of new drug molecules. In the platform developed in collaboration with the Semancik group at NIST and the Sintim group at UMD and Purdue, SWV, a highly sensitive electrochemical technique, was used as a cost-effective alternative to screen for thermal stability on the microscale.[22, 123] Initial features of the approach included localized and addressable temperature control of small-footprint elements, allowing for analysis of small-volume samples with compatible scale up to array formats.

In Chapter 2, enhancements of the device fabrication methodology resulting in higher quality Pt thin film, and better adhesion of the subsequent insulating oxide were described. The process involved switching from using metal lift-off processing of the Pt microheater and blanket deposition of PECVD oxide to depositing a Pt thin film with an additional Ti and $SiO_2$ or $Al_2O_3$ adhesion layer all in one tool. The oxide and fabrication steps were investigated both for film and process impurities and led to design and implementation of an ALD/PECVD/ALD sandwich oxide or a thicker annealed PECVD oxide.

Chapter 3 discussed the assembly of the completed devices and the incorporation of thermoelectric modules for temperature control and utilizing the embedded platinum thin films as a PRT. This approach prolonged the lifetime of the devices by utilizing devices with small insulation defects (as long as the PRT was not monitored at the same time as the electrochemical scan), while also allowing for localized temperature control below room temperature. Additionally, the thermal control and the electrochemical experiments were automated, increasing measurement repeatability. Further work on the ECP extended the program to enable simultaneous measurement on 2-device arrays, and also incorporated a software PID control for uniform temperature ramps.

Chapter 4 highlighted that both resistive heating and thermoelectric heating can be used successfully for the analysis of duplex DNA melting. The proof-of-concept experiments showed that, utilizing the reversibility of the melting profile of duplex DNA, a baseline thermal profile could be analyzed, a ligand added, and then the shift of the melting temperature could be quantified. Two known duplex binding ligands were tested, DMZ and proflavine, and two distinct shifts in the melting temperatures were measured.

In Chapter 5, steps taken to adapt the technology to immobilized G-quadruplexes were presented. Compared to the duplex DNA system which was highly reversible and resulted in a larger change due to the on-off approach, the G-quadruplex system was more challenging. Due to the G-rich nature of the G-quadruplex, a higher probability of intermolecular interactions existed (than for the duplex system),

especially as the G-quadruplex density increased. To better understand G-quadruplex immobilization as a function of concentration, XPS was performed. The XPS analysis guided experimentation to significantly lower concentrations, but there was still variability in the day-to-day analyses. Analysis in the presence of DMZ and SYUIQ-5 did show a change in the overall thermal profile, but not a simple shift like that observed for the duplex DNA system. Further investigations with a poly-thymine sequence of the same length as the studied G-quadruplex did not show the anticipated increase in electrochemical current with increasing temperature. Overall, the examination of both the poly-thymine and G-quadruplex sequences highlighted the need for more fundamental studies to support understanding of thermal profiling of such immobilized species.

## 6.2 Proposed work

While the duplex system achieved clearer stability results because the system offers a simple on-off electrochemical approach, it seems that the possibility exists to study intermolecular behavior of G-quadruplexes with the microplatform technology. The proposed system shown in **Figure 6.1** is designed to summarize a range of future work into one design, but each design change should be studied systematically first. Tsuji and Sintim have shown that a conditional riboswitch-peroxidase-mimicking sensor could be used to sense the presence of c-di-GMP.[191] This concept could be applied to G-quadruplexes on the surface. If the G-quadruplex structure is comprised of two DNA sequences that have a region that hybridizes with Watson-Crick base pairs, that region

would be stabilized by the formation and orientation of the G-quadruplex. One of these sequences could be tethered to the surface and the second sequence could be labeled with MB as demonstrated in this work. With this method, the denaturing of the structure, allowing for the MB-labeled sequence to diffuse in the bulk solution, would provide a clearer on-off detection method. The thermal stability of these systems could be investigated first, followed by a subsequent examination of ligand-induced stabilization of these structures.

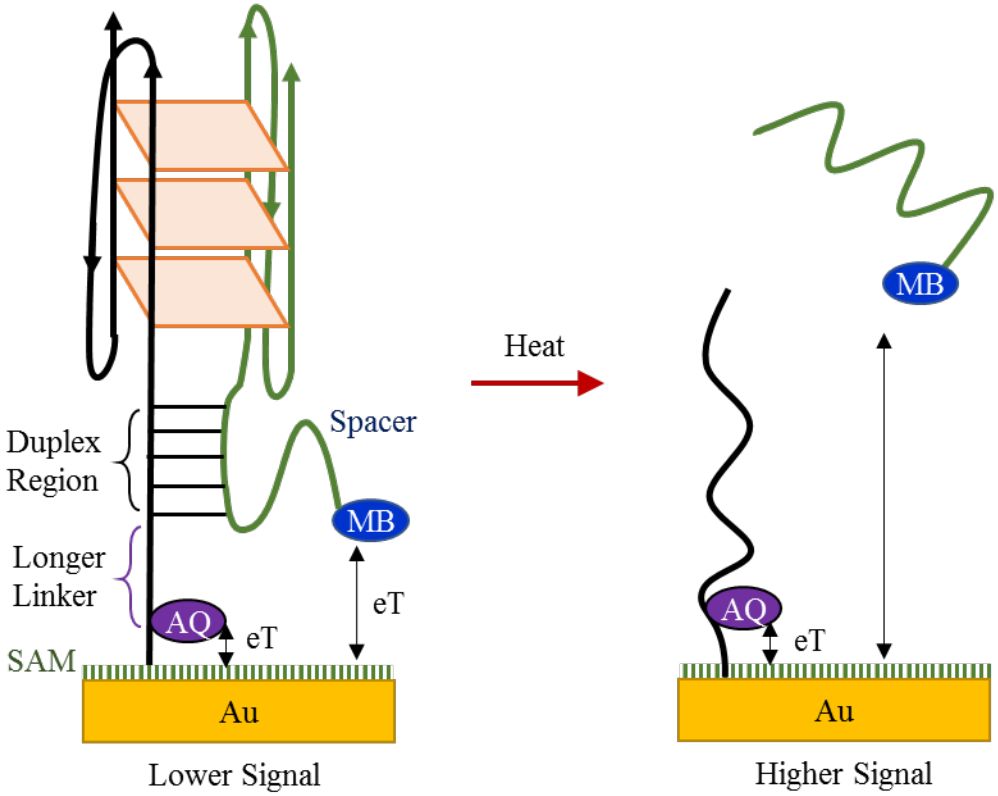


**Figure 6.1.** Schematic of on-off G-quadruplex/duplex hybrid system. Anthraquinone (AQ)-labeled immobilized strand (black) forming a dimeric G-quadruplex with the methylene blue (MB)-labeled sequence in solution. Upon melting the electrochemical signal of the AQ could be used as a reference to the expected decrease in MB current.

As discussed in Chapter 5, the utilization of a longer linker along with lower packing densities, should allow one to reduce the amount of intermolecular interactions with the immobilized sequences. Additionally, a second redox tag could be used as a reference to both quantify how much immobilized DNA is on the surface and to monitor for any desorption at higher temperatures. Using a two-redox probe system has been studied for both samples in whole blood,[192] and for investigating screening effects in duplex DNA.[185]

Overall to address the amount of characterization required for simpler stability-study systems and for fundamental interfacial understanding, the need to extend to larger device arrays is emphasized. The currently used potentiostat has a limitation of 8 simultaneous channels. In order to use all 8 channels, the SMU can rapidly switch between monitoring individual PRTs, but additional power supplies would be needed to control individual thermoelectric modules. The use of low-cost potentiostat circuits and multiplexing hardware would be beneficial as array sized is increased.

In the presented feasibility studies, simple PDMS wells were employed. They required pipetting of approximately 10 μL of analyte solution, and it was essentially impossible to remove the entirety of the solution without removing the well. In addition, pipetting analyte solutions into the well can change the total volume of liquid that functions as a heat sink above the device and was therefore minimized, if not avoided. Automation of the technology would be dramatically enhanced by replacing the manual analyte delivery, removal, and cleaning with a properly designed microfluidic system. While initial designs would require the microfluidic channels to

be removable for piranha cleaning, even a non-optimized microfluidic system would provide the mechanism to flow a range of concentrations and conditions over the devices significantly faster and more reliably than by using manual means. Further development could also allow cleaning procedures to be built into the microfluidic system, resulting in permanent integration of the sample delivery system. The optimization of microfluidics would also be very important for operation of multi-element arrays.

# Bibliography


1. Prescient & Strategic Intelligence: Biosensors Market Overview. www.psmarketresearch.com/market-analysis/biosensors-market (accessed Oct 20, 2019).

2. Market Research Engine Biosensor Market Report. www.marketresearchengine.com/biosensor-market-report (accessed Oct 20, 2019).

3. Clark, L. C., Jr.; Lyons, C., Electrode systems for continuous monitoring in cardiovascular surgery. *Ann. N. Y. Acad. Sci.* **1962,** *102*, 29-45.

4. Wang, J., Electrochemical glucose biosensors. *Chem. Rev.* **2008,** *108* (2), 814-825.

5. Turner, A. P., Biosensors: Sense and sensibility. *Chem. Soc. Rev.* **2013,** *42* (8), 3184-3196.

6. Swinney, D. C.; Anthony, J., How were new medicines discovered? *Nat. Rev. Drug Discov.* **2011,** *10* (7), 507-519.

7. Liu, J.; Cao, Z.; Lu, Y., Functional nucleic acid sensors. *Chem. Rev.* **2009,** *109* (5), 1948-1998.

8. Sassolas, A.; Leca-Bouvier, B. D.; Blum, L. J., DNA biosensors and microarrays. *Chem. Rev.* **2008,** *108* (1), 109-139.

9. Palecek, E., Oscillographic polarography of highly polymerized deoxyribonucleic acid. *Nature* **1960,** *188*, 656-657.

10. Drummond, T. G.; Hill, M. G.; Barton, J. K., Electrochemical DNA sensors. *Nat. Biotechnol.* **2003,** *21* (10), 1192-1199.

11. Carter, M. T.; Bard, A. J., Electrochemical investigations of the interaction of metal chelates with DNA. 3. Electrogenerated chemiluminescent investigation of the interaction of tris(1,10-phenanthroline)ruthenium(II) with DNA. *Bioconjug. Chem.* **1990,** *1* (4), 257-263.

12. Herne, T. M.; Tarlov, M. J., Characterization of DNA probes immobilized on gold surfaces. *J. Am. Chem. Soc.* **1997,** *119* (38), 8916-8920.

13. Steel, A. B.; Herne, T. M.; Tarlov, M. J., Electrochemical quantitation of DNA immobilized on gold. *Anal. Chem.* **1998,** *70* (22), 4670-4677.

14. Erkkila, K. E.; Odom, D. T.; Barton, J. K., Recognition and reaction of metallointercalators with DNA. *Chem. Rev.* **1999,** *99* (9), 2777-2796.

15. Kelley, S. O.; Barton, J. K.; Jackson, N. M.; Hill, M. G., Electrochemistry of methylene blue bound to a DNA-modified electrode. *Bioconjug. Chem.* **1997,** *8* (1), 31-37.

16. Fan, C.; Plaxco, K. W.; Heeger, A. J., Electrochemical interrogation of conformational changes as a reagentless method for the sequence-specific detection of DNA. *Proc. Natl. Acad. Sci. U.S.A.* **2003,** *100* (16), 9134-9137.

17. Xiao, Y.; Lai, R. Y.; Plaxco, K. W., Preparation of electrode-immobilized, redox-modified oligonucleotides for electrochemical DNA and aptamer-based sensing. *Nat. Protoc.* **2007,** *2* (11), 2875-2880.

18. Boon, E. M.; Ceres, D. M.; Drummond, T. G.; Hill, M. G.; Barton, J. K., Mutation detection by electrocatalysis at DNA-modified electrodes. *Nat. Biotechnol.* **2000,** *18* (10), 1096-1100.

19. Lucarelli, F.; Marrazza, G.; Turner, A. P. F.; Mascini, M., Carbon and gold electrodes as electrochemical transducers for DNA hybridisation sensors. *Biosens. Bioelectron.* **2004,** *19* (6), 515-530.

20. Odenthal, K. J.; Gooding, J. J., An introduction to electrochemical DNA biosensors. *Analyst* **2007,** *132* (7), 603-610.

21. Pei, H.; Lu, N.; Wen, Y.; Song, S.; Liu, Y.; Yan, H.; Fan, C., A DNA nanostructure-based biomolecular probe carrier platform for electrochemical biosensing. *Adv. Mater.* **2010,** *22* (42), 4754-4758.

22. Shen, Z.; Sintim, H. O.; Semancik, S., Rapid nucleic acid melting analyses using a microfabricated electrochemical platform. *Anal. Chim. Acta* **2015,** *853*, 265-270.

23. Mergny, J. L.; Lacroix, L., Analysis of thermal melting curves. *Oligonucleotides* **2003,** *13* (6), 515-537.

24. Wilson, W. D.; Tanious, F. A.; Fernandez-Saiz, M.; Rigl, C. T., Evaluation of drug-nucleic acid interactions by thermal melting curves. *Methods Mol. Biol.* **1997,** *90*, 219-240.

25. Breslauer, K. J.; Remeta, D. P.; Chou, W. Y.; Ferrante, R.; Curry, J.; Zaunczkowski, D.; Snyder, J. G.; Marky, L. A., Enthalpy-entropy compensations in drug-DNA binding studies. *Proc. Natl. Acad. Sci. U.S.A.* **1987,** *84* (24), 8922-8926.

26. Freire, E.; van Osdol, W. W.; Mayorga, O. L.; Sanchez-Ruiz, J. M., Calorimetrically determined dynamics of complex unfolding transitions in proteins. *Annu. Rev. Biophys. Biophys. Chem.* **1990,** *19* (1), 159-188.

27. Owczarzy, R., Melting temperatures of nucleic acids: Discrepancies in analysis. *Biophys. Chem.* **2005,** *117* (3), 207-215.

28. Craig, M. E.; Crothers, D. M.; Doty, P., Relaxation kinetics of dimer formation by self complementary oligonucleotides. *J. Mol. Biol.* **1971,** *62* (2), 383-401.

29. SantaLucia, J., Jr., A unified view of polymer, dumbbell, and oligonucleotide DNA nearest-neighbor thermodynamics. *Proc. Natl. Acad. Sci. U.S.A.* **1998,** *95* (4), 1460-1465.

30. Allawi, H. T.; SantaLucia, J., Jr., Thermodynamics and NMR of internal G.T mismatches in DNA. *Biochemistry* **1997,** *36* (34), 10581-10594.

31. Owczarzy, R.; You, Y.; Moreira, B. G.; Manthey, J. A.; Huang, L. Y.; Behlke, M. A.; Walder, J. A., Effects of sodium ions on DNA duplex oligomers: Improved predictions of melting temperatures. *Biochemistry* **2004,** *43* (12), 3537-3554.

32. Owczarzy, R.; Moreira, B. G.; You, Y.; Behlke, M. A.; Walder, J. A., Predicting stability of DNA duplexes in solutions containing magnesium and monovalent cations. *Biochemistry* **2008,** *47* (19), 5336-5353.

33. SantaLucia, J., Jr.; Hicks, D., The thermodynamics of DNA structural motifs. *Annu. Rev. Biophys. Biomol. Struct.* **2004,** *33*, 415-440.

34. Schreiber-Gosche, S.; Edwards, R. A., Thermodynamics of oligonucleotide duplex melting. *J. Chem. Educ.* **2009,** *86* (5), 644-650.

35. Borer, P. N.; Dengler, B.; Tinoco, I., Jr.; Uhlenbeck, O. C., Stability of ribonucleic acid double-stranded helices. *J. Mol. Biol.* **1974,** *86* (4), 843-853.

36. Vologodskii, A.; Frank-Kamenetskii, M. D., DNA melting and energetics of the double helix. *Phys. of Life Rev.* **2018,** *25*, 1-21.

37. Owczarzy, R., Predicting melting and folding of nucleic acids: Comment on "DNA melting and energetics of double helix" by Alexander Vologodskii and Maxim D. Frank-Kamenetskii. *Phys. Life Rev.* **2018,** *25*, 24-25.

38. D'Abramo, M.; Castellazzi, C. L.; Orozco, M.; Amadei, A., On the nature of DNA hyperchromic effect. *J. Phys. Chem. B* **2013,** *117* (29), 8697-8704.

39. Cardullo, R. A.; Agrawal, S.; Flores, C.; Zamecnik, P. C.; Wolf, D. E., Detection of nucleic acid hybridization by nonradiative fluorescence resonance energy transfer. *Proc. Natl. Acad. Sci. U.S.A.* **1988,** *85* (23), 8790-8794.

40. De Cian, A.; Guittat, L.; Kaiser, M.; Sacca, B.; Amrane, S.; Bourdoncle, A.; Alberti, P.; Teulade-Fichou, M. P.; Lacroix, L.; Mergny, J. L., Fluorescence-based melting assays for studying quadruplex ligands. *Methods* **2007,** *42* (2), 183-195.

41. Moreira, B. G.; You, Y.; Owczarzy, R., Cy3 and Cy5 dyes attached to oligonucleotide terminus stabilize DNA duplexes: Predictive thermodynamic model. *Biophys. Chem.* **2015,** *198*, 36-44.

42. Moreira, B. G.; You, Y.; Behlke, M. A.; Owczarzy, R., Effects of fluorescent dyes, quenchers, and dangling ends on DNA duplex stability. *Biochem. Biophys. Res. Commun.* **2005,** *327* (2), 473-484.

43. Pantoliano, M. W.; Petrella, E. C.; Kwasnoski, J. D.; Lobanov, V. S.; Myslik, J.; Graf, E.; Carver, T.; Asel, E.; Springer, B. A.; Lane, P.; Salemme, F. R., High-density miniaturized thermal shift assays as a general strategy for drug discovery. *Journal of Biomolecular Screening* **2001,** *6* (6), 429-440.

44. Razinkov, V. I.; Treuheit, M. J.; Becker, G. W., Methods of high throughput biophysical characterization in biopharmaceutical development. *Curr. Drug Discov. Technol.* **2013,** *10* (1), 59-70.

45. Samra, H. S.; He, F., Advancements in high throughput biophysical technologies: Applications for characterization and screening during early formulation development of monoclonal antibodies. *Mol. Pharmacol.* **2012,** *9* (4), 696-707.

46. Simeonov, A., Recent developments in the use of differential scanning fluorometry in protein and small molecule discovery and characterization. *Expert Opin. Drug Discov.* **2013,** *8* (9), 1071-1082.

47. Feig, A., *Calorimetry*. 1st ed.; Elsevier Science: 2016; p 530.

48. Garbett, N. C.; Chaires, J. B., Thermodynamic studies for drug design and screening. *Expert Opin. Drug Discov.* **2012,** *7* (4), 299-314.

49. McCluskey, P. J.; Vlassak, J. J., Combinatorial nanocalorimetry. *J. Mater. Res.* **2011,** *25* (11), 2086-2100.

50. Levicky, R.; Horgan, A., Physicochemical perspectives on DNA microarray and biosensor technologies. *Trends Biotechnol.* **2005,** *23* (3), 143-149.

51. Qiao, W.; Chiang, H. C.; Xie, H.; Levicky, R., Surface vs. solution hybridization: Effects of salt, temperature, and probe type. *Chem. Commun. (Camb)* **2015,** *51* (97), 17245-17248.

52. Malmqvist, M., Biospecific interaction analysis using biosensor technology. *Nature* **1993,** *361* (6408), 186-187.

53. Karlsson, R., SPR for molecular interaction analysis: A review of emerging application areas. *J. Mol. Recognit.* **2004,** *17* (3), 151-161.

54. Peterlinz, K. A.; Georgiadis, R. M.; Herne, T. M.; Tarlov, M. J., Observation of hybridization and dehybridization of thiol-tethered DNA using two-color surface plasmon resonance spectroscopy. *J. Am. Chem. Soc.* **1997,** *119* (14), 3401-3402.

55. Peterson, A. W.; Heaton, R. J.; Georgiadis, R. M., The effect of surface probe density on DNA hybridization. *Nucleic Acids Res.* **2001,** *29* (24), 5163-5168.

56. Heaton, R. J.; Peterson, A. W.; Georgiadis, R. M., Electrostatic surface plasmon resonance: Direct electric field-induced hybridization and denaturation in monolayer nucleic acid films and label-free discrimination of base mismatches. *Proc. Natl. Acad. Sci. U.S.A.* **2001,** *98* (7), 3701-3704.

57. Buhot, A.; Halperin, A., Extension of rod-coil multiblock copolymers and the effect of the helix-coil transition. *Phys. Rev. Lett.* **2000,** *84* (10), 2160-2163.

58. Buhot, A.; Halperin, A., On the helix-coil transition in grafted chains. *Europhys. Lett.* **2000,** *50* (6), 756-761.

59. Buhot, A.; Halperin, A., Extension behavior of helicogenic polypeptides. *Macromolecules* **2002,** *35* (8), 3238-3252.

60. Buhot, A.; Halperin, A., Effects of stacking on the configurations and elasticity of single-stranded nucleic acids. *Phys. Rev. E.* **2004,** *70* (2 Pt 1), 020902.

61. Halperin, A.; Buhot, A.; Zhulina, E. B., Sensitivity, specificity, and the hybridization isotherms of DNA chips. *Biophys. J.* **2004,** *86* (2), 718-730.

62. Halperin, A.; Buhot, A.; Zhulina, E. B., Hybridization isotherms of DNA microarrays and the quantification of mutation studies. *Clin. Chem.* **2004,** *50* (12), 2254-2262.

63. Halperin, A.; Buhot, A.; Zhulina, E. B., Hybridization at a surface: The role of spacers in DNA microarrays. *Langmuir* **2006,** *22* (26), 11290-11304.

64. Halperin, A.; Buhot, A.; Zhulina, E. B., On the hybridization isotherms of DNA microarrays: The Langmuir model and its extensions. *J. Phys.: Condens. Mat.* **2006,** *18* (18), S463-S490.

65. Fiche, J. B.; Buhot, A.; Calemczuk, R.; Livache, T., Temperature effects on DNA chip experiments from surface plasmon resonance imaging: Isotherms and melting curves. *Biophys. J.* **2007,** *92* (3), 935-946.

66. Fiche, J. B.; Fuchs, J.; Buhot, A.; Calemczuk, R.; Livache, T., Point mutation detection by surface plasmon resonance imaging coupled with a temperature scan method in a model system. *Anal. Chem.* **2008,** *80* (4), 1049-1057.

67. Melaine, F.; Roupioz, Y.; Buhot, A., Gold nanoparticles surface plasmon resonance enhanced signal for the detection of small molecules on split-aptamer microarrays (small molecules detection from split-aptamers). *Microarrays* **2015,** *4* (1), 41-52.

68. Melaine, F.; Coilhac, C.; Roupioz, Y.; Buhot, A., A nanoparticle-based thermodynamic aptasensor for small molecule detection. *Nanoscale* **2016,** *8* (38), 16947-16954.

69. Campion, A.; Kambhampati, P., Surface-enhanced Raman scattering. *Chem. Soc. Rev.* **1998,** *27* (4), 241-250.

70. Fan, M.; Andrade, G. F. S.; Brolo, A. G., A review on the fabrication of substrates for surface enhanced Raman spectroscopy and their applications in analytical chemistry. *Anal. Chim. Acta* **2011,** *693* (1-2), 7-25.

71. Vo-Dinh, T.; Houck, K.; Stokes, D. L., Surface-enhanced Raman gene probes. *Anal. Chem.* **1994,** *66* (20), 3379-3383.

72. Mahajan, S.; Richardson, J.; Brown, T.; Bartlett, P. N., SERS-melting: A new method for discriminating mutations in DNA sequences. *J. Am. Chem. Soc.* **2008,** *130* (46), 15589-15601.

73. Johnson, R. P.; Gale, N.; Richardson, J. A.; Brown, T.; Bartlett, P. N., Denaturation of dsDNA immobilised at a negatively charged gold electrode is not caused by electrostatic repulsion. *Chem. Sci.* **2013,** *4*, 1625–1632.

74. Papadopoulou, E.; Gale, N.; Thompson, J. F.; Fleming, T. A.; Brown, T.; Bartlett, P. N., Specifically horizontally tethered DNA probes on Au surfaces allow labelled and label-free DNA detection using SERS and electrochemically driven melting. *Chem. Sci.* **2016,** *7* (1), 386-393.

75. Nicolini, C.; Erokhin, V.; Facci, P.; Guerzoni, S.; Ross, A.; Paschkevitsch, P., Quartz balance DNA sensor. *Biosens. Bioelectron.* **1997,** *12* (7), 613-618.

76. Dultsev, F. N.; Kolosovsky, E. A.; Lomzov, A. A.; Pyshnyi, D. V., QCM-based rupture force measurement as a tool to study DNA dehybridization and duplex stability. *Anal. Bioanal. Chem.* **2017,** *409* (4), 891-901.

77. Kurus, N. N.; Dultsev, F. N., Determination of the thermodynamic parameters of DNA double helix unwinding with the help of mechanical methods. *ACS Omega* **2018,** *3*, 2793-2797.

78. Dultsev, F. N.; Kurus, N. N., Temperature dependence of unwinding forces between complementary oligonucleotides. *J. Microbiol. Methods* **2017,** *143*, 94-97.

79. Howell, W. M.; Jobs, M.; Gyllensten, U.; Brookes, A. J., Dynamic allele-specific hybridization. A new method for scoring single nucleotide polymorphisms. *Nat. Biotechnol.* **1999,** *17* (1), 87-88.

80. Jobs, M.; Fredriksson, S.; Brookes, A. J.; Landegren, U., Effect of oligonucleotide truncation on single-nucleotide distinction by solid-phase hybridization. *Anal. Chem.* **2002,** *74* (1), 199-202.

81. Lagally, E. T.; Emrich, C. A.; Mathies, R. A., Fully integrated PCR-capillary electrophoresis microsystem for DNA analysis. *Lab on a Chip* **2001,** *1* (2), 102-107.

82. Dodge, A.; Turcatti, G.; Lawrence, I.; de Rooij, N. F.; Verpoorte, E., A microfluidic platform using molecular beacon-based temperature calibration for thermal dehybridization of surface-bound DNA. *Anal. Chem.* **2004,** *76* (6), 1778-1787.

83. Eid, J.; Fehr, A.; Gray, J.; Luong, K.; Lyle, J.; Otto, G.; Peluso, P.; Rank, D.; Baybayan, P.; Bettman, B.; Bibillo, A.; Bjornson, K.; Chaudhuri, B.; Christians, F.; Cicero, R.; Clark, S.; Dalal, R.; Dewinter, A.; Dixon, J.; Foquet, M.; Gaertner, A.; Hardenbol, P.; Heiner, C.; Hester, K.; Holden, D.; Kearns, G.; Kong, X.; Kuse, R.; Lacroix, Y.; Lin, S.; Lundquist, P.; Ma, C.; Marks, P.; Maxham, M.; Murphy, D.; Park, I.; Pham, T.; Phillips, M.; Roy, J.; Sebra, R.; Shen, G.; Sorenson, J.; Tomaney, A.; Travers, K.; Trulson, M.; Vieceli, J.; Wegener, J.; Wu, D.; Yang, A.; Zaccarin, D.; Zhao, P.; Zhong, F.; Korlach, J.; Turner, S., Real-time DNA sequencing from single polymerase molecules. *Science* **2009,** *323* (5910), 133-138.

84. Sobek, J.; Rehrauer, H.; Schauer, S.; Fischer, D.; Patrignani, A.; Landgraf, S.; Korlach, J.; Schlapbach, R., Single-molecule DNA hybridisation studied by using a modified DNA sequencer: A comparison with surface plasmon resonance data. *Methods Appl Fluores* **2016,** *4* (1), 015002.

85. Chen, T.; Jia, Y.; Dong, C.; Gao, J.; Mak, P.-I.; Martins, R. P., Sub-7-second genotyping of single-nucleotide polymorphism by high-resolution melting curve analysis on a thermal digital microfluidic device. *Lab on a Chip* **2016,** *16* (4), 743-752.

86. Knob, R.; Nelson, D. B.; Robison, R. A.; Woolley, A. T., Sequence-specific DNA solid-phase extraction in an on-chip monolith: Towards detection of antibiotic resistance genes. *J. Chromatogr. A* **2017,** *1523*, 309-315.

87. Traeger, J. C.; Schwartz, D. K., Surface-mediated DNA hybridization: Effects of DNA conformation, surface chemistry, and electrostatics. *Langmuir* **2017,** *33* (44), 12651-12659.

88. Wang, J., *Analytical Electrochemistry*. 3rd ed.; John Wiley & Sons, Inc.: 2006.

89. Labib, M.; Sargent, E. H.; Kelley, S. O., Electrochemical Methods for the Analysis of Clinically Relevant Biomolecules. *Chem. Rev.* **2016,** *116* (16), 9001-9090.

90. Ferapontova, E. E., Electrochemical indicators for DNA electroanalysis. *Curr. Anal. Chem.* **2011,** *7* (1), 51-62.

91. Lai, R. Y.; Lagally, E. T.; Lee, S. H.; Soh, H. T.; Plaxco, K. W.; Heeger, A. J., Rapid, sequence-specific detection of unpurified PCR amplicons via a reusable, electrochemical sensor. *Proc. Natl. Acad. Sci. U.S.A.* **2006,** *103* (11), 4017-4021.

92. De Crozals, G.; Farre, C.; Sigaud, M.; Fortgang, P.; Sanglar, C.; Chaix, C., Methylene blue phosphoramidite for DNA labelling. *Chem. Commun.* **2015,** *51* (21), 4458-4461.

93. Pheeney, C. G.; Barton, J. K., DNA electrochemistry with tethered methylene blue. *Langmuir* **2012,** *28* (17), 7063-7070.

94. Anne, A.; Bouchardon, A.; Moiroux, J., 3'-Ferrocene-labeled oligonucleotide chains end-tethered to gold electrode surfaces: Novel model systems for exploring flexibility of short DNA using cyclic voltammetry. *J. Am. Chem. Soc.* **2003,** *125* (5), 1112-1113.

95. Arroyo-Curras, N.; Dauphin-Ducharme, P.; Ortega, G.; Ploense, K. L.; Kippin, T. E.; Plaxco, K. W., Subsecond-resolved molecular measurements in the living body using chronoamperometrically interrogated aptamer-based sensors. *ACS Sens.* **2018,** *3* (2), 360-366.

96. Marquette, C. A.; Lawrence, I.; Polychronakos, C.; Lawrence, M. F., Impedance based DNA chip for direct $T_m$. *Talanta* **2002,** *56*, 763–768.

97. Henry, O. Y. F.; Sanchez, J. L. A.; O'Sullivan, C. K., Bipodal PEGylated alkanethiol for the enhanced electrochemical detection of genetic markers involved in breast cancer. *Biosens. Bioelectron.* **2010,** *26* (4), 1500-1506.

98. Henry, O. Y. F.; Perez, J. G.; Sanchez, J. L. A.; O'Sullivan, C. K., Electrochemcial characterisation and hybridisation efficiency of co-assembled monolayers of PEGylated ssDNA and mercaptohexanol on planar gold electrodes. *Biosens. Bioelectron.* **2010,** *25* (5), 978-983.

99. Belozerova, I.; Levicky, R., Melting thermodynamics of reversible DNA/ligand complexes at interfaces. *J. Am. Chem. Soc.* **2012,** *134* (45), 18667-18676.

100. Belozerova, I.; Ge, D.; Levicky, R., Electrochemical measurements of DNA melting on surfaces. *Methods Mol. Biol.* **2013,** *1025*, 127-136.

101. Eckermann, A. L.; Feld, D. J.; Shaw, J. A.; Meade, T. J., Electrochemistry of redox-active self-assembled monolayers. *Coord. Chem. Rev.* **2010,** *254* (15-16), 1769-1802.

102. Yang, A. H.; Hsieh, K.; Patterson, A. S.; Ferguson, B. S.; Eisenstein, M.; Plaxco, K. W.; Soh, H. T., Accurate zygote-specific discrimination of single-nucleotide polymorphisms using microfluidic electrochemical DNA melting curves. *Angew. Chem. Int. Ed. Engl.* **2014,** *53* (12), 3163-3167.

103. Lai, R. Y.; Walker, B.; Stormberg, K.; Zaitouna, A. J.; Yang, W., Electrochemical techniques for characterization of stem-loop probe and linear probe-based DNA sensors. *Methods* **2013,** *64* (3), 267-275.

104. Ramaley, L.; Krause, M. S., Theory of square wave voltammetry. *Anal. Chem.* **1969,** *41* (11), 1362-1365.

105. Turner, J. A.; Christie, J. H.; Vukovic, M.; Osteryoung, R. A., Square wave voltammetry at the dropping mercury electrode: Experimental. *Anal. Chem.* **1977,** *49* (13), 1904-1908.

106. Christie, J. H.; Turner, J. A.; Osteryoung, R. A., Square wave voltammetry at the dropping mercury electrode: Theory. *Anal. Chem.* **1977,** *49* (13), 1899-1903.

107. Meunier-Prest, R.; Raveau, S.; Finot, E.; Legay, G.; Cherkaoui-Malki, M.; Latruffe, N., Direct measurement of the melting temperature of supported DNA by electrochemical method. *Nucleic Acids Res.* **2003,** *31* (23), e150.

108. Miralles, V.; Huerre, A.; Malloggi, F.; Jullien, M. C., A review of heating and temperature control in microfluidic systems: Techniques and applications. *Diagnostics* **2013,** *3* (1), 33-67.

109. Ferro Tec. A Guide to Thermoelectrics. www.thermal.ferrotec.com/technology (accessed on Oct 20, 2019).

110. Bhattacharyya, P., Technological journey towards reliable microheater development for MEMS gas sensors: A review. *IEEE T Device Mat Re* **2014,** *14* (2), 589-599.

111. Semancik, S.; Cavicchi, R. E.; Wheeler, M. C.; Tiffany, J. E.; Poirier, G. E.; Walton, R. M.; Suehle, J. S.; Panchapakesan, B.; DeVoe, D. L., Microhotplate platforms for chemical sensor research. *Sensor. Actuat. B-Chem.* **2001,** *77* (1-2), 579-591.

112. Barrettino, D.; Graf, M.; Kirstein, K.; Hierlemann, A.; Baltes, H., A monolithic fully-differential CMOS gas sensor microsystem for microhotplate temperatures up to 450°C. In *2004 IEEE International Symposium on Circuits and Systems*, 2004; pp 888-891.

113. Contento, N. M.; Semancik, S., Thermal characteristics of temperature-controlled electrochemical microdevices. *Sensor. Actuat. B-Chem.* **2016,** *225*, 279-287.

114. Grundler, P.; Flechsig, G. U., Deposition and stripping at heated microelectrodes. Arsenic(V) at a gold electrode. *Electrochim. Acta* **1998,** *43* (23), 3451-3458.

115. Wang, J.; Grundler, P.; Flechsig, G. U.; Jasinski, M.; Rivas, G.; Sahlin, E.; Paz, J. L. L., Stripping analysis of nucleic acids at a heated carbon paste electrode. *Anal. Chem.* **2000,** *72* (16), 3752-3756.

116. Biala, K.; Sedova, A.; Flechsig, G. U., Sequence and temperature influence on kinetics of DNA strand displacement at gold electrode surfaces. *ACS Appl. Mater. Interfaces* **2015,** *7* (36), 19948-19959.

117. Flechsig, G. U., New electrode materials and devices for thermoelectrochemical studies and applications. *Curr. Opin. Electrochem.* **2018,** *10*, 54-60.

118. Surkus, A. E.; Flechsig, G. U., Electrochemical detection of DNA melting curves by means of heated biosensors. *Electroanal.* **2009,** *21* (10), 1119-1123.

119. Walter, A.; Langschwager, F.; Marken, F.; Flechsig, G. U., Nanostructured heated gold electrodes for DNA hybridization detection using enzyme labels. *Sensor. Actuat. B-Chem.* **2016,** *233*, 502-509.

120. Walter, A.; Surkus, A. E.; Flechsig, G. U., Hybridization detection of enzyme-labeled DNA at electrically heated electrodes. *Anal. Bioanal. Chem.* **2013,** *405* (11), 3907-3911.

121. Franssila, S., *Introduction to microfabrication*. 2nd ed.; John Wiley & Sons Ltd: Chichester, U.K. ; Hoboken, N.J., 2010; p 518.

122. Robinson, S. M.; Shen, Z.; Askim, J. R.; Montgomery, C. B.; Sintim, H. O.; Semancik, S., Ligand-based stability changes in duplex DNA measured with a microscale electrochemical platform. *Biosensors* **2019,** *9* (2).

123. Shen, Z. A temperature-controlled electrochemical microscale platform for biomolecular binding studies. University of Maryland, College Park, 2014.

124. Rosenbaum, E.; King, J. C.; Hu, C. M., Accelerated testing of $SiO_2$ reliability. *IEEE Trans. Electron Dev.* **1996,** *43* (1), 70-80.

125. Momose, H. S.; Nakamura, S. I.; Katsumata, Y.; Iwai, H., Study of direct-tunneling gate oxides for CMOS applications. In *1998 3rd International Symposium on Plasma Process-Induced Damage (Cat. No.98EX100)*, 1998; pp 30-33.

126. McPherson, J.; Kim, J.; Shanware, A.; Mogul, H.; Rodriguez, J., Proposed universal relationship between dielectric breakdown and dielectric constant. *International Electron Devices 2002 Meeting, Technical Digest* **2002**, 633-636.

127. Koutsaroff, I. P.; Zelner, M.; Woo, P.; McNeil, L.; Buchbinder, M.; Cervin-Lawry, A., Oxidized titanium as a bottom electrode adhesion layer for the multilayer (Ba,Sr)$TiO_3$ capacitors. *Integr. Ferroelectr.* **2010,** *45* (1), 97-103.

128. Litvinov, J.; Wang, Y. J.; George, J.; Chinwangso, P.; Brankovic, S.; Willson, R. C.; Litvinov, D., Development of pinhole-free amorphous aluminum oxide protective layers for biomedical device applications. *Surf. Coat. Technol.* **2013,** *224*, 101-108.

129. Neidle, S., DNA minor-groove recognition by small molecules. *Nat. Prod. Rep.* **2001,** *18* (3), 291-309.

130. Emami, S.; Dadashpour, S., Current developments of coumarin-based anti-cancer agents in medicinal chemistry. *Eur. J. Med. Chem.* **2015,** *102*, 611-630.

131. Balasubramanian, S.; Hurley, L. H.; Neidle, S., Targeting G-quadruplexes in gene promoters: A novel anticancer strategy? *Nat. Rev. Drug Discov.* **2011,** *10* (4), 261-275.

132. Kohn, K. W., Beyond DNA cross-linking: History and prospects of DNA-targeted cancer treatment--fifteenth Bruce F. Cain Memorial Award Lecture. *Cancer Res.* **1996,** *56* (24), 5533-5546.

133. Pommier, Y.; Leo, E.; Zhang, H.; Marchand, C., DNA topoisomerases and their poisoning by anticancer and antibacterial drugs. *Chem. Biol.* **2010,** *17* (5), 421-433.

134. Rescifina, A.; Zagni, C.; Varrica, M. G.; Pistarà, V.; Corsaro, A., Recent advances in small organic molecules as DNA intercalating agents: Synthesis, activity, and modeling. *Eur. J. Med. Chem.* **2014,** *74*, 95-115.

135. Patel, A. G.; Kaufmann, S. H., How does doxorubicin work? *Elife* **2012,** *1*, e00387.

136. Gewirtz, D. A., A critical evaluation of the mechanisms of action proposed for the antitumor effects of the anthracycline antibiotics adriamycin and daunorubicin. *Biochem. Pharmacol.* **1999,** *57* (7), 727-741.

137. Turner, P. R.; Denny, W. A., The mutagenic properties of DNA minor-groove binding ligands. *Mutat. Res.* **1996,** *355* (1-2), 141-169.

138. Bhaduri, S.; Ranjan, N.; Arya, D. P., An overview of recent advances in duplex DNA recognition by small molecules. *Beilstein J. Org. Chem.* **2018,** *14*, 1051-1086.

139. Wegner, M.; Grummt, F., Netropsin, distamycin and berenil interact differentially with a high-affinity binding site for the high mobility group protein HMG-I. *Biochem. Biophys. Res. Commun.* **1990,** *166* (3), 1110-1117.

140. Barcelo, F.; Ortiz-Lombardia, M.; Portugal, J., Heterogeneous DNA binding modes of berenil. *Biochim. Biophys. Acta* **2001,** *1519* (3), 175-184.

141. Tse, W. C.; Boger, D. L., A fluorescent intercalator displacement assay for establishing DNA binding selectivity and affinity. *Acc. Chem. Res.* **2004,** *37* (1), 61-69.

142. Rauf, S.; Gooding, J. J.; Akhtar, K.; Ghauri, M. A.; Rahman, M.; Anwar, M. A.; Khalid, A. M., Electrochemical approach of anticancer drugs--DNA interaction. *J. Pharm. Biomed. Anal.* **2005,** *37* (2), 205-217.

143. Makaraviciute, A.; Xu, X.; Nyholm, L.; Zhang, Z., Systematic approach to the development of microfabricated biosensors: Relationship between gold surface pretreatment and thiolated molecule binding. *ACS Appl. Mater. Interfaces* **2017,** *9* (31), 26610-26621.

144. Fischer, L. M.; Tenje, M.; Heiskanen, A. R.; Masuda, N.; Castillo, J.; Bentien, A.; Emneus, J.; Jakobsen, M. H.; Boisen, A., Gold cleaning methods for electrochemical detection applications. *Microelectron. Eng.* **2009,** *86* (4-6), 1282-1285.

145. Kelly, J. M.; Tossi, A. B.; McConnell, D. J.; OhUigin, C., A study of the interactions of some polypyridylruthenium (II) complexes with DNA using fluorescence spectroscopy, topoisomerisation and thermal denaturation. *Nucleic Acids Res.* **1985,** *13* (17), 6017-6034.

146. Nasef, H.; Ozalp, V. C.; Beni, V.; O'Sullivan, C. K., Melting temperature of surface-tethered DNA. *Anal. Biochem.* **2010,** *406* (1), 34-40.

147. Somasundaram, S.; Holtan, M. D.; Easley, C. J., Understanding signal and background in a thermally resolved, single-branched DNA assay using square wave voltammetry. *Anal. Chem.* **2018,** *90* (5), 3584-3591.

148. He, Y. K.; Zhang, J.; Ruffin, S.; Ji, L. N.; Wang, K.; Levicky, R.; Xia, X. H., An electrochemical study of the surface hybridization process of morpholino-DNA: Thermodynamics and kinetics. *Electroanal.* **2016,** *28* (7), 1647-1653.

149. Flechsig, G. U.; Peter, J.; Hartwich, G.; Wang, J.; Grundler, P., DNA hybridization detection at heated electrodes. *Langmuir* **2005,** *21* (17), 7848-7853.

150. Tseng, H. Y.; Adamik, V.; Parsons, J.; Lan, S. S.; Malfesi, S.; Lum, J.; Shannon, L.; Gray, B., Development of an electrochemical biosensor array for quantitative polymerase chain reaction utilizing three-metal printed circuit board technology. *Sensor. Actuat. B-Chem.* **2014,** *204*, 459-466.

151. Nicholson, B. H.; Peacocke, A. R., The inhibition of ribonucleic acid polymerase by acridines. *Biochem. J.* **1966,** *100* (1), 50-58.

152. Li, H. J.; Crothers, D. M., Relaxation studies of the proflavine-DNA complex: The kinetics of an intercalation reaction. *J. Mol. Biol.* **1969,** *39* (3), 461-477.

153. Kuriakose, S.; Muleme, H. M.; Onyilagha, C.; Singh, R.; Jia, P.; Uzonna, J. E., Diminazene aceturate (Berenil) modulates the host cellular and inflammatory responses to Trypanosoma congolense infection. *PLoS One* **2012,** *7* (11), e48696.

154. Zhou, J.; Le, V.; Kalia, D.; Nakayama, S.; Mikek, C.; Lewis, E. A.; Sintim, H. O., Diminazene or berenil, a classic duplex minor groove binder, binds to G-quadruplexes with low nanomolar dissociation constants and the amidine groups are also critical for G-quadruplex binding. *Mol. Biosyst.* **2014,** *10* (10), 2724-2734.

155. Mikek, C. G.; West, S. J.; Gwin, J. C.; Dayal, N.; Sintim, H. O.; Lewis, E. A., Berenil binds tightly to parallel and mixed parallel/antiparallel G-quadruplex motifs with varied thermodynamic signatures. *ACS Omega* **2018,** *3* (9), 11582-11591.

156. Nakayama, S.; Kelsey, I.; Wang, J.; Sintim, H. O., c-di-GMP can form remarkably stable G-quadruplexes at physiological conditions in the presence of some planar intercalators. *Chem. Commun. (Camb)* **2011,** *47* (16), 4766-4768.

157. Mergny, J. L.; Helene, C., G-quadruplex DNA: A target for drug design. *Nat. Med.* **1998,** *4* (12), 1366-7.

158. Sun, D.; Thompson, B.; Cathers, B. E.; Salazar, M.; Kerwin, S. M.; Trent, J. O.; Jenkins, T. C.; Neidle, S.; Hurley, L. H., Inhibition of human telomerase by a G-quadruplex-interactive compound. *J. Med. Chem.* **1997,** *40* (14), 2113-2116.

159. Phan, A. T., Human telomeric G-quadruplex: Structures of DNA and RNA sequences. *FEBS J.* **2010,** *277* (5), 1107-1117.

160. Lane, A. N.; Chaires, J. B.; Gray, R. D.; Trent, J. O., Stability and kinetics of G-quadruplex structures. *Nucleic Acids Res.* **2008,** *36* (17), 5482-5515.

161. Wang, Y.; Patel, D. J., Guanine residues in d(T2AG3) and d(T2G4) form parallel-stranded potassium cation stabilized G-quadruplexes with anti glycosidic torsion angles in solution. *Biochemistry* **1992,** *31* (35), 8112-9.

162. Phan, A. T.; Patel, D. J., Two-repeat human telomeric d(TAGGGTTAGGGT) sequence forms interconverting parallel and antiparallel G-quadruplexes in solution: Distinct topologies, thermodynamic properties, and folding/unfolding kinetics. *J. Am. Chem. Soc.* **2003,** *125* (49), 15021-15027.

163. Parkinson, G. N.; Lee, M. P. H.; Neidle, S., Crystal structure of parallel quadruplexes from human telomeric DNA. *Nature* **2002,** *417* (6891), 876-880.

164. He, Y.; Neumann, R. D.; Panyutin, I. G., Intramolecular quadruplex conformation of human telomeric DNA assessed with 125I-radioprobing. *Nucleic Acids Res.* **2004,** *32* (18), 5359-5367.

165. Simonsson, T.; Sjöback, R., DNA tetraplex formation studied with fluorescence resonance energy transfer. *J. Biol. Chem.* **1999,** *274* (24), 17379-17383.

166. Xu, H.; Di Antonio, M.; McKinney, S.; Mathew, V.; Ho, B.; O'Neil, N. J.; Santos, N. D.; Silvester, J.; Wei, V.; Garcia, J.; Kabeer, F.; Lai, D.; Soriano, P.; Banath, J.; Chiu, D. S.; Yap, D.; Le, D. D.; Ye, F. B.; Zhang, A.; Thu, K.; Soong, J.; Lin, S. C.; Tsai, A. H.; Osako, T.; Algara, T.; Saunders, D. N.; Wong, J.; Xian, J.; Bally, M. B.; Brenton, J. D.; Brown, G. W.; Shah, S. P.; Cescon, D.; Mak, T. W.; Caldas, C.; Stirling, P. C.; Hieter, P.; Balasubramanian, S.; Aparicio, S., CX-5461 is a DNA G-quadruplex stabilizer with selective lethality in BRCA1/2 deficient tumours. *Nat. Commun.* **2017,** *8* (1), 14432.

167. Asamitsu, S.; Obata, S.; Yu, Z.; Bando, T.; Sugiyama, H., Recent progress of targeted G-quadruplex-preferred ligands toward cancer therapy. *Molecules* **2019,** *24*, 429.

168. Largy, E.; Hamon, F.; Teulade-Fichou, M. P., Development of a high-throughput G4-FID assay for screening and evaluation of small molecules binding quadruplex nucleic acid structures. *Anal. Bioanal. Chem.* **2011,** *400* (10), 3419-3427.

169. Fang, W. J.; Jin, D. Z.; Luo, Y.; Li, H.; Zheng, Y.; Zhang, Z.; Gu, H.; Zheng, S. S., A DNA minor groove binder shows high effectiveness as a quencher for FRET probes. *Bioorg. Med. Chem. Lett.* **2014,** *24* (16), 3956-3960.

170. Xiao, Y.; Lubin, A. A.; Heeger, A. J.; Plaxco, K. W., Label-free electronic detection of thrombin in blood serum by using an aptamer-based sensor. *Angew. Chem. Int. Ed.* **2005,** *44* (34), 5456-5459.

171. Xiao, Y.; Uzawa, T.; White, R. J.; DeMartini, D.; Plaxco, K. W., On the signaling of electrochemical aptamer-based sensors: Collision- and folding-based mechanisms. *Electroanal.* **2009,** *21* (11), 1267-1271.

172. Palacký, J.; Vorlíčková, M.; Kejnovská, I.; Mojzeš, P., Polymorphism of human telomeric quadruplex structure controlled by DNA concentration: A Raman study. *Nucleic Acids Res.* **2013,** *41* (2), 1005-1016.

173. Cao, C.; Zhang, J.; Wen, X.; Dodson, S. L.; Dao, N. T.; Wong, L. M.; Wang, S.; Li, S.; Phan, A. T.; Xiong, Q., Metamaterials-based label-free nanosensor for conformation and affinity biosensing. *ACS Nano* **2013,** *7* (9), 7583-7591.

174. Qiu, S.; Zhao, F.; Zenasni, O.; Li, J.; Shih, W. C., Nanoporous gold disks functionalized with stabilized G-quadruplex moieties for sensing small molecules. *ACS Appl. Mater. Interfaces* **2016,** *8* (44), 29968-29976.

175. Miljanić, S.; Ratkaj, M.; Matković, M.; Piantanida, I.; Gratteri, P.; Bazzicalupi, C., Assessment of human telomeric G-quadruplex structures using surface-enhanced Raman spectroscopy. *Analytical and Bioanalytical Chemistry* **2017,** *409* (9), 2285-2295.

176. Li, Y.; Han, X.; Zhou, S.; Yan, Y.; Xiang, X.; Zhao, B.; Guo, X., Structural features of DNA G-quadruplexes revealed by surface-enhanced Raman spectroscopy. *J. Phys. Chem. Lett.* **2018,** *9* (12), 3245-3252.

177. Xiao, Y.; Lubin, A. A.; Baker, B. R.; Plaxco, K. W.; Heeger, A. J., Single-step electronic detection of femtomolar DNA by target-induced strand displacement in an electrode-bound duplex. *Proc. Natl. Acad. Sci. U.S.A.* **2006,** *103* (45), 16677-16680.

178. Zhou, J. M.; Zhu, X. F.; Lu, Y. J.; Deng, R.; Huang, Z. S.; Mei, Y. P.; Wang, Y.; Huang, W. L.; Liu, Z. C.; Gu, L. Q.; Zeng, Y. X., Senescence and telomere shortening induced by novel potent G-quadruplex interactive agents, quindoline derivatives, in human cancer cell lines. *Oncogene* **2006,** *25* (4), 503-511.

179. Wang, C. H.; Carter-Cooper, B.; Du, Y. X.; Zhou, J.; Saeed, M. A.; Liu, J. B.; Guo, M.; Roembke, B.; Mikek, C.; Lewis, E. A.; Lapidus, R. G.; Sintim, H. O., Alkyne-substituted diminazene as G-quadruplex binders with anticancer activities. *Eur. J. Med. Chem.* **2016,** *118*, 266-275.

180. Ricci, F.; Lai, R. Y.; Heeger, A. J.; Plaxco, K. W.; Sumner, J. J., Effect of molecular crowding on the response of an electrochemical DNA sensor. *Langmuir* **2007,** *23* (12), 6827-6834.

181. Petrovykh, D. Y.; Kimura-Suda, H.; Whitman, L. J.; Tarlov, M. J., Quantitative analysis and characterization of DNA immobilized on gold. *J. Am. Chem. Soc.* **2003,** *125* (17), 5219-5226.

182. Uzawa, T.; Cheng, R. R.; White, R. J.; Makarov, D. E.; Plaxco, K. W., A mechanistic study of electron transfer from the distal termini of electrode-bound, single-stranded DNAs. *J. Am. Chem. Soc.* **2010,** *132* (45), 16120-16126.

183. Novev, J. K.; Compton, R. G., Natural convection effects in electrochemical systems. *Curr. Opin. Electrochem.* **2018,** *7*, 118-129.

184. Yang, S.; Huang, Z. X.; Hou, X. H.; Cheng, F. F.; Wu, S. H.; Sun, J. J., A model for understanding the temperature change of an alternate hot and cold micro-band graphite electrode. *Electrochem. Commun.* **2016,** *68*, 71-75.

185. Silva, S. M.; Tavallaie, R.; Goncales, V. R.; Utama, R. H.; Kashi, M. B.; Hibbert, D. B.; Tilley, R. D.; Gooding, J. J., Dual signaling DNA electrochemistry: An approach to understand DNA interfaces. *Langmuir* **2018,** *34* (4), 1249-1255.

186. Gray, R. D.; Li, J.; Chaires, J. B., Energetics and kinetics of a conformational switch in G-quadruplex DNA. *J. Phys. Chem. B* **2009,** *113* (9), 2676-2683.

187. Petraccone, L.; Spink, C.; Trent, J. O.; Garbett, N. C.; Mekmaysy, C. S.; Giancola, C.; Chaires, J. B., Structure and stability of higher-order human telomeric quadruplexes. *J. Am. Chem. Soc.* **2011,** *133* (51), 20951-20961.

188. Bianchi, F.; Comez, L.; Biehl, R.; D'Amico, F.; Gessini, A.; Longo, M.; Masciovecchio, C.; Petrillo, C.; Radulescu, A.; Rossi, B.; Sacchetti, F.; Sebastiani, F.; Violini, N.; Paciaroni, A., Structure of human telomere G-quadruplex in the presence of a model drug along the thermal unfolding pathway. *Nucleic Acids Res.* **2018,** *46* (22), 11927-11938.

189. Wang, K. Y.; McCurdy, S.; Shea, R. G.; Swaminathan, S.; Bolton, P. H., A DNA aptamer which binds to and inhibits thrombin exhibits a new structural motif for DNA. *Biochemistry* **2002,** *32* (8), 1899-1904.

190. Meneghello, M.; Papadopoulou, E.; Ugo, P.; Bartlett, P. N., Using electrochemical SERS to measure the redox potential of drug molecules bound to dsDNA-a study of mitoxantrone. *Electrochim. Acta* **2016,** *187*, 684-692.

191. Tsuji, G.; Sintim, H. O., Cyclic dinucleotide detection with riboswitch-G-quadruplex hybrid. *Mol. Biosyst.* **2016,** *12* (3), 773-777.

192. Li, H.; Arroyo-Curras, N.; Kang, D.; Ricci, F.; Plaxco, K. W., Dual-reporter drift correction to enhance the performance of electrochemical aptamer-based sensors in whole blood. *J. Am. Chem. Soc.* **2016,** *138* (49), 15809-15812.